COUPLED PHENOMENA IN ARRAYS OF MICROPLASMA DEVICES AND MICROCHANNEL PLASMA DEVICES AS ANTENNAS

BY

SEUNG HOON SUNG

DISSERTATION

Submitted in partial fulfillment of the requirements
for the degree of Doctor of Philosophy in Electrical and Computer Engineering
in the Graduate College of the
University of Illinois at Urbana-Champaign, 2010

Urbana, Illinois

Doctoral Committee:

Professor J. Gary Eden, Chair
Professor Andreas C. Cangellaris
Professor Jennifer T. Bernhard
Professor Kanti Jain
Adjunct Associate Professor Sung-Jin Park

ABSTRACT

Arrays of microcavity and microchannel plasmas with characteristic dimensions of 25 μm–800 μm have been generated in glass substrates. To reproducibly fabricate the arrays, glass micromaching using replica molding and micropowder blasting was proposed and demonstrated. The microplasmas were optically and electrically probed in this work. The investigation showed that each plasma is physically separated and yet, under the proper conditions, is optically and/or electrically coupled to its neighbors. In arrays as large as 10 parallel microchannel plasmas, evidence of optical coupling among the channels is observed in the form of strongly enhanced atomic emission which is attributed to electron heating driven by the resonant absorption of scattered radiation. The transition from Townsend-like discharges to abnormal glow-like discharges was observed in arrays of microcavity plasma devices. During the transition, bistable oscillations of visible emission were observed in microcavity plasma devices operating in Ne at pressures of 200–700 Torr. In this situation, the time-varying distribution of charge deposited on a dielectric layer in a dielectric barrier device structure appears to be responsible for the oscillations and coupling. It was also observed, in arrays of microcavity plasma devices with a gap, that free microdischarges interact with bounded microdischarges over a distance of $\lesssim$500 μm.

In addition, this work explored and demonstrated the possibility of using microchannel plasma devices as antennas. The measured transmission of RF signals and theoretical predictions of the plasma conductivity show that metal antennas can be replaced by microchannel plasmas. The simulated results also suggest that MHz domain frequency is required to drive microchannel plasma antennas in a quasi-continuous mode. Operation of microplasma channels as receiving antennas was also observed in a planar microstrip configuration.

If the LORD delights in a man's way, he makes his steps firm.

ACKNOWLEDGMENTS

First of all, I thank God for allowing me to be here at Illinois. I cannot tell my time here without His Grace. He led me sincerely in his guidance even though I did not recognize His way.

My dearest appreciation is for my best friend and wife, Bohye Kim. I have been in her prayers all the time, especially when I had a hard time. Without her complete support, I could not spend many hours on my experiments. I thank her for the prayers, understanding and encouragement. I believe that God designed us for each other.

I also would like to thank my friend, mentor and adviser, Professor J. Gary Eden, for his sincere support in the last several years. He always motivated me to think about underlying physics that people did not think about or recognize before. His philosophy on research, teaching, life and family deeply impressed and shaped me.

Special thanks to Professor Sung-Jin Park who guided and helped to develop my work on microplasmas. The Laboratory for Optical Physics and Engineering (LOPE) at the University of Illinois at Urbana-Champaign is a unique place to enjoy and learn science and engineering. I have known great people, too. I was nourished by excellent, future scientists and engineers. I would like to thank all the colleagues, past and present, in chronological order. Dr. Clark Wagner, Dr. Kevin Chen, Dr. Jennifer Hafez, Brian Ricconi, Dr. Kwangsoo Kim, Dr. Tom Spinka, Dr. Jason Readle, Brittany Zheng, Ellen Kiester, Brenda Li, Andrew Price, Jeff Putney, Jekwon Yoon, Taek-Lim Kim, Sungkun Lee, Tom Galvin, Darby Hewitt and Tom Houlahan. Special thanks to Tom Galvin for his valuable comments and editing of this thesis. I cannot forget their humor and generosity. A special thank you goes to Professor Ho-Jun Lee from the Pusan National University in Korea. Discussions on physics and engineering including plasmas that we had in the LOPE were most valuable. I also wish to thank the undergraduates who have

assisted me during this work, including Young-Mo Kang, In-Chan Hwang, Yilei Li, Chang Lee and Young-Hwa Kim, for their technical assistance. I am also grateful for the friendship of Young K. Jeong in the last 23 years. I wish to extend my thanks to all my friends in the Jesussamo and John family in the Korean Church at Champaign-Urbana. I am fortunate to share my life with all these great people.

Finally, I would like to thank my family - my mother, sister and her family, father-in-law, mother-in-law and sister-in-law - in Korea. Also, to my father in heaven. Their sincere prayers, advice and support have been the essential part of my life.

TABLE OF CONTENTS

CHAPTER 1

INTRODUCTION

In the last several decades, engineering and physics have progressed rapidly toward nanotechnology and nanoscience, as Richard Feynman envisioned in his lecture, "There's Plenty of Room at the Bottom" [1]. The advancement of research from the macro- to the nano-scale has led to the discovery of novel functional materials such as graphene [2] and phenomena such as quantum jumps of single molecules at room temperature [3]. The significant amount of research in microcavity plasmas (or microplasmas) over the last 15 years can be understood in a similar context.

Microcavity plasmas (or microplasmas) are defined as plasmas spatially confined in cavities having characteristic dimensions of 1 μm–1 mm. The development of semiconductor and microelectromechanical systems (MEMS) fabrication techniques has stimulated this field, and as a result, the spatial scale of the plasmas has moved into the domain below 10 μm [4]. As the characteristic dimensions of plasmas have descreased from the macro- to the micro-scale, several unexpected and attractive properties have been observed, including operating pressures beyond one atmosphere and power loadings higher than hundreds of kW/cm^3. Interesting phenomena such as the breakdown of charge neutrality have also been investigated [5]. This is surprising, considering that a plasma has traditionally been defined as an ionized gas which is quasi-neutral.

In addition to the characterization of beneficial aspects of microplasmas, a variety of new applications which were not possible with macroplasmas are being investigated [6, 7]. Plasma channels provide a diffuse medium of controllable conductivity, offering properties with respect to power deposition and transparency at short wavelengths (vacuum ultraviolet and beyond) that are essential for nonlinear optics in intense radiation fields, and plasma processing under nonequilibrium conditions. Typically formed by the guidance of a laser pulse in gas-filled capillary tubing, filamentation in air, or

focusing with conventional optics, plasma channels reported previously have been restricted in geometry and the characteristics of the plasma [8, 9, 10]. Potential applications of low temperature plasma channels in realizing antennas, chemical synthesis [11] and molecular fragmentation also suggest the desirability of developing parallel processing architectures.

The work in this disseration is based on the demonstration of a glass microfabrication technique by replica molding and micropowder blasting. Glass is a very promising platform for arrays of microplasma devices because it is optically transparent, chemically resistant, strong against sputtering in plasmas and scalable up to at least ∼100 inches (along the diagonal). It also has a dielectric strength of ∼9.8–13.8 MV/m. The versatility of glass, however, is limited by its inert nature. By applying a replication process for the production of a high-resolution mask, low-cost glass micromachining is demonstrated in this work. Through this glass fabrication technique, the generation of low temperature, nonequilibrium microplasmas in linear arrays of 25–200 μm wide channels in glass is reported. Axially uniform glows, produced in rare gases or air at pressures of 200–760 Torr, are confined in channels 2.5 cm in length with cross-sectional areas as small as 250 μm^2. The maximum length of 7.5 cm for a 200 μm wide channel has also been demonstrated. Arrays of microplasmas have also been generated in circular or ellipsoidal microcavities with characteristic dimensions of 50–800 μm and stable operation in several gases or gas mixtures has been confirmed. To date, arrays having active surface areas as large as ∼60 cm^2 have been demonstrated. These microcavity and microchannel plasmas have been electrically and optically probed so as to elucidate the operation in this spatial domain.

The optical probing of arrays of glass microplasmas reveals that rare gas plasmas, spatially confined in at least two dimensions, couple optically when sited sufficiently close to one another. Scattered atomic radiation, transmitted by the array substrate, provides coupling between each microplasma and its nearest neighbors [12]. The spatially-resolved profiles of visible emission of microchannel plasmas are broadened and intensified when they are arrayed in glass. Varying the pitch of arrays and these operating frequencies, it is also demonstrated that an optogalvanic effect is responsible for the coupling phenomena. The spatial broadening and intensification of the visible emission of linear arrays of microchannel plasmas are caused by the radiation

from the adjacent channel and the optogalvanic effects. Optimization of this mechanism for coupling between microplasmas has significant implications for microlasers and on-chip plasma processing, and provides the opportunity to optically modulate the local electric field strength in large arrays.

In addition, arrays of microcavity plasmas with a micron-scale gap are electrically modeled. The analysis leads to the first investigation of the transition from a Townsend-like to an abnormal glow-like discharge in microplasmas. In the course of observing these plasmas by optical microscopy, bistable oscillations of the visible intensity are observed. The oscillation is random in time but appears to be closely related to its neighboring microcavity plasmas owing to charge imbalance. It is also intriguing that microdischarges in a gap can be bounded by a microcavity itself or a microcavity plasma. The bounded microdischarges interact with free microdischarges when they are in proximity to one another. The interaction appears to be attributable to space charge near the dielectric layer and/or geometrical effects of microcavities.

Finally, one of the highlights of this work is the observation that arrays of microchannel plasma devices appear to be attractive as on-chip receiving antennas. This study is a proof-of-concept to replace metal patches of microstrip antennas with arrays of microchannel plasmas. Both experiments and theoretical predictions indicate the potential of microchannel plasmas as radiating or receiving elements in the HF and microwave regions. These results are preliminary, but arrays of microchannel plasma devices could open a new door to invisible antennas in the near future.

CHAPTER 2

LOW TEMPERATURE PLASMA FUNDAMENTALS

2.1 Basic Phenomena in Plasmas

A plasma is a collection of free charged and neutral particles moving with random directions and it is electrically neutral. The temporal variation of the charge density and its spatial distribution, in tandem with any external fields, determines the strength and spatial variation of the electric field. This physical situation sets the stage for novel phenomena which are not possible in other states of matter. Having electrons with high mobility, plasma is an electrical as well as a thermal conductor and emits and absorbs optical radiation.

2.1.1 Electron Oscillations

One of the fundamental properties of plasmas is that under equilibrium condition, they are quasi–neutral. This means that the plasmas are electrictrically neutral on a macroscopic scale. Perturbations to charge neutrality in plasmas lead to an imbalance of charge. The charge imbalance will cause a Coulombic force which restores charge neutrality. Consider a small sphere in a plasma and let us regard the excess of negative charge introduced onto the sphere as a perturbation. Electrons on the sphere will experience a repulsive force which forces the electrons to leave the surface. More electrons than those needed to maintain charge neutrality will leave the region of interest because of the repulsive interaction. This charge imbalance draws electrons onto the sphere and charge neutrality is restored.

The behavior of these oscillations in a low temperature, non–magnetized plasma will now be discussed. Such plasmas are typical of the type discussed in this thesis. The thermal motion of particles and pressure gradients can be

neglected in this model of plasmas. The perturbation of the electron density within a sphere can be given by

$$n_e(\mathbf{r},t) = n_0 + n_e^{'}(\mathbf{r},t) \tag{2.1}$$

where n_e is the electron density, $\mathbf{r}$ is the position vector, t is time and n_0 is the average electron density. The perturbation to the electron density is represented by $n_e^{'}$.

It is assumed that the electric field $\mathbf{E}(\mathbf{r},t)$ and the average velocity of the electrons of $\mathbf{u}_e(\mathbf{r},t)$ are first–order perturbations under the given charge perturbations. The continuity and momentum equations are

$$\frac{\partial n_e^{'}(\mathbf{r},t)}{\partial t} + n_0 \nabla \cdot \mathbf{u}_e(\mathbf{r},t) = 0 \tag{2.2}$$

$$\frac{\partial \mathbf{u}_e(\mathbf{r},t)}{\partial t} = -\frac{e}{m_e}\mathbf{E}(\mathbf{r},t) \tag{2.3}$$

where collisional momentum loss is presumed to be negligible in Equation 2.3.

If the plasma was electrically neutral before it was perturbed, then the charge density (ρ) after the perturbation is related to the number of excess electrons by the expression

$$\rho(\mathbf{r},t) = -en_e^{'}(\mathbf{r},t)\ . \tag{2.4}$$

By integrating Equations 2.1–2.4 so as to yield Gauss's law, the differential equation describing the harmonic motion of electrons in a plasma is obtained:

$$\frac{\partial^2 n_e^{'}(\mathbf{r},t)}{\partial^2 t} + (2\pi f_p)^2 \cdot n_e^{'}(\mathbf{r},t) = 0 \tag{2.5}$$

where the plasma frequency ω_p is given by

$$\omega_p = 2\pi f_p = \sqrt{\frac{n_0 e^2}{m_e \epsilon_0}} \approx 9000\sqrt{n_e} \tag{2.6}$$

where m_e is the mass of an electron, ϵ_0 is the permittivity of free space, n_0 is the average density of electrons, e is charge on an electron and f_p is expressed in Hz.

Equation 2.5 describes the time harmonic oscillation of the perturbation.

The perturbation function can be separated into terms dependent solely on space or time:

$$n_e^{'}(\mathbf{r}, e) = n_e^{'}(\mathbf{r}) exp(-j2\pi f_p t) \ . \tag{2.7}$$

By employing the assumption that all first order quantities are time harmonic, the expression above can be simplified as

$$n_e^{'}(\mathbf{r}) = - \, n_0 \nabla \cdot \mathbf{u}_e \ , \tag{2.8}$$

$$\text{where} \quad u_e(\mathbf{r}) = -\frac{je}{\omega m_e} \mathbf{E}(\mathbf{r}) \ . \tag{2.9}$$

The phase of these quantities does not change in time and this means that the oscillation is stationary. The velocity of the electron(s) represented by Equation 2.3 has the same direction as that of the electric field so that this oscillation is longitudinal. Lastly, this plasma is electrostatic [13].

2.1.2 Wave Propagation in Plasmas

The conductivity and wavevector of plasmas are briefly reviewed here in order to better understand the interaction mechanisms between plasmas and electromagnetic waves.

Microplasmas are generally weakly ionized plasmas with a low temperature in which electron-neutral collisions dominate. The Lorentz gas model can be used to derive the mathematical expression of conductivity and wavevector of plasmas [14]. Specifically, the application of Newton's law to describe the forces exerted on electrons and the collisional loss of the momentum of electrons yields the Langevin equation. For non-magnetized plasmas ($\mathbf{B} = 0$), the Langevin equation is written as follows:

$$\frac{d(m_e \mathbf{u}_e)}{dt} = -e\mathbf{E} - m_e \mathbf{u}_e \nu_m \tag{2.10}$$

where ν_m and $\mathbf{u}_e$ are the collisional frequency for momentum transfer and the average velocity of the electrons, respectively. The constant m_e denotes the mass of an electron, and ν_m is the collision frequency for the transfer of momentum in e^--neutral collisions.

It is assumed that the electric field is oscillating at a frequency of f_0 and can be written as $\mathbf{E}(\mathbf{r}, t) = \mathbf{E}_0(\mathbf{r}) \cdot e^{j2\pi f_0 t}$. Thus, the average velocity of electrons

is given by

$$\mathbf{u}_e = -\frac{e\mathbf{E}}{m_e(\nu_m + jf_0)} \ . \tag{2.11}$$

Thus, from this velocity, the complex conductivity and relative dielectric constant of plasmas are obtained as follows:

$$\sigma_p = \frac{n_e e^2}{m(\nu_m + jf_0)} \ , \tag{2.12}$$

$$\epsilon_p = 1 - \frac{f_p^2/f_0^2}{1 - j\nu_m/f_0} \tag{2.13}$$

where σ_p is the plasma conductivity, ϵ_p is the relative dielectric constant of the plasma, f_p represents the plasma frequency and f_0 is the frequency of an oscillating electric field. The conductivity of plasmas also simplifies to $n_e e^2/m_e\nu_m$ when $\nu_m \gg f_0$.

Plasmas are assumed to be homogeneous and the wave vector k_p in plasmas is derived from the complex dielectric constant. The derivation is as follows:

$$\begin{aligned} k_p &= 2\pi f_0\sqrt{\mu_0\epsilon_p} \\ &= k_r - j \cdot k_i \\ &= k_0(r^{1/4}cos(\phi/2) + j \cdot r^{1/4}sin(\phi/2)) \end{aligned} \tag{2.14}$$

where k_r is the real part of k_p, k_i is the negative of the imaginary part of k_p, and k_0, r and ϕ are defined as:

$$k_0 = 2\pi f_0\sqrt{\mu_0\epsilon_0} \ , \tag{2.15}$$

$$r = \frac{\nu_m^2 \cdot f_0^2 + (f_0^2 - f_p^2)^2}{f_0^2(\nu_m^2 + f_p^2)} \ , \tag{2.16}$$

$$\phi/2 = tan^{-1}\left[-\frac{\nu_m \cdot f_p^2}{f_0(f_0^2 + \nu_m^2 - f_p^2)}\right], \quad Re(\epsilon_p > 0) \ . \tag{2.17}$$

Note that k_i must be positive to be physically acceptable because a positive value for k_i predicts the absorption of electromagnetic waves by plasmas rather than gain. A more detailed derivation of Equations 2.14–2.17 is provided in Appendix A.

The dependence of the absorption coefficient of electromagnetic waves on the frequency of the waves in plasmas is illustrated in Figure 2.1 for two

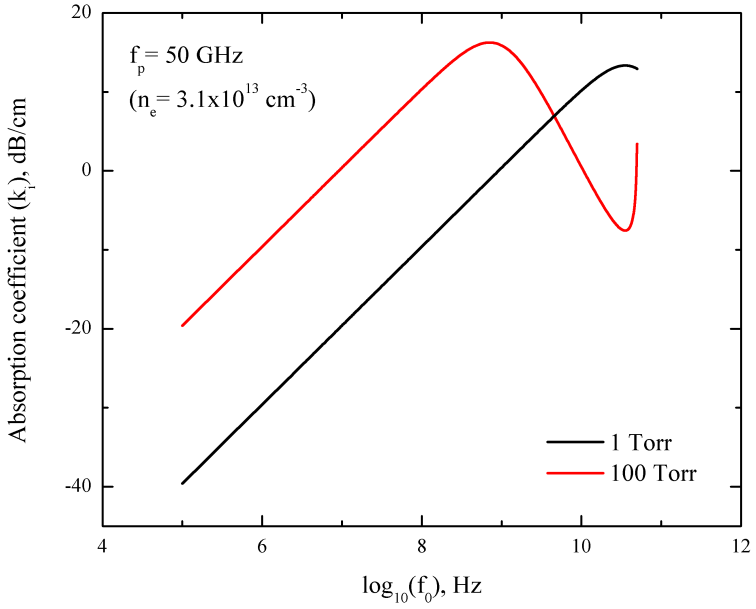

Figure 2.1: Dependence of plasma absorption coefficient on an oscillating frequency of electromagnetic waves (f_0) for different pressures of Ne 1 Torr and 100 Torr.

different pressures in Ne: 1 Torr and 100 Torr. Collisional frequencies for momentum transfer in plasmas were estimated by assuming $\nu_m \approx p(Torr) \cdot 10^9$ $\sec^{-1}$ [15]. Thus, pressures of 1 Torr and 100 Torr of neon correspond to collision frequencies of 1 GHz and 100 GHz, repspectively. A plasma frequency of 50 GHz (when corresponds to $n_e \simeq 3.1\times10^{13}$ cm^{-3}) was assumed for these calculations and incident wave frequencies up to the plasma frequency were considered. The attenuation of an electromagnetic wave mainly relies on k_i. The plots have one local maximum near the collision frequency for each pressure and the absorption coefficient increases up to the local maximum. Note that the collisional loss increases with increasing frequency, in general. When the incoming electromagnetic wave frequency is higher than the collision frequency, the effective collision rate and the collision losses decrease, resulting in a decrease of the absorption coefficient. In 1 Torr of Ne, a local minimum is present near the plasma frequency of 50 GHz and the absorption abruptly increases. This is because of the enhanced energy transfer from electromagnetic waves to electrons oscillating near the plasma frequency.

2.1.3 Plasma Sheath

The plasma sheath is a non–neutral region located between a bulk plasma and a surface. It should be emphasized that, in this region, electrical neutrality is not valid. The structure of the sheath and the potential distribution near the sheath are illustrated in Figure 2.2 [16].

Upon applying a potential (Φ_S) to the electrodes of a discharge device, positive ions accumulate near the cathode and electrons are repelled. Owing to the positive space charge near the cathode, a sheath region is formed in which the electron density is much lower than the ion density. The sheath will be generated even when the electrode is grounded. Because the thermal velocity of electrons is at least 100 times that of ions, the fast electrons may adsorb on the surface or leave the region near the surface before the positive ions can react. Most of the positive ions, however, remain and the region near the zero potential surface can be occupied by positive space charges.

This sheath region is critical to sustaining and understanding glow discharges. One characteristic of the sheath is the presence of a large electric field that is caused by positive space charges. This field accelerates ions to-

ward the cathode and electrons toward the bulk plasma. The accelerated heavy ions approach the surface, thereby generating a deep potential well on the scale of a Bohr radius. The positive ions can recombine with electrons in the conduction band of the surface, which can lead to secondary electron emission. Secondary electrons are accelerated toward the plasma by the electric field of the sheath. These energetic electrons transfer energy to the bulk plasma and play a critical role in maintaining the electron production range necessary for sustenance of the plasma. To derive a mathematical description

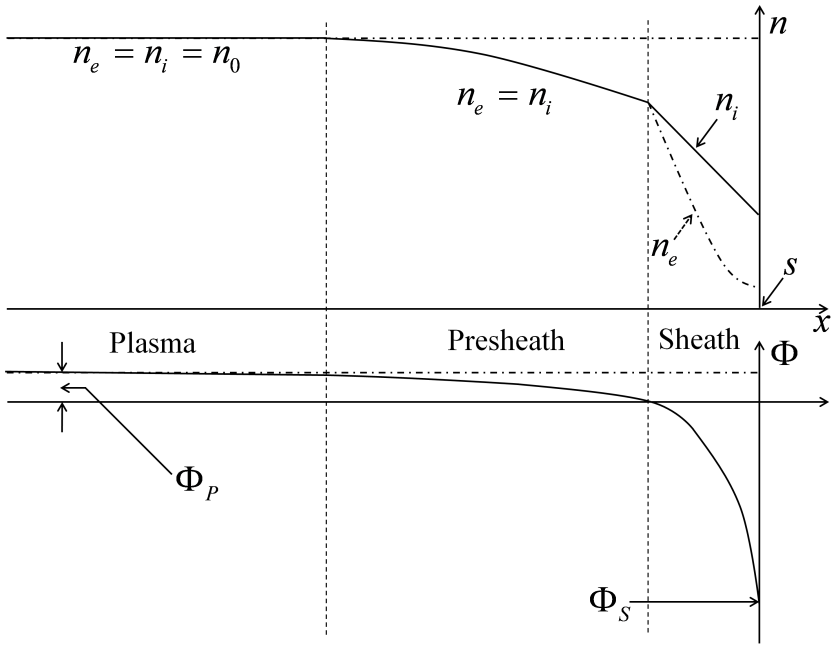

Figure 2.2: Qualitative description of the sheath, presheath and the bulk plasma, where n_e is the density of electrons, n_i is the density of ions, Φ_p is the potential as a plasma, Φ_s is the potential at the surface, $\Phi(x)$ is the potential at the function of position (x) and λ_{sheath} is the sheath width [16].

of the sheath, a collisionless DC sheath is considered here. The integration of Poisson's equation, the equation describing energy conservation for the ion, and the Boltzmann distribution for electrons, describes the potential (Φ) near the sheath as follows:

$$\frac{d^2\Phi}{dx^2} = \frac{en_s}{\epsilon_0}\left[exp\frac{\Phi}{T_e} - \left(1 - \frac{e\Phi}{E_{is}}\right)^{-1/2}\right] \tag{2.18}$$

where n_s is a plasma density at the sheath, T_e is the electron temperature, ϵ is the permittivity of free space, and E_{is} $(1/2Mu_{is}^2)$ is the initial energy of an

ion entering the sheath. The quantities of M and u_{is} are the corresponding mass and velocity for the ions.

A Taylor expansion of Equation 2.18 yields the simplified expression

$$\frac{d^2\Phi}{dx^2} = \frac{2en_s}{\epsilon_0}\left[T_e \cdot exp\left(\frac{e\Phi}{T_e}\right) - T_e + 2E_{is}\left(1 - \frac{e\Phi}{E_{is}}\right)^{1/2} - 2E_{is}\right] . \quad (2.19)$$

Equation 2.19 is only physically meaningful when the initial velocity of an ion is above a threshold value. This minimum velocity, known as Bohm velocity, is given by

$$u_B = \sqrt{\frac{T_e}{M}} . \quad (2.20)$$

In addition to the sheath region near the wall, a presheath region exists between a sheath and the bulk plasma that provides energy to ions so that they may enter the sheath region. The presheath region is a quasi-neutral with a low electric field. Thus, this region provides a slight enhancement of the ion energy so that the velocity of ions can exceed the Bohm velocity.

2.2 Glow Discharges

A glow discharge is generally regarded as a self-sustaining discharge with a cold cathode emitting electrons mainly by secondary electron emission. The general voltage-current (V-I) characteristic of a self-sustained DC discharge between electrodes is illustrated in Figure 2.3.

The region "A" represents a non self-sustained plasma. The plateau denoted Townsend (BC) is a plasma self-sustained by a voltage level higher than the breakdown voltage of V_t. The Townsend discharge generally has a current level of $\sim 10^{-10}$ to 10^{-5} A. At this low current, the electron and ion densities are negligible and the space charge does not distort the electric field between electrodes. In this region, an increase of the voltage leads to the growth of the density of electrons and ions. Eventually, there will be a significant distortion of the electric field due to space charge near the cathode. This corresponds to the transition from a Townsend to a glow discharge. The subnormal glow discharge is identified with this region. The negative slope of the V-I curve is a distinct feature of the subnormal glow discharge. Then, further increases of the external voltage lead to the segment, denoted

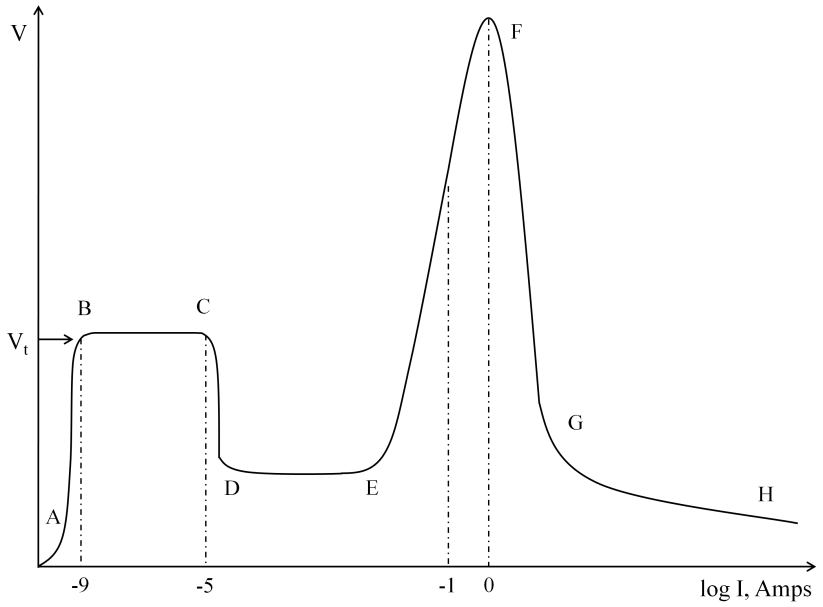

Figure 2.3: V-I characteristics of a DC discharge between electrodes: (A) a region of non-self-sustaining discharge; (BC) Townsend discharge; (CD) subnormal discharge; (DE) normal glow discharge; (EF) abnormal glow discharge; (FG) transition to arc discharge; and (GH) arc. V_t is the threshold voltage for a breakdown. This figure is reproduced from [15].

(DE), that is essentially flat. This is the normal glow discharge. The distinct feature of the normal glow is a constant current density on the cathode, and increases in the current correspond to a growth in the area of the cathode spot. When the cathode surface cannot grow any more, the current continues to increase with increasing voltage in a region known as the abnormal glow region (EF). Continuing increases in the current with increasing voltage in an abnormal glow discharge result in the transition from an abnormal glow to arc discharge (FG) usually at a current value of 1 A. The arc discharge (GH) is distinct from other discharge modes such as Townsend or glow regimes in that the arc sustenance mechanisms are intensive thermoionic and field emission from the cathode.

Of interest in this study is the transition from the Townsend to the glow discharge which was observed in an array of glass microplasma devices. The transition is caused by the growth of the electron and ion density in plasams and the distortion of the electric field, especially near the cathode. The processes responsible for the transition from the Townsend to the glow discharge are mathematically described here. One-dimensional geometry is assumed in order to reduce the mathmatical complexity. In Townsend discharges, a uniform electric field exists and the steady-state continuity equation is valid for charged particles. Thus, the continuity equation in Townsend discharges is as follows [17]:

$$\frac{dj_e}{dx} = \alpha j_e, \quad \frac{dj_i}{dx} = -\alpha j_i \tag{2.21}$$

where j_e is the electron current density, j_i is the ion current density and α is the Townsend coefficient which describes the ionization rate per unit length of discharge.

By applying the appropriate boundary conditions at the cathode and anode, Equation 2.21 can be reduced to the following expression:

$$\alpha \cdot E \cdot L = ln\frac{\gamma + 1}{\gamma} \tag{2.22}$$

where α is the Townsend coefficient, γ is the secondary electron emission, E is the spatially-invariant field strength in Townsend discharge and L is the gap between the electrodes.

Equation 2.22 describes the condition for a self-sustaining Townsend discharge. In a *glow* discharge, the electric field is not uniform and the sustaining

condition of the Townsend discharge (Equation 2.22) cannot be applied to glow discharges. The electric field can, however, be obtained from Gauss's law:

$$\frac{dE}{dx} = \frac{1}{\epsilon_0} e(n_i - n_e) \tag{2.23}$$

where E is the electric field, ϵ_0 is the permittivity of free space, e is the elementary charge, n_i is the ion density and n_e is the electron density.

Assuming that $n_i \approx j/e\mu_i$E and $n_i \gg$ n$_e$ in the sheath, the electric field in the gap (L) is obtained from Equation 2.23 as follows:

$$E = E_c \sqrt{1 - \frac{x}{d}} \tag{2.24}$$

where the E_c is the electric field at the cathode and x is the position in the gap between the electrodes. The position x=0 indicates the cathode and the position x=L indicates the anode in this case. The quantity d is a function of E_c and given by

$$d = \frac{\epsilon_0 \mu_i E_c^2}{2j} \tag{2.25}$$

where ϵ_0 is the permittivity of free space, μ_i is the ion mobility and j is current density.

The evolution of the electric field with current density is illustrated in Figure 2.4 [17]. Equation 2.25 describes the distortion of the electric field that is produced by the current density. The electric field at the cathode (E_c) increases with increasing current density, resulting in increasing distortion of the electric field in the plasma. When d is equal to L, the electric field at the anode is zero. Therefore, we let the current density be j_L and be given by

$$j_L = \frac{\epsilon_0 \mu_i E_c^2}{2L} \tag{2.26}$$

where E_t is the electric field when a breakdown occurs in the gap between electrodes. The electric field is not distorted in the gap and the current is close to zero. When the current is small, the distortion of the electric field is not significant and E_c is approximately equal to E_t. As the current is increased further, E_C deviates from E_t and the electric field and the structure of a discharge are significantly perturbed when the current is larger than j_L. In this situation, the self-sustaining condition is quite different from

Equation 2.22 and the condition is modified as follows:

$$\int_0^L \alpha E(x)dx = ln(1 + 1/\gamma) \ . \tag{2.27}$$

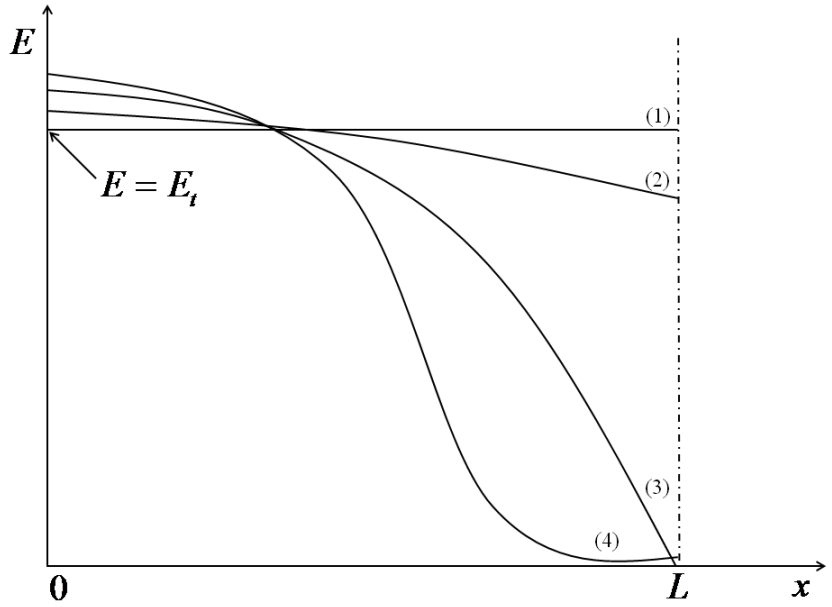

Figure 2.4: Electric field evolution according to different current densities: (1) unperturbed field when j=0; (2) represents a weak current of $j < j_L$; (3) $j = j_L$; and (4) is the transition from Townsend to glow discharges when $j > j_L$, where j_L is the current density when $d = L$, and is equal to $\epsilon_0 \mu_i E_c^2/2L$. E_t is the non-distorted breakdown field in a given gap distance of L. This figure is reproduced from [17].

2.3 Optogalvanic Effect in Neon Plasmas

The optogalvanic effect (OGE) is the term given to changes of the electrical properties of plasmas caused by external light which has a resonance with atomic or molecular transitions of the gas or vapor medium in the plasma. The principle is that the absorption of light causes a redistribution of the populations of the atomic of molecular levels involved in the optical transition. The redistribution of excited or ionized states alters E/N which then changes the density of charged particles, mobility and energy. Changes in

Table 2.1: Selected Neon Transitions which Are Known to Yield a Positive Optogalvanic Signal

Transition	E_{UPPER} (cm^{-1})	E_{LOWER} (cm^{-1})	λ (nm)
$3p[1/2]_1 \rightarrow 3s[3/2]^o_2$	148260	134044	703.24
$3p[5/2]_3 \rightarrow 3s[3/2]^o_2$	149659	134044	640.23
$3p[3/2]_2 \rightarrow 3s[3/2]^o_2$	150318	134044	614.31
$3p'[1/2]_1 \rightarrow 3s[3/2]^o_2$	151040	134044	588.19

the conductivity of the discharge are observed by monitoring the change of a voltage or discharge current. The OGE is positive when the illuminated light increases a discharge current. Otherwise, the OGE is negative [18].

A diagram showing the mechanism of the optogalvanic effect in neon is given in Figure 2.5 [19]. In a neon discharge, the primary route for ionization is the two-step process that concludes with ionization of the two metastable states of $3s[3/2]^o_2$ and $3s'[1/2]^o_0$. Radiative relaxations or collisional de–excitation to $2p^53p$ decreases the ionization rate. When the neon discharge is illuminated by a light source such as a HeNe laser, the population of specific state(s) can be dramatically changed. If the states populated optically lie close to the ionization continuum, an increase of the current (so-called positive activity) is observed in the Ne discharge. Several of the transitions that yield positive optogalvanic effect are summarized in Table 2.1. All the listed transitions have the same lower level of $3s[3/2]^o_1$, one of the metastable states of Ne. Negative OGE activity occurs when the absorbed radiation enhances the population of the $2p^53p$ states which result in a decrease in the ionization rate. The negative activity of an OGE occurs when the radiation enhances the population of $2p^53p$ states because it is an indirect pathway of metastable atoms to radiative decay. Thus, the ionization rate is decreased.

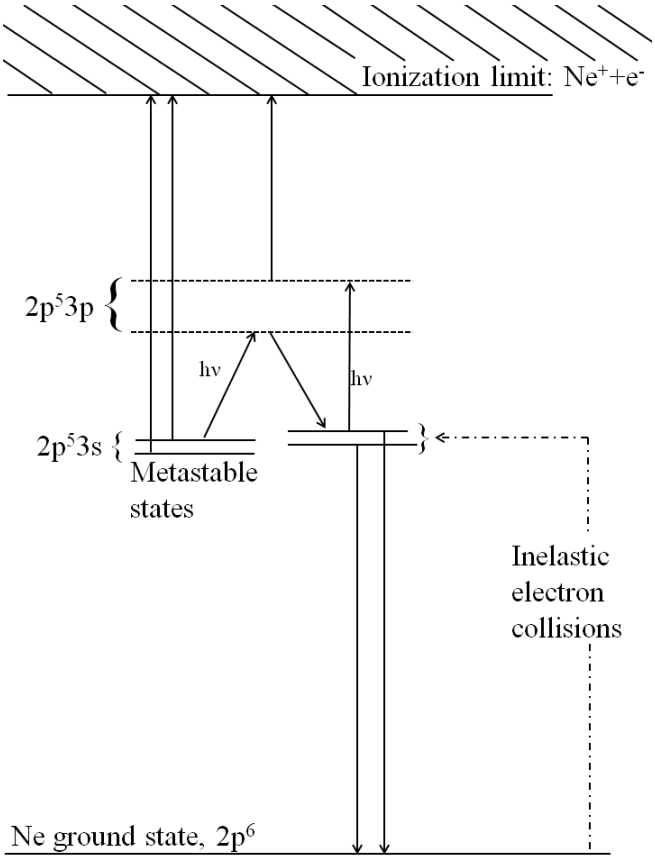

Figure 2.5: Schematic diagram of the mechanisms of relavant to the optogalvanic effect in Ne.

CHAPTER 3

ARRAYS OF GLASS MICROPLASMA DEVICES

Early studies of microplasmas focused on direct current (DC) excitation of single microcavity plasma devices [20] and successfully demonstrated stable operation of microplasmas having characteristic dimensions of less than 100 μm [21]. Several attractive aspects of microcavity plasmas, including power loadings as large as hundreds of kW/cm^{-3}, stable operation at atmospheric pressure and ballast-free operation have been demonstrated [22, 23]. However, DC-excited microplasma devices are severely limited in several respects, one of which is lifetime as a result of electrode sputtering. Thus, alternating current (AC) arrays of microplasma devices are promising for a wide range of applications, particularly those situations where lifetime and and the purity of gas flow are critical factors. Arrays of microplasma devices fabricated on glass are of particular interest both in research and applications because of its transparency in the visible, chemical resistance, and dielectric and mechanical strength. The general features of sodalime glass are summarized in Table 3.1.

Table 3.1: Properties of Sodalime Glass

Chemical Durability	3–4 in hydrolytic class
Dielectric Strength	9.8–13.8 MV/m
Young's Modulus	70±2 GPa
Dielectric Constant	7.6 @25 °C and 1 MHz
Softening Temperature	575 °C

3.1 Fabrication of Arrays of Glass Microplasma Devices

The ability to be able to fabricate reproducibly microchannel or microcavity plasma devices over a large substrate of large array is critical to any effort to explore their optical and electrical properties. Well-established semiconductor microfabrication and semiconductor and micro-electro-mechanical systems (MEMS) fabrication techniques of Illinois originally provided me stimulus for research on arrays of microplasmas. The mechanical strength and inert nature of glass, however, pose a challenge to realizing a low cost and high resolution micromachining process suitable for fabricating microchannel and microcavity devices.

The isotropy of wet etching precludes obtaining high aspect ratios although the process is well developed for quartz or pyrex. Inductively coupled plasma reactive ion etching (ICP-RIE) enables aspect ratios of up to 10:1 for silica and glass [24]. Its etching rate is less than 1 μm/min at optimized conditions [25, 26]. Femtosecond laser micromaching may be an alternative, but this technique is also limited in that an etching rate of 30 nm per pulse is achieved at a fluence of 800 mJ-cm^{-2} [27]. An alternative candidate for precision micromachining of glass is micropowder blasting. This fabrication technique offers low cost, etching rates up to $\sim$100 μm/s, feature size of tens of μm and an aspect ratio $>$ 1:1 [28].

Mask materials and masking schemes are essential for precision fabrication with micropowder blasting, and several different approaches have been investigated [28, 29]. A polydimethylsiloxane (PDMS, DuPont Sylgard 184) mask requires cumbersome SU8 processing in a cleanroom environment. Also, the SU8 structure can be damaged in a wet-and-drag process. The mask material (a flexopolymer) demands expensive photolithographic processes. To render the powder blasting strategy simpler and cheaper, a high-resolution and non-lithographic scheme using ultraviolet (UV) curable polymer and soft lithography is proposed and illustrated in Figure 3.1. First, a silicon master wafer having the desired pattern is fabricated. Photolithographic processes transfer the patterns onto a silicon wafer. After a post-bake process (5 min at 125 °C), 40 μm deep trenches are produced by an inductively-coupled plasma (ICP) reactive ion etcher (RIE). The depth of the patterns can be further optimized according to the minimum feature size of the patterns. A standard

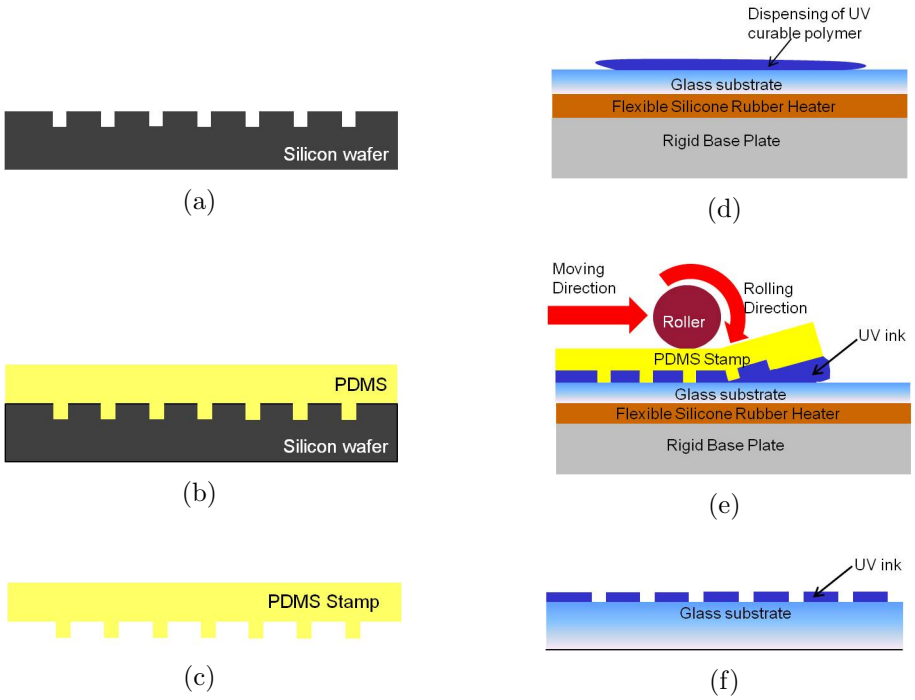

Figure 3.1: Illustration of high-resolution mask fabrication for micropowder blasting: (a) the silicon master mold is fabricated by photolithography and ICP-DRIE; (b) PDMS is poured onto the master mold after surface treatment of the master wafer and is thermally cured; (c) the PDMS daughter mold is released from the master; (d) UV curable polymer is dispensed on a glass substrate at 40 °C; (e) a high-resolution mask is replicated from the daughter mold by an imprinting process and is cured by UV light; and (f) the daughter mold is peeled off from the substrate, yielding a high-resolution mask.

degreasing process using acetone/isopropyl alcohol (IPA) and plasma ashing are used to completely eliminate the photoresist film. Then, a flexible PDMS daughter mold is replicated from this master mold. The surface of the wafer is treated by dimethyldichlorosilane (Repel Silane, Amersham Bioscience) to prevent the PDMS mold from adhering to the waver. The liquid PDMS is poured into a square metal frame placed on top of the silicon wafer, thermally cured at 120 °C for 4 hours, and peeled off from the hydrophobic layer of the wafer produced by the Repel Silane treatment. A mask layer is then defined by the flexible mold for micropowder blasting. The glass substrate is placed on top of a flexible heater, and it is warmed up to 40 °C. Ultraviolet (UV) curable polymer (GEC-10H, Jujo Chemical) is dispensed onto the glass substrate and the stamp is imprinted by rolling. The stamp and substrate are pressurized with a contact force of a few newtons, and cured in a 400 W UV exposure system. The stamp is released and can be reused more than 50 times. A high-resolution mask is produced by this strategy. Micropowder blasting then etches microcavities or microchannels on a glass substrate.

Micropowder blasting has been attractive, especially for industrial applications, because of its features such as a cost effectiveness and etching rates up to and beyond 100 μm/s. The fundamental mechanism of this etching is a brittle erosion process in which a material is eliminated by crack formation. The area associated with the impact of micropowder particles is plastically deformed because of high compressive stress when a hard sharp particle collides with the surface of a brittle material. A radial crack is produced in this process and, hence, large tensile stress, which causes lateral cracks. The material is finally removed by the subsequent impacts [30].

The micropowder blasting system is illustrated schematically in Figure 3.2. A Comco Microblaster (MB 1002, Comco Inc.) and alumina oxide (Al_2O_3) particles having a diameter of 9 μm and 17.5 μm were used. The microblaster was connected to a pressurized nitrogen gas tank providing backing pressures up to 120 psi. The nitrogen gas hinders the agglomeration of fine particles of Al_2O_3. Alumina oxide powder is fed to the nitrogen gas stream from a pressurized reservoir through an orifice where mixing occurs and the powder/N_2 mixture is accelerated. The particles impinge on the sample substrate with a velocity >100 m/s. A motorized, two dimensional stage operated by a computer with Labview was designed to obtain uniform coverage over an area >40 cm^2. The distance between the nozzle tip and the substrate was fixed

at 2 cm and the backing pressure was set at 30 psi.

Figure 3.3 comprises four scanning electron micrographs (SEMs) illustrating the cross-sectional or top view of etched structures. Figure 3.3(a) shows an end-on view of a portion of an array of 10 microchannels with linear tapered sidewalls, a width of 120±2 μm, depth of 140±5 μm and a channel pitch of 200 μm. Arrays of rounded square shaped microcavities with a 180±5 μm diagonal and depth of 100±3 μm are shown in Figure 3.3(b). The cross section resembles a half-ellipsoid. Figure 3.3(c) illustrates the minimum feature size of 25 μm that has been demonstrated by this fabrication approach and the cross section of the microchannel is similar to that of a half-ellipse. A microchannel having a semicircular cross-section is shown in Figure 3.3(d). The channel width is 550 μm. The RMS roughness of the channel sidewalls is estimated to be ~3 μm. Smaller diameter alumina particles and post-annealing of a substrate are expected to improve the surface morphology. These SEMs confirm that the proposed glass micromachining process using soft-lithography and micropowder blasting has been demonstrated successfully.

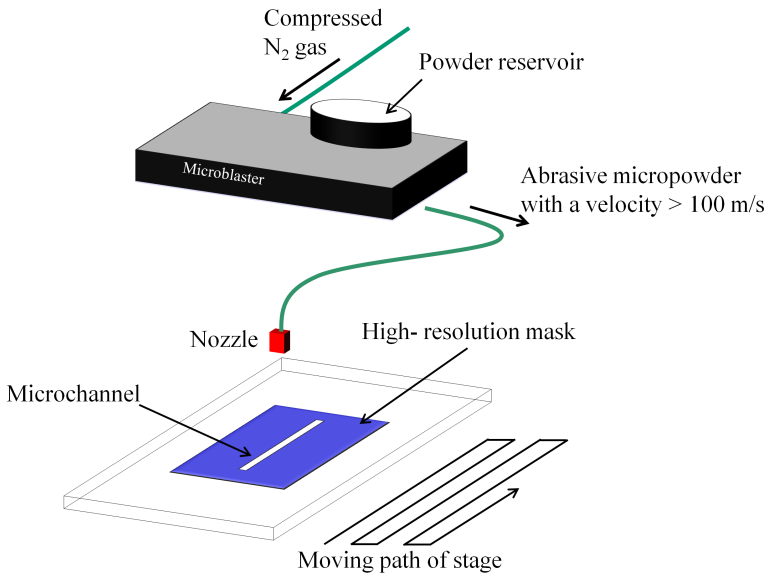

Figure 3.2: Schematic illustration of the micropowder blasting system.

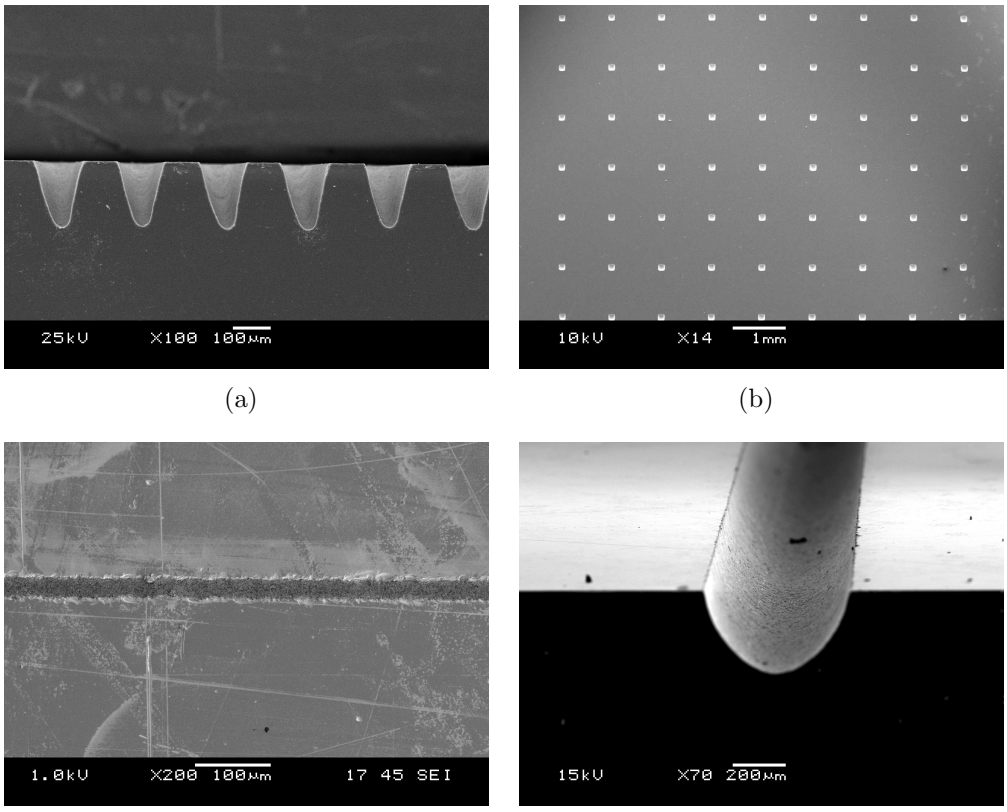

(a) (b)

(c) (d)

Figure 3.3: Scanning electron micrograph (SEM) images: (a) portion of an array of 120 μm wide and 150 μm deep microchannels; (b) array of microcavities with a diagonal of 180 μm and a depth of 100 μm; (c) a 25 μm wide and 2.5 cm long microchannel; (d) end-on image of a 500 μm wide microchannel which resembles a half-circle.

3.2 Structures of Glass Microplasma Devices

Glass microplasma devices are a family of dielectric barrier discharges in that one or both electrodes are covered by a dielectric layer. It is notable that, to utilize the benefits of the high dielectric strength of glass, a patterned glass substrate serves as a dielectric layer for our microplasma devices. This also eliminates the necessity for the subsequent sputtering or deposition of dielectric layers. Three representative structures were designed for the investigation of the underlying physics of microplasmas and their applications such as antennas, UV-IR optical emitters and water/air purifications.

Schematic diagrams for several genres of glass microplasma devices are illustrated in Figure 3.4. In the design of Figure 3.4(a), two patterned substrates having half-ellipsoidal cavities or channels were aligned and hermetically sealed. Metal layers of titanium (Ti) and nickel (Ni) were evaporated on the bottom face of the device. The transparent electrode of indium tin oxide (ITO) was sputtered onto the top surface, and annealed at 270 °C for 20 minutes. These two metal layers serve as electrodes. This design has thick dielectric layers (>100 μm) and a driving sinusoidal voltage >10 kV_{p-p} at a frequency of 20 kHz. The difference between the structure of Figure 3.4(a) and Figure 3.4(b) is the gap intentionally introduced between the substrates. The gap distance was optimized for the investigation of the electrical properties of microcavity plasmas and the interaction of microcavity plasmas with microgap plasmas. Figure 3.4(c) has only one patterned glass substrate. The metal layers of Ti (30 nm) and Ni (200 nm) are evaporated before the mask fabrication procedure, illustrated in Figure 3.1(d), and are subsequently patterned by the micropowder blasting process. The metal layer is photolithographically patterned to decrease the displacement current for the device. The etched glass substrate is hermetically sealed with an optical window. Evaporation of Ti (30 nm) and Ni (200 nm) films produces another electrode. This design does not require an alignment process, and this has, accordingly, been widely used for glass microplasma devices having characteristic dimensions of $\leq$200 μm. The operating voltage for the structure of Figure 3.4(c) is only $\sim$6.5 kV_{p-p} at a frequency of 20 kHz because the metal pad in between two glass wafers may contact the microplasmas, thereby eliminating the voltage drop required when a dielectric is present.

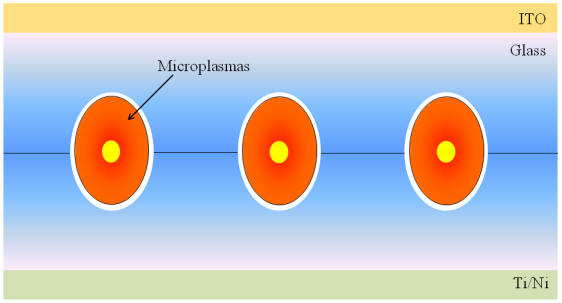

(a)

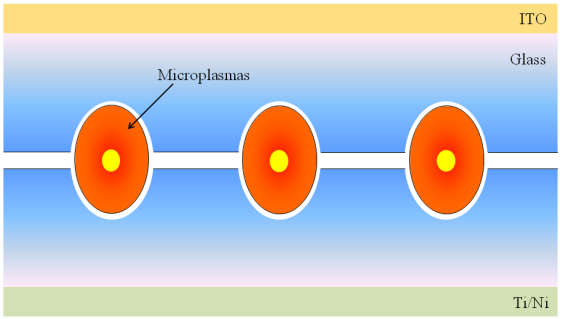

(b)

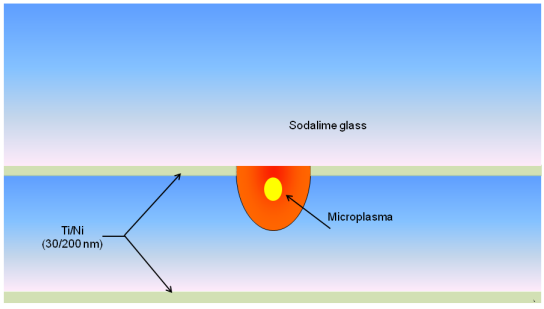

(c)

Figure 3.4: Structures of several ellipsoidal microcavity/microchannel plasma devices: (a) symmetric ellipsoidal microplasma devices; (b) symmetric ellipsoidal microplasma devices with a micro-gap; (c) asymmetric half-ellipsoidal microplasma devices.

3.3 Characterization of Arrays of Glass Microplasma Devices

3.3.1 Electrical Characterization of Arrays of Glass Microplasma Devices

The electrical properties of microplasmas were investigated with the symmetric microcavity plasma devices illustrated in Figure 3.4(a). Both top and cross-sectional views, with dimensions indicated, are provided in Figure 3.5. The voltage-current (V-I) characteristics for the structure are shown in Figure 3.6. The RMS currents (I_{TOTAL}) in Figure 3.6(a) include both a displacement current and discharge current. The RMS discharge current ($I_{DISCHARGE}$) in Figure 3.6(b) is the RMS value of the current when the contribution of displacement has been subtracted from the total current. The effective capacitance of arrays of microcavity plasma devices can be approximated from the slope of the V-I plot by the relation

$$C_{eff} = \frac{I_{vac}}{V_{vac}} \cdot \frac{1}{2\pi f} \tag{3.1}$$

where C_{eff} is an effective capacitance, I_{vac} is the displacement current with vacuum in the microcavities, V_{vac} is the voltage in vacuum, and f is the frequency of the applied input voltage. The vacuum data for the tested device yields a capacitance of 38±2 pF for an array with an active area of 2.5×2.5 cm^2.

Notice that the turn-on (ignition) voltage (entire array operating) increases from 410 to 450 V_{RMS} when the Ne pressure is increased from 100 to 700 Torr. The I-V curves of Figure 3.6 have features similar to those of all other types of glass microplasma devices in that: (1) higher currents were observed at higher pressures above a threshold voltage for the pressures of 100–700 Torr, and (2) the operating voltage was larger than ∼1100 V_{RMS}.

The operating mode of the microplasmas in this device can be understood from the slope of the discharge current versus the applied voltage. The curves clearly show positive differential slopes for operating pressures and voltages, as has been observed previously in other microplasma devices [22, 23]. This positive differential slope guarantees ballast-free operation, and a detailed discussion of this behavior can be found in several articles [31, 32]. One

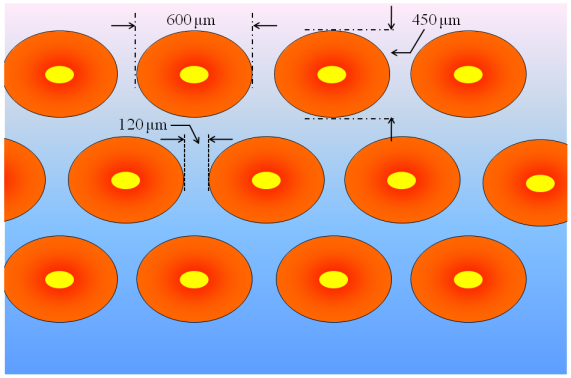

(a)

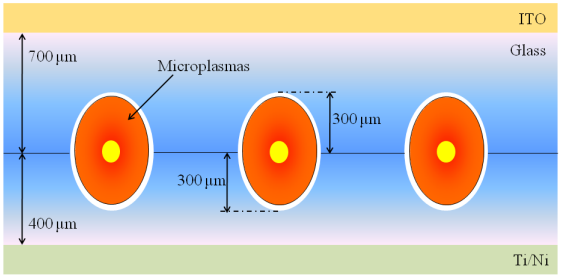

(b)

Figure 3.5: Structure of ellipsoidal microcavity devices: (a) top view of arrays of microcavities; and (b) cross-sectional diagram of the overall device.

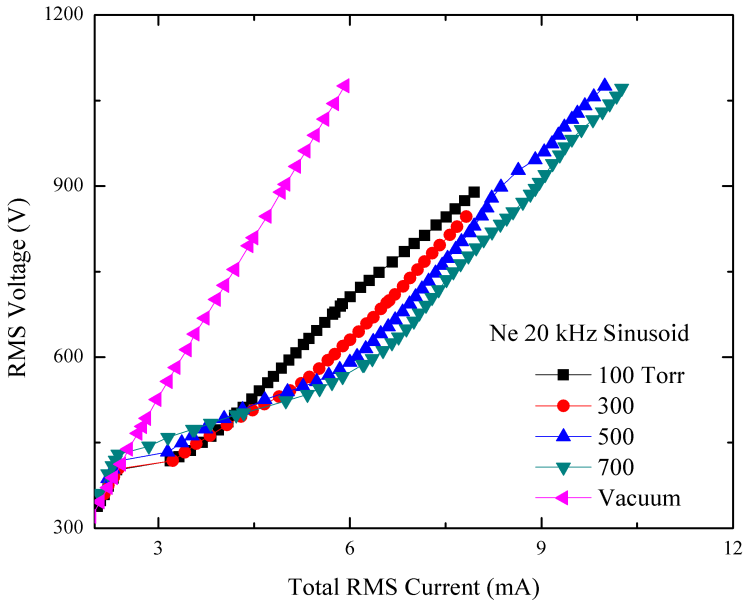

(a)

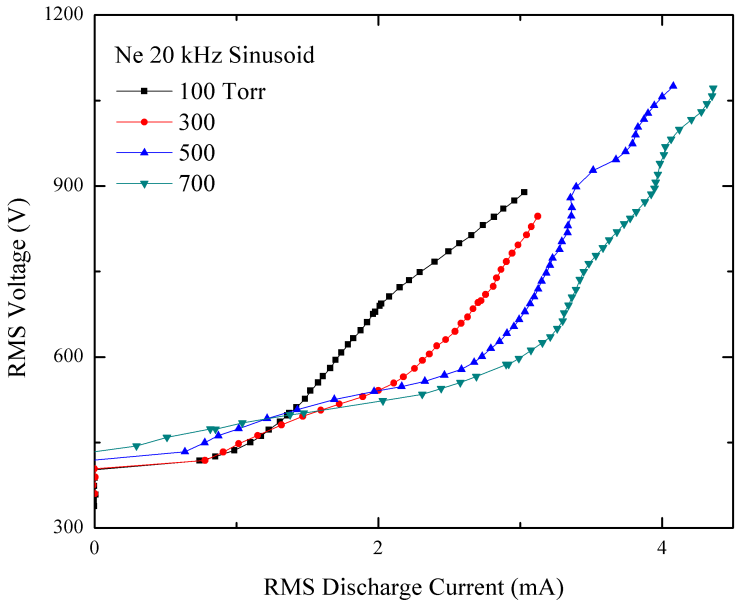

(b)

Figure 3.6: Voltage-current (V-I) characteristics of arrays of ellipsoidal microcavity plasma devices having an overall active region of 2.5 cm × 2.5 cm: (a) V-I_{TOTAL} characteristics; (b) V-$I_{DISCHARGE}$ characteristics. I_{TOTAL} is the sum of the displacement and discharge currents and $I_{DISCHARGE}$ is the discharge current.

interesting observation from the curves of Figure 3.6 is that the slopes change abruptly above $\sim$560 V_{RMS} for Ne pressures of 300, 500 and 700 Torr and are almost same. For a given voltage, the current increases with increasing pressure in the 100 to 700 Torr range when the slopes are the same. This observation is in agreement with theoretical predictions [5]. In addition, the higher pressure leads to a higher slope in the region below $\sim$560 V_{RMS}. These observations imply that the operating mode of the arrays of microplasmas changes at this juncture. V-I curves are well-known to be excellent indicators for the mode of operation of DC plasmas, but the situation for AC DBD plasmas is less clear because of the effect of dielectric layers. In this latter case, it is preferred to study the temporal evolution of the applied voltage, gas voltage, total current and discharge current. The dilemma in the research of microplasmas, however, is the determination of the capacitance of the dielectric layers owing to the complicated geometry of microcavity plasma devices [33, 34]. Thus, later in this dissertation, a modified structure of Figure 3.4(b) is introduced to further investigate modes of operation and the results will clearly show a transition between operating modes of the plasma.

3.3.2 Optical Characterization of Arrays of Microplasmas

Optical characterization techniques such as imaging and emission spectroscopy provide a non-invasive tool to investigate microplasmas. High-resolution photography is, for example, a convenient diagnostic to study the stable operation of plasmas. Optical emission spectra also provide information such as discharge dynamics and chemical reactions in plasmas. This section deals with the stable operation of arrays of microplasmas, and the observation of frequency and voltage dependent UV/visible emissions. The emission spectra from ambient air microplasmas are also discussed. Both air microplasmas and the UV emission from such plasmas are of particular importance for a wide range of applications in biomedicine and environmental issues.

Optical micrographs of microcavity and microchannel plasma devices are displayed in Figure 3.7 and Figure 3.8. These micrographs, aside from Figure 3.8(b), were recorded by a 10$\times$ optical microscope in tandem with a CCD camera having a pixel resolution of 2.3$\times$2.3 μm^2. Figure 3.8(b) was recorded by a commercial digital camera because the CCD was not sensitive

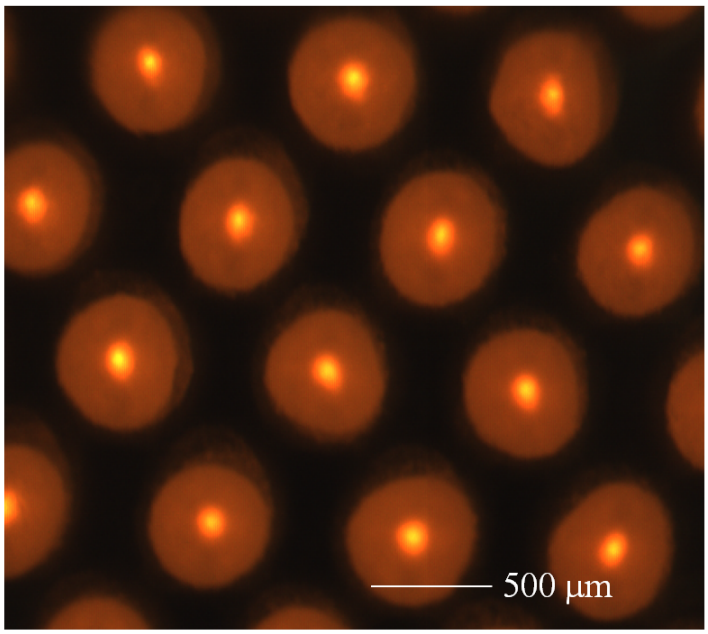

(a)

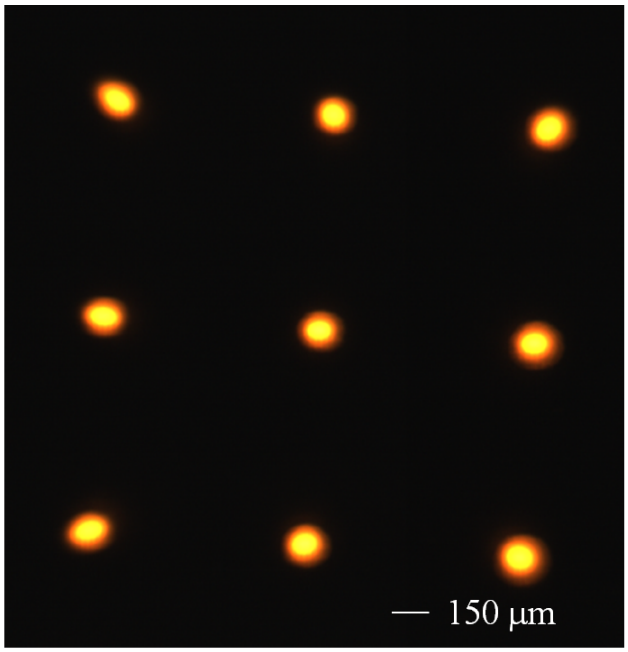

(b)

Figure 3.7: Optical micrographs of arrays of microcavity plasma devices: (a) ellipsoidal microcavities with axes of 650 μm$\times$450 μm with a depth of 300 μm in Ne 300 Torr; and (b) hemisphere microcavities with a diameter of 150 μm in Ne 300 Torr.

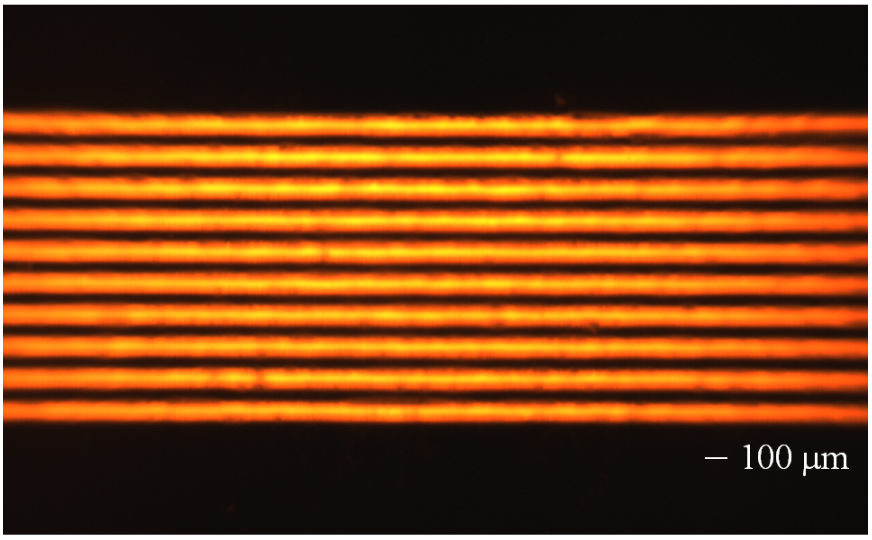

(a)

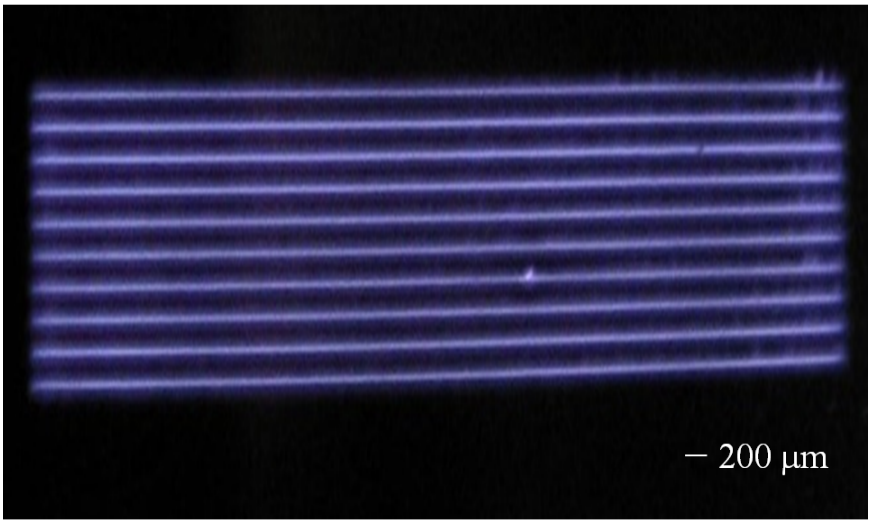

(b)

Figure 3.8: Optical micrographs of arrays of microchannel plasma devices: (a) half-ellipsoidal microchannels with a width of 100 μm and depth of 150 μm in Ne 700 Torr; and (b) half-ellipsoidal microchannels with a width of 200 μm and depth of 250 μm, operating in ambient air.

in the ultraviolet and blue regions. A 20 kHz sinusoidal voltage was used to drive these microplasma devices. Figure 3.7(a) illustrates the operation of an ellipsoidal microcavity plasma device operating in 300 Torr of Ne. Two glass substrates having arrays of half-ellipsoidal microcavities (major and minor axes of 700 μm $\times$ 500 μm) with a depth of 300 μm were aligned so as to form ellipsoidal microcavities. The operation of a hemisphere microcavity plasma device with a diameter of 150 μm and a depth of 150 μm is shown in Figure 3.7(b) for operation in 300 Torr of Ne. Figure 3.8(a) shows the operation in 700 Torr of Ne for a half-ellipsoidal microchannel plasma device having a width of 100 μm and a depth of 150 μm in 700 Torr of Ne. The microchannel in Figure 3.8(b) has a width of 200 μm and depth of 250 μm and it is in operation in ambient air. Spatially confined, uniform glows in the structures described in Figure 3.4 have been generated both in microcavities and microchannels with several noble gases and gas mixtures, including ambient air.

A number of atomic and molecular transitions have been investigated in glass microplasmas since the initial demonstration of the stable operation of glass microplasma devices. UV emission (200–390 nm) in Ar/1% N_2 gas mixtures and ambient air and visible emissions (390–750 nm) in Ne gas are among those that have been studied. Both the Ar/N_2 system and Ne have been examined extensively for decades and are well understood, and they have been adopted to characterize the optical emissions of microplasmas. Argon-N_2 mixtures produce intense emission in the $\nu' \rightarrow \nu''$=0–4 bands of the $C^3\prod_u \rightarrow B^3\prod_g$ transition of N_2 (second positive system) and, in Ne plasmas, 3p $\rightarrow$ 3s transitions are most intense.

Figure. 3.9 shows the voltage-dependent characteristics of UV emissions in Ar/1% N_2 gas mixtures. A 20 kHz driving frequency was chosen for the tests. The lowest measured voltage at each pressure was higher than the turn-on voltage by 100 V_{RMS}. The breakdown voltage significantly increased when increasing the total pressure from 300 to 600 Torr. The measured voltages were from 900 V_{RMS} for p_{TOTAL}=300 Torr to $\sim$1350 V_{RMS} for p_{TOTAL}=600 Torr. This implies that all tested pressures at given dimensions lie on the right side of Paschen's minimum. It is observed that there are three different regimes in the UV emissions. The 300 Torr curve, for example, has three different slopes in the 900–1200, 1200–1300 and 1300–1650 V_{RMS} voltage ranges. The data for 400 and 500 Torr also show similar features, but the

600 Torr data are somewhat unclear because of the range in the tested voltage. The changes in the slopes of Figure 3.9 may correspond to the changes in the electrical properties of microplasmas, as the V-I characteristics of Figure 3.6 indicate. One possible reason for the abrupt increase of UV output is the existence of a positive column in the microplasma at the voltage range of 1300–1650 when the Ar/1%N_2 operating pressure is 300 Torr.

The efficiency for generating UV differs for plasmas operating as a glow

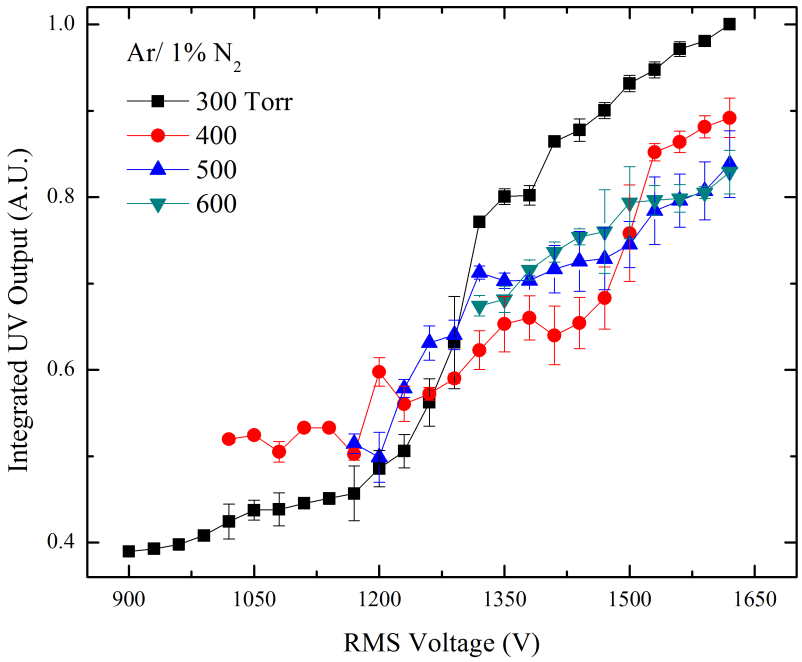

Figure 3.9: Dependence on applied voltage of the integrated UV output intensity (200–380 nm) from arrays of symmetric ellipsoidal microcavity plasma devices over the 300–600 Torr pressure range for an Ar/1% N_2 gas mixture.

or in the Townsend region. A simple distinction exists between operation of the plasma as a negative glow or positive column. A simple steady-state, one-dimensional model proposed by R. Ganter et al. [35] offers a rough estimate for the different effeciency of a plasma in the Townsend region and positive column. This model suggests that for a Townsend discharge, the

fraction of the electrical power delivered to the electron is

$$\eta_e = \frac{\int_0^d J_e E \, dx}{J_T E d} = \frac{1}{e^{\alpha d}} \int_0^d e^{\alpha x} \, dx = \frac{1}{(1+\gamma)(\ln((1+\gamma)/\gamma))} \tag{3.2}$$

$$\eta_i = 1 - \eta_e \tag{3.3}$$

In this expression, η_e is the ratio of the power dissipated by the electrons to the total power, η_i is a ratio of a dissipated power by ions to a total power, J_e is a current density of electrons, J_T is a total current density, α is the ionization coefficient and γ is the secondary electron emission coefficient. By examining Equation 3.2, it can be seen that the efficiency for electron heating in a Townsend discharge is only ∼52% even with a secondary electron emission coefficient of 0.3. The electron and ion density in the positive column are calculated by the drift of the electrons and ions, respectively. The fractional power of electrons is changed into the following expression:

$$\eta_e = \frac{\mu_e}{\mu_e + \mu_i} \tag{3.4}$$

where μ_e is the mobility of electrons and μ_i is the mobility of ions. In general, $\mu_e/\mu_i > 100$. This model may not be sufficient to explain all the underlying physics of microplasmas, but it is beneficial in demonstrating that the efficiency for electron heating of a positive column is much higher than that for a Townsend discharge. The abrupt increase of UV output in Figure 3.9 can be understood in this context.

Neon is of particular interest because its strong visible emissions provide an opportunity to investigate the underlying physics of microplasmas by non-invasive imaging techniques. The frequency dependent and voltage dependent visible emissions are illustrated in Figure 3.10. The relative intensities of an emission spectrum in 390–750 nm were integrated and compared. Figure 3.10(a) describes a frequency dependent visible emission in the neon plasmas. The amplitude of the applied voltage was set to 500 V_{RMS} for all the frequencies. The visible output increases with increasing frequency for all pressures of 300–700 Torr. The increase of visible emissions from neon plasmas generally corresponds to the population of neon excited states because I∝NA$\hbar\omega$. The input power into plasmas linearly increases as the driving

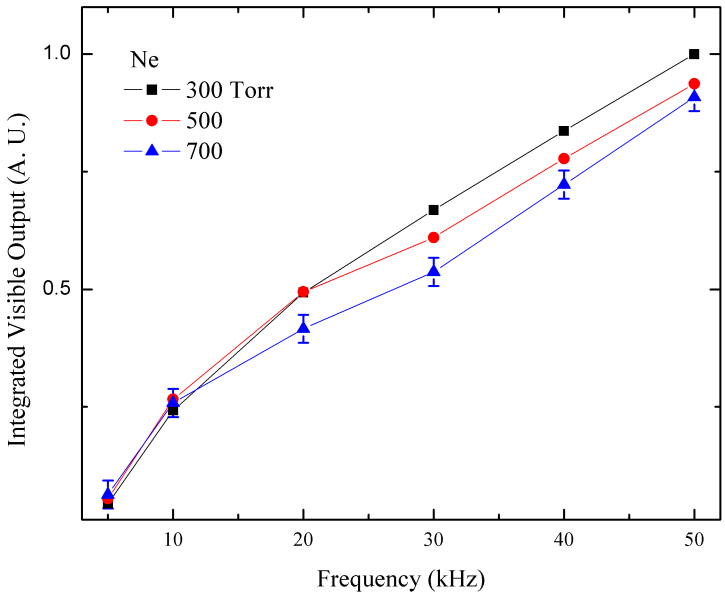

(a)

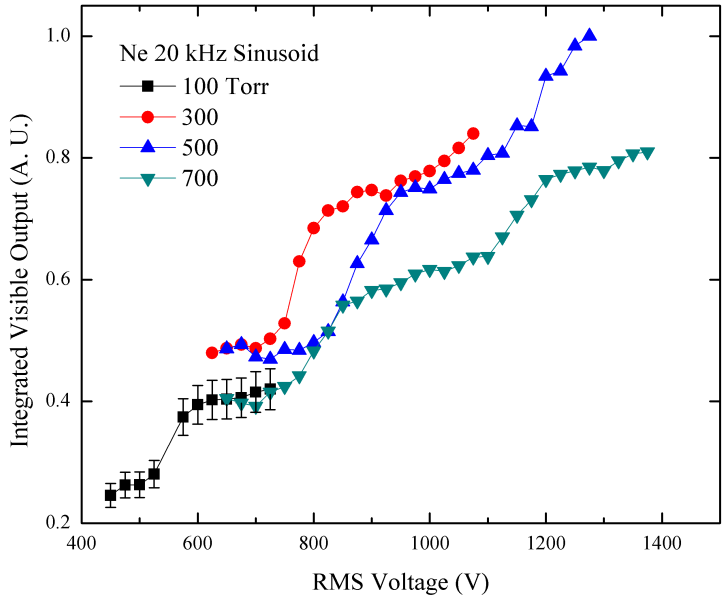

(b)

Figure 3.10: Dependence of visible emission intensity on: (a) operating frequency, and (b) applied voltage.

frequency increases and this leads to the increase of the visible output. The visible output of a frequency range of 30–60 kHz also decreased with an increasing pressure from 300 to 700 Torr. Collisional frequency is proportional to pressure. A electron cannot produce excitation or ionization of atoms or molecules if it collides with other species before getting enough energy for the processes. This collisional loss is the reason for the decrease of visible output. The voltage dependent visible outupt is illustrated in Figure 3.10(b). The region that shows an abrupt increase of visible emissions was observed for pressures between 100 and 700 Torr of Ne. The sudden increase in the visible intensity is caused by multiple breakdown events of plasmas. The discharge current of plasmas is created at a breakdown voltage and increases with an increasing voltage. The current pulse, however, is inhibited by the charge recombination on the dielectric layer and collisional losses and decays to zero. The FWHM of a discharge current in glass microplasma devices operating in hundreds of Torr is approximately several μs if it is abnormal glow-like discharge. Another current pulse occurs if the driving voltage keeps increasing and dV/dt is sufficiently high to create another breakdown. The second pulse also leads to the visible output. The evolution of a current in 700 Torr of Ne is given in Figure 3.11. The visible output increases by $\sim$50 % when an RMS voltage rises from 650 to 1000 V. The number of a current peak of 650 V_{RMS} is one and that of 1000 V_{RMS} is three. It has two current peaks at the voltage of 800 V_{RMS} where an abrupt increase exists. The peak of a current pulse has terminated since the dV/dt decreased. The multiple peaks of the current of Ne 700 Torr start from the voltages of 600, 700 and 850 V_{RMS}. The differences of RMS voltages are 100 and 150 V and they are much lower than the first breakdown voltage of 600 V_{RMS}. Several excited species, such as metastable atoms of Ne, play a critical role in this. It is also observed that the intensity of multiple current peaks decreases and it is caused by recombination on the surface of the dielectric layers.

The distinct characteristics of arrays of glass air microplasmas are low temperature and atmospheric operation. For example, a plasma ozone generator prefers low temperature operation because the lifetime of ozone molecules decreases with increasing temperature. Atmospheric pressure operation also helps the formation of ozone, which is produced by three- body collisions between an oxygen atom, an O_2 molecule and a third party of O_2 or N_2. The capability to fabricate large-area, high dielectric strength, and low sputter

rate glass is another asset of glass microplasma devices. The emission spec-

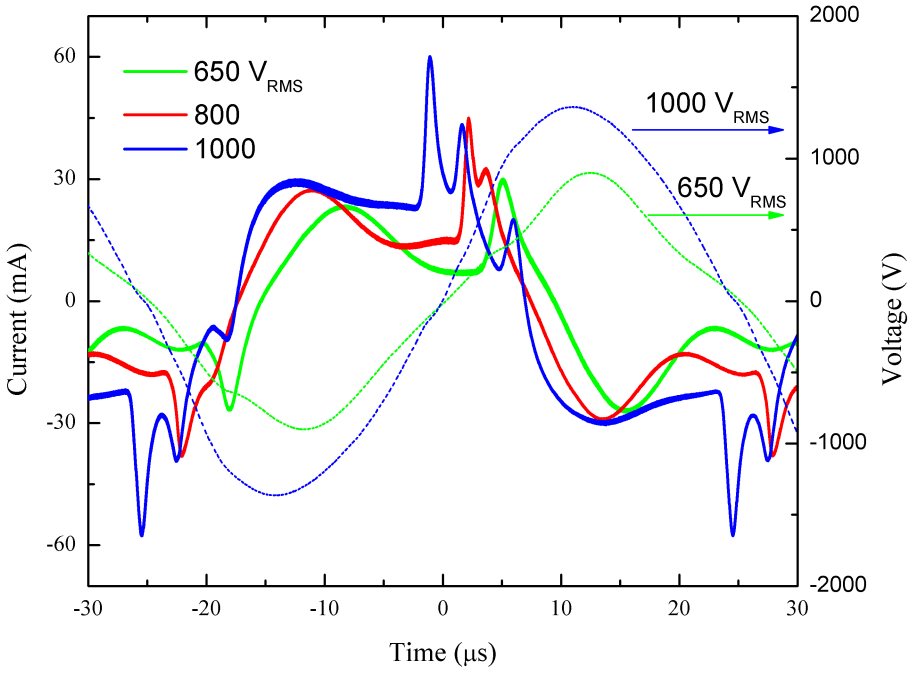

Figure 3.11: Temporal response of the current for an RMS voltage of 650, 800 and 1000 V in 700 Torr of Ne.

tra of ambient air microchannel plasmas in the middle ultraviolet (200–290 nm) and near infrared (700–800 nm) range are displayed in Figure 3.12 with an emphasis on oxidants such as NO, OH and O. Reactive chemical species of $NO_{\beta,\delta,\gamma,\varepsilon}$, O_2 ($A^3\sum_u^+(\nu' = 0) \rightarrow X^3\sum_g^-(\nu'' = 2)$) and OH ($A^2\sum^+ \rightarrow X^2\prod$) are recognized in the middle ultraviolet region. The subscripts of β, δ, γ and ε of NO are four band systems of $B^2\prod \rightarrow X^2\prod$, $A^2\sum^+ \rightarrow X^2\prod$, $C^2\prod \rightarrow X^2\prod$ and $D^2\sum^+ \rightarrow X^2\prod$, respectively. Ultraviolet B (UVB, 280–315 nm) is especially effective for the production of vitamin D on the skin and treatment of psoriasis and vitiligo [36]. Gaseous NO also helps wound healing by initiating a strong antioxidant reaction from the treated tissue [37]. In addition, strong emission of the first positive bands of N_2 ($B^3\prod_g(\nu'$=3–6) $\rightarrow$ $A^3\sum_u^+$ (ν''=1–4)) and the oxygen atom ($3p^5P \rightarrow 3s^5S$) were observed in the mid infrared (IR). These reactive radicals are of particular interest as effective oxidants and they play a significant role in water purification [38] and the decontamination of chemical or biological warfare agents [39]. Thus, arrays

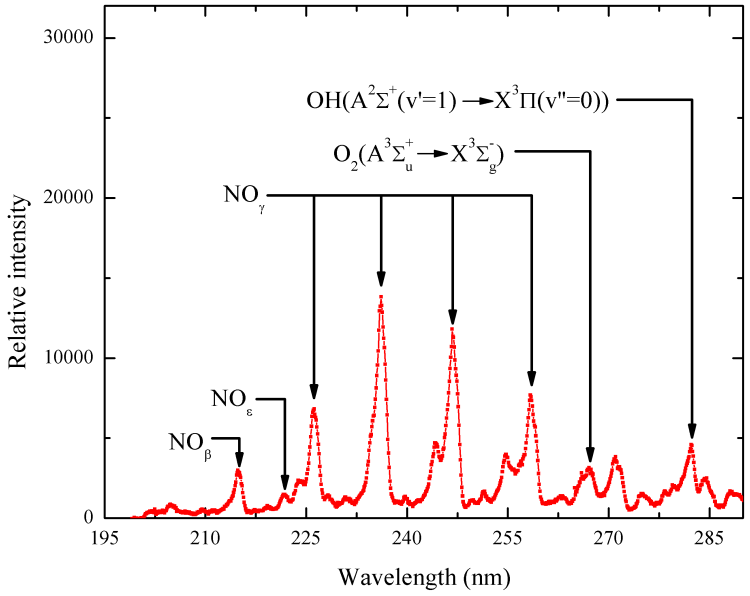

(a)

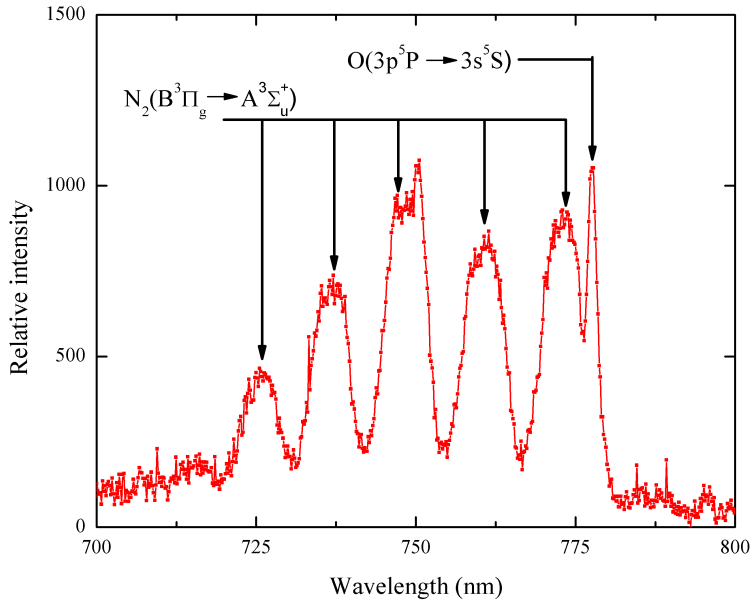

(b)

Figure 3.12: Emission spectra from ambient air microchannel plasmas: (a) mid-ultraviolet (200–290 nm) spectral region; and (b) near infrared (700–800 nm) spectral region.

of microplasmas with a high throughput would be a promising candidate in these applications.

3.3.3 Gas Temperature Measurements of Glass Microchannel Plasmas

The gas temperature is an important parameter in characterizing plasmas. Chemical reactions in plasmas cannot be fully understood without the knowledge of the gas temperature. The diagnosis of microplasmas, however, is elusive because direct probing with an instrument such as a Langmuir probe may not be accurate because it strongly perturbs micron scale plasmas. Non-invasive techniques such as optical emission spectroscopy (OES), laser-induced fluorescence (LIF) and coherent anti-Stokes Raman scattering (CARS) are powerful tools for studying temperature. The simplicity and low cost of OES make it more attractive than the others. In these experiments, OES was used to estimate the microplasma neutral gas temperature from measurements of partially-resolved rotational structure in the emission spectra of diatomic molecules. The rotational temperature of N_2 and O_2 has been widely used in estimating plasma gas temperature. However, several experiments [40] have shown that measured rotational temperatures from those gases overestimate the gas kinetic temperature. The (ν',ν''=0,0) transition of OH A$\rightarrow$X from Ar/H_2O system was adopted for the estimation of the gas temperature of glass microchannel plasma devices, illustrated in Figure 3.4(c). The concentration of the minority constituent of water vapor in the tests was <1%. The microchannel of the tested device had a width of 200 μm, a depth of 200 μm and a length of 2.5 cm. The OH transition in a Ar/H_2O system generates strong fluorescence because the Rydberg levels of water molecules are resonant with metastable states of argon ($^3P_0$ and $^3P_2$). A previous study [40] has shown that the concentration of water vapor has negligible effect on the estimated temperature. The rotational temperature from the water vapor adsorbed onto a vacuum chamber wall can be a convenient measure of gas temperatures of microchannel plasmas.

A panoramic view of the emission spectrum in the 200–530 nm region is given in Figure 3.13. The partial pressure of H_2O was not quantitatively measured. the experiments relied simply on the trace water concentration present

in the background gas when the system was pumped to a base pressure of $\sim 10^{-7}$ Torr. Strong lines of 307 nm and 308 nm are attributed to OH A→X

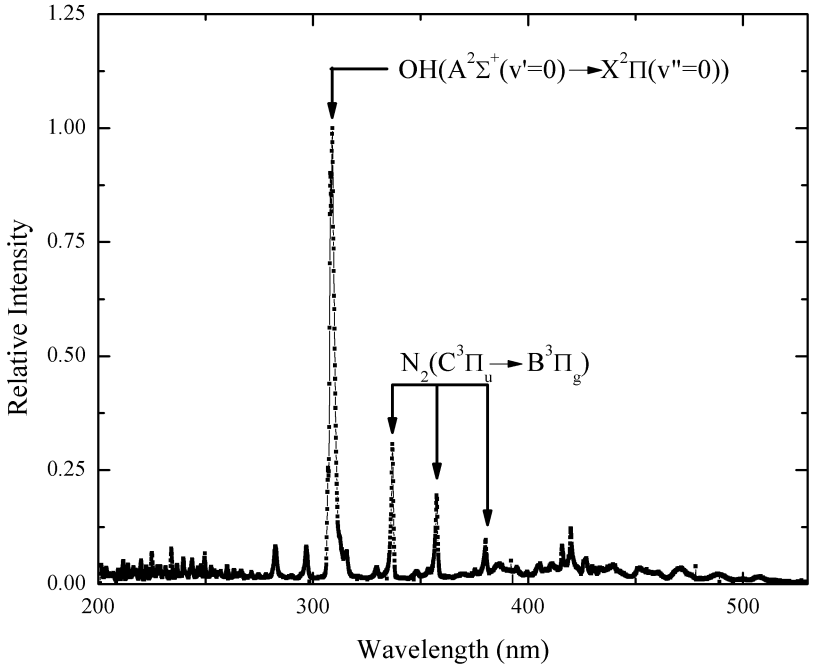

Figure 3.13: Comprehensive view of the emission spectrum from 300 Torr of Ar/H_2O in a single microchannel plasma. The spectral resolution of a detector is ∼0.6 nm.

transitions ((ν', ν'')=(0,0)) and the rotational temperature was assessed from the ratio of these lines. The spectrum also shows the $C^3\prod_u \rightarrow B^3\prod_g$ transition from impurity of N_2. The excited Ar also populates the $C^3\prod_u$ excited state of N_2 and the spontaneous radiative decay of N_2(C) leads to the vibrational transitions at 315 nm, 337.1 nm, 357.7 nm and 380.5 nm in the spectrum. To study gas temperatures of microchannel plasmas, emission spectra from Ar/H_2O mixtures have been measured at pressures of 100–700 Torr. Spectra were recorded five times at each pressure. The results were also compared with a simulation code of OH(A(ν'=0)→X(ν''=0)), developed in [41]. To simulate the observed spectra, the 108 rotational lines [42] of the (ν',ν''=0,0) transition of OH(A→X) were convolved with a Gaussian distribution function with the FWHM of the detector (0.6 nm). An example of the process for estimating the rotational temperature of microplasmas in 300

Torr of Ar/H_2O vapor mixtures is provided in Figure 3.14. The measured

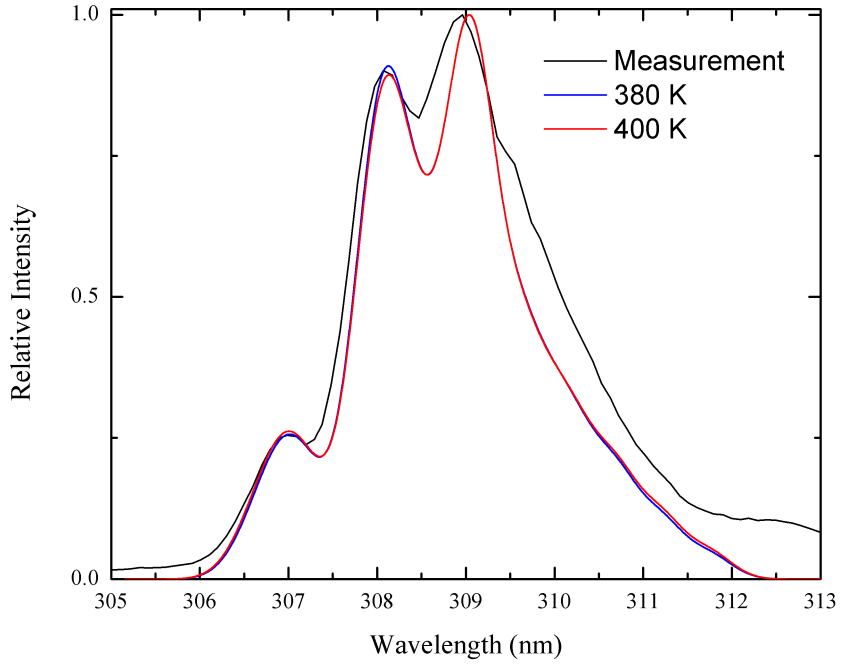

Figure 3.14: The measured and simulated spectra of OH A→X transition ((ν',ν'')=(0,0)) from Ar/H_2O vapor mixtures. The calculated spectra are for rotational temperature temperatures (T_R) of 380 K (blue) and 400 K (red).

spectra are normalized with respect to maximum intensity. The rotational line which corresponds to 309 nm is strongest. The simulated spectra were generated with increasing rotational temperature with a step size of 10 K and the lower and upper bound of the temperature are selected when the ratio of the rotational line envelope intensity at 308 nm to 307 nm is higher and lower compared with the ratio of the lines from the measured data. The error in accuracy of the example is predicted to be ±10 K. A summary of the rotational temperature data for microchannel plasmas is provided in Figure 3.15. At a voltage of 1400 V_{RMS}, estimated rotational temperatures of 100, 300, 500 and 700 Torr are 410, 385, 403 and 395 K, respectively. Their estimated uncertainties are ±10, 15, 13 and 18 K. The tested microchannel plasmas, regardless of the pressure of the Ar/H_2O vapor system, showed temperatures of 385–410 K. The fact that the gas temperature $\lesssim$100 K above ambient is ben-

eficial for applications, including antennas and chemical decontaminations.

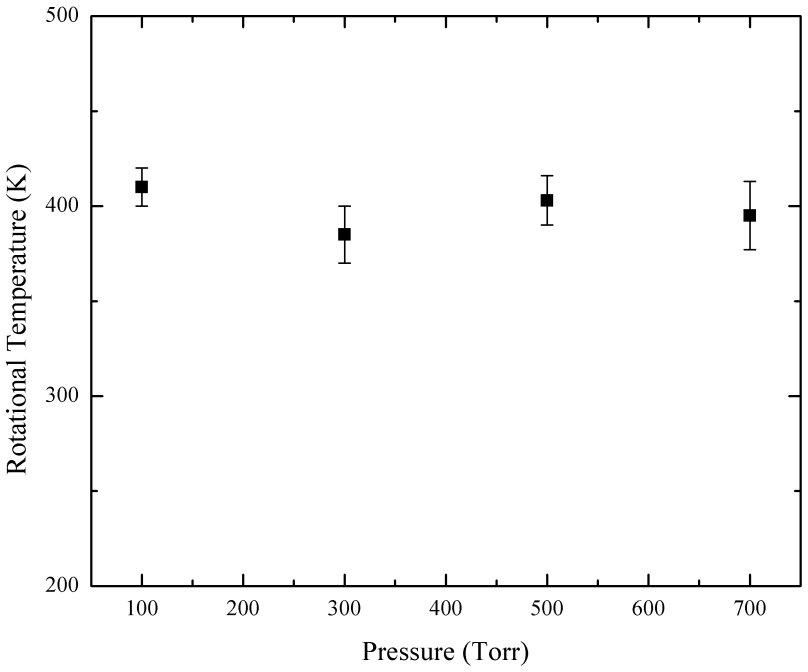

Figure 3.15: Rotational temperatures measured from 200 μm wide and 200 μm deep half-ellipsoidal microchannel plasmas in the pressure range of 100–700 Torr for Ar/H_2O vapor gas mixtures.

CHAPTER 4

COUPLING PHENOMENA IN ARRAYS OF GLASS MICROPLASMA DEVICES

Interest in microplasma research has grown dramatically in the last 15 years. Microplasmas are now opening new applications in photonics [6], electromagnetics [43], microelectronic processing [44] and biomedicine [45]. However, plasma physics in the spatial domain of 1 μm–1 mm is still not well understood and studies of the underlying physics of arrays of microplasmas are few. One of the compelling aspects of microcavity plasma devices [46] is the opportunity afforded by this technology to investigate collective plasma and optical effects as well as the degree and nature of coupling between a single device and its neighbors. This work provides the first investigation into the intriguing problems of optical and electrical coupling mechanisms in arrays of microplasmas produced in ellipsoidal microcavities or microchannels fabricated in glass. Further optimization of the coupling between microplasmas has significant implications for microlasers, on-chip plasma processing tools and the surface treatment of biomaterials. Coupling provides an opportunity to optically modulate the local field strength in large arrays.

4.1 Optical Coupling in Arrays of Microcavity and Microchannel Plasmas

The structure of Figure 3.4(a) is investigated in these experiments, and Figure 4.1 is a scanning electron micrograph (SEM) illustrating one-half of an ellipsoidal cavity in cross section. Photographs of a portion of an array of ellipsoidal microcavities operating in 700 torr of Ne are shown in Figures 4.2(a) and 4.3(a). The ellipsoids in these arrays are oriented such that their major axes are normal to the surface of the glass sheets. Recorded by an optical microscope in tandem with a CCD camera, the photographs illustrate the presence of intense emission at the center of those ellipsoids in which

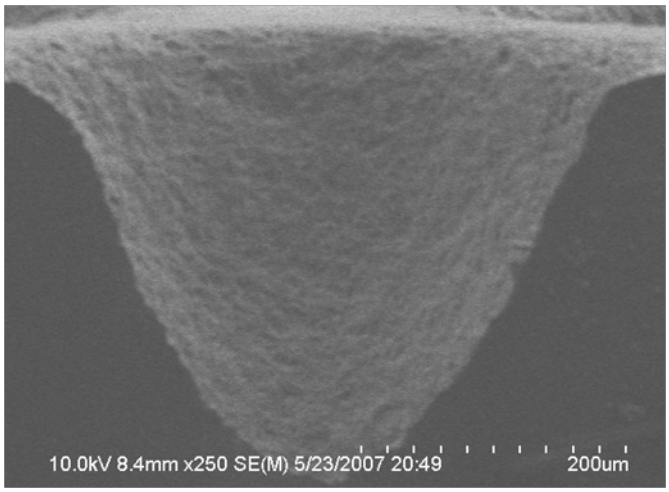

Figure 4.1: SEM of the cross-sectional view of a half-ellipsoidal microcavity.

plasmas have been ignited. However, the voltage region in which all of the microcavities are not ignited was chosen specifically for study. Panel (b) of Figures 4.2 and 4.3, which are false color images of their corresponding photographs, reveal behavior that is not immediately evident in the photographs themselves. Considering Figure 4.2(b), for example, it is apparent that one or more luminous spots appear near the wall of those microcavities in which, at this voltage (V_1, estimated plasma power loading of 56 W-cm^{-3}), a microplasma has not yet been ignited. Each of these spots is correlated with a nearest neighbor microcavity in which a microplasma has been established. For example, the nonignited cavity that is indicated in Figure 4.2(a) by the white circle has three nearest neighbors with fully operating microplasmas and, accordingly, three faint luminous spots are evident near the perimeter of the central unignited cavity. Digital analysis of the image of Figure 4.2(b) (correcting for saturation and the limited depth of field of the microscope) demonstrates that such spots are the result of the scattering of incoherent radiation from one microplasma into neighboring microcavities. Image subtraction, in particular, reveals that cavities at a distance of five to six times the intercavity spacing (pitch) receive detectable scatter from a single microplasma.

However, the observed scattering may also be responsible for a form of intercavity coupling that is more interesting. Consider, for example, Figure 4.3. If the voltage imposed on the array of Figure 4.2 is increased from V_1 to a slightly higher value V_2, then the photograph of Figure 4.3(a) is recorded.

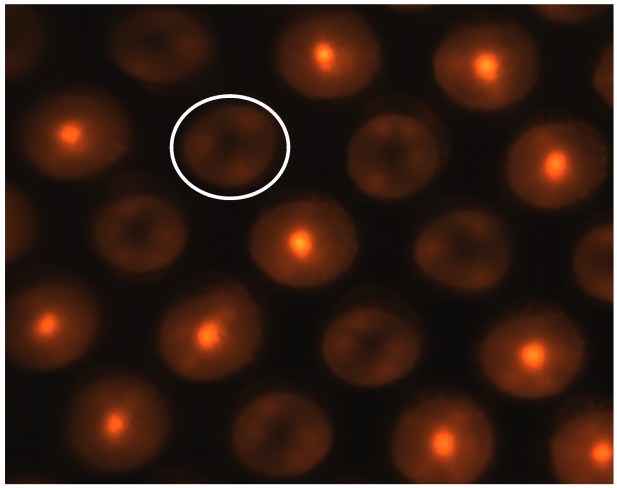

(a)

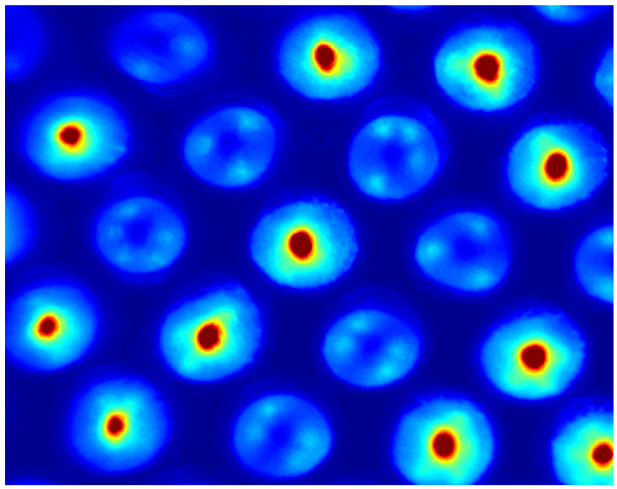

(b)

Figure 4.2: (a) Photograph and (b) corresponding false color image of the emission intensity produced by an ensemble of ellipsoidal microcavities operating in 700 torr of Ne at a voltage V_1.

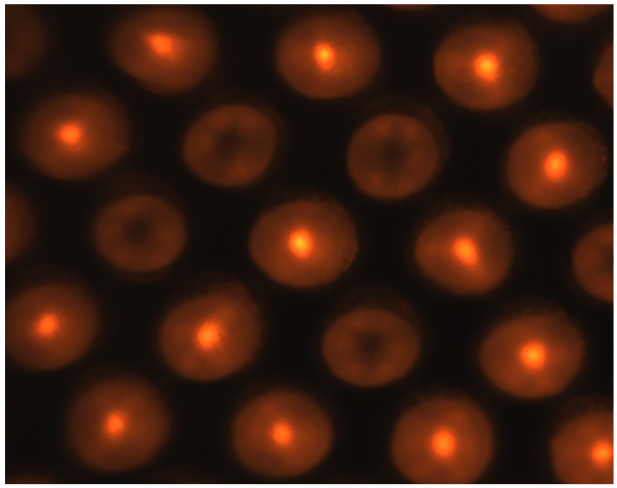

(a)

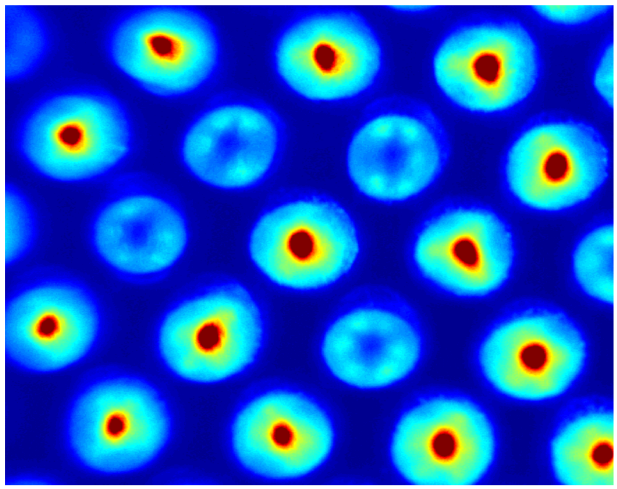

(b)

Figure 4.3: Images recorded under identical conditions to those of Figure 4.2 except that the operating voltage $V_2 > V_1$.

Panel (b) of Figure 4.3, the false color counterpart of Figure 4.3(a), shows that the number of microcavities remaining unignited has fallen by 1/3 and the center of each of these is, from an emission perspective, dark. More importantly, the spatially resolved emission profiles in those cavities that have ignited are apparently distorted. After correcting Figures 4.2(b) and 4.3(b) for the aforementioned CCD camera/microscope effects and the influence of scattered fluorescence from surrounding microcavities, the distortion is significantly reduced, but the images suggest nevertheless that each microplasma is perturbed by the presence of another microplasma in a neighboring microcavity. The perturbation manifests as an elongation of both microplasma intensity profiles along the axis connecting the two cavities. This has been checked out in this work depending on the experimental conditions. One possible mechanism for the former is a variant of the optogalvanic effect in which atomic emission generated by one microplasma is partially absorbed by its neighbor. Although representative of preliminary experiments, the images presented here vividly illustrate a few of the intriguing phenomena that are observable in microplasma arrays, and this has stimulated ongoing research to elucidate the collective phenomena in arrays of microplasmas and their possible mechanisms.

The spatial broadening and intensification of the visible emission from microchannel plasmas, relative to a spatially-isolated channel, has also been observed in the analysis of emission profiles. The structure of Figure 3.4(c) was used to investigate this phenomenon. Figure 4.4 shows the pressure dependent broadenings of visible emission profiles in linear microplasmas. These measurements were made with a CCD camera and telescope, and the data of Figure 4.4 were obtained with a resolution of 2.3$\pm$0.3 μm from lineouts. Two channel widths (W) of 100 μm and 200 μm were tested and their pitch (Λ) was 200 μm and 400 μm, respectively. Regardless of the channel width, the full width at half max (FWHM) of the spatial emission profiles increased as the pressure increased from 200 to 700 Torr in Ne, and the increase is more pronounced with 200 μm wide channels. It is interesting that the ratio of the FWHM of 700 Torr to the one of 200 Torr is $\sim$1.5 for both of the channels. The broadening of the spatial emission for arrays of microchannel plasmas, shown in Figure 4.4, is in disagreement with theoretical predictions [5] and experimental observation [47] for a *single* microcavity plasma. This discrepancy between arrays and single microplasmas led to

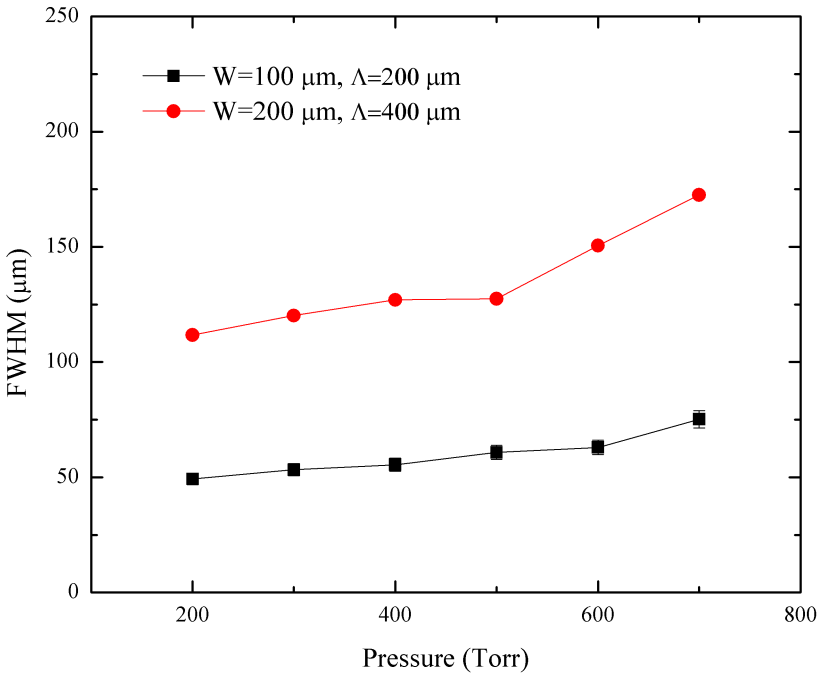

Figure 4.4: Pressure dependent FWHM of visible emission profiles.

continuing investigations into the phenomena.

Further experiments conducted with microchannel plasma arrays hav-

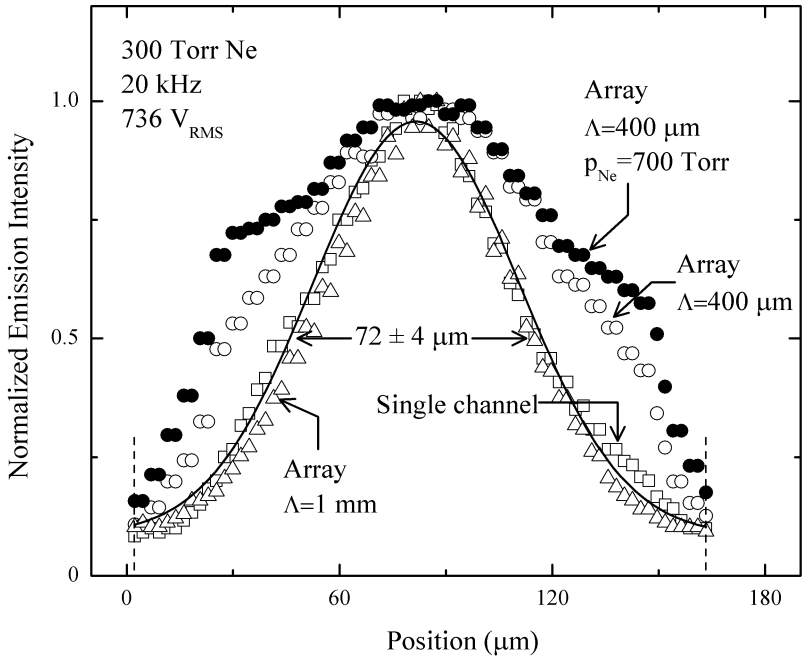

Figure 4.5: Comparison of the transverse emission intensity profile (lineout) for a single 160 μm wide microchannel plasma (□) with those for a microchannel of the same dimensions that is a member of a three element array having a pitch (Λ) of 400 μm (○) or 1 mm (△). The uncertainty in amplitude for each data point is smaller than the size of the associated symbol and the spatial resolution is ≈5 μm. The continuous curve drawn through the Λ=1 mm and single channel data is a Gaussian with a full-width of 72 μm, and the positions of the microcavity sidewalls are indicated by dashed vertical lines. Data for a Λ=400 μm array operating at 700 Torr Ne are also given(●).

ing as many as 10 parallel elements (channels) show clear evidence of optical coupling between the microplasmas. Consider Figure 4.5, for example, which compares the transverse, spatially-resolved emission profiles recorded for a single, isolated microchannel plasma with those emitted by each channel of a three-element array having a pitch of 400 μm or 1 mm. For all of the microplasmas represented in Figure 4.5, W=160 μm and V_{RMS}=736 V, and most of the data (open points) was acquired for p_{Ne}=300 Torr. Note that

the single microplasma emission profile (□), which illustrates the optical behavior expected of each linear plasma element in the absence of interactions between the microchannels in an array, is virtually indistinguishable from that for the Λ=1 mm array element (△). Both curves are described well by a Gaussian with a full-width of 72 μm. When the microchannel pitch in the array is 400 μm, however, the emission profile (○) differs significantly from that for a single channel and the deviations are most pronounced off-axis, near the side walls of the cavity. Not only is the breadth of the Λ=400 μm profile $>$ 60 % larger than that for a single channel but a distinct transition between the sheath and negative glow regions appears 20–30 μm from the side walls. For convenience, the Λ=400 μm data for p_{Ne}=700 Torr is also shown in Figure 4.5 to illustrate the steepening of the emission curve that occurs near the walls with increasing pressure. Attributing these phenomena to light scattering within the array is not viable for several reasons, one of which is the pressure and Λ-dependent alteration of the profile. Rather, I associate the reproducible behavior of Figure 4.5 (and similar data acquired with other arrays) to the resonant absorption of visible Ne atomic emission which, owing to the optogalvanic effect [48], culminates in enhanced plasma fluorescence and near the sheath/negative glow interface, in particular. The optical transmission of the array's glass substrate restricts the Ne emission scattered into adjacent channels to the characteristic lines in the ∼550–750 nm wavelength region, the strongest of which are observed to be the $3p'[1/2]_0$–$3s'[1/2]^o_1$ and $3p[1/2]_1$–$3s[3/2]^o_2$ transitions at 585.2 nm and 703.2 nm, respectively. The absorption of incoming radiation by a microplasma increases E/N locally (where E and N are the electric field strength and gas number density, respectively) because of the altered 3p and 3p′ excited state distributions which, in turn, heat the electrons and enhance spontaneous emission because of the superlinear dependence of electron temperature T_e on E/N [16]. Relative to a single channel, the increase in fluorescence of a microplasma in a Λ=400 μm array reaches maximum ∼30 μm from the wall, a distance consistent with an absorption length given by a Ne (3p←3s) absorption cross-section of (2–3) $\cdot 10^{-12}$ cm^2 [49] and a lower level (3s) population of 10^{14} cm^{-3}. Because the spontaneous emission power received by a microplasma from its neighbors scales with array pitch as Λ^{-2}, the negative glow/sheath transition is not evident for the 1 mm pitch array as is the case for Λ=400 μm. Although the optogalvanic effect has been known for decades [50], it has neither been

demonstrated previously on the dimensional scale of interest here nor been adopted for coupling discharges. The interchange of atomic radiation by two or more microscopic plasmas in close proximity to one another is a potentially versatile mechanism for controlling the properties of both or phaselocking the optical emission from an array of parallel channels.

Finally, capacitive effects have been eliminated as an alternative explanation for the data of Figure 4.5. Varying the driving voltage frequency from 5 kHz to 60 kHz alters the capacitive coupling impedance $Z_C \propto(\omega C)^{-1}$ by more than an order of magnitude, yet both the arrays with a pitch (Λ) of 1 mm and 400 μm provide almost identical profiles of the intensity, as shown in Figure 4.6(a). The emission profile of 5 kHz and 60 kHz for both the 400 μm and 1 mm pitches shows a minor change only near the negative glow region and the broadening of emission profiles was not observed over a frequncy range of 5–60 kHz. Thus, by differing the pitch and frequency, it was demonstrated that each element of an array of linear microchannel plasmas is optically coupled to its neighbors and this is attributed to the optogalvanic effect.

4.2 Electrical Coupling in Arrays of Microplasmas

The electrical probing of arrays of microplasma devices reported here shows that there is a transition from a Townsend-like to an abnormal glow-like discharge in these devices. This study will also show that each microcavity plasma is electrically coupled to its neighbors, possibly by a charge imbalance on the dielectric. Arrays of microplasma devices having the structure shown in Figure 3.4(b) were tested for this investigation.

The tested structure, by intentionally adding a micron-scale gap ($\sim$80 μm) to microcavity plasma devices of Figure 3.4(a), has analytical advantages in that the ratio of discharge current to displacement current is higher than conventional microcavity plasma devices (Figure 3.4(a)) without a gap. The simple structure of dielectric layers thus lends itself to being electrically modeled as compared to other alumina or silicon microcavity plasma devices [46]. The specific dimensions of the devices tested were illustrated in Figure 4.7. The ellipsoids in Figure 4.7(a) have a major axis of 800 μm and minor axis of 600 μm. The depths of half-ellipsoidal cavities are 450 μm and 250 μm

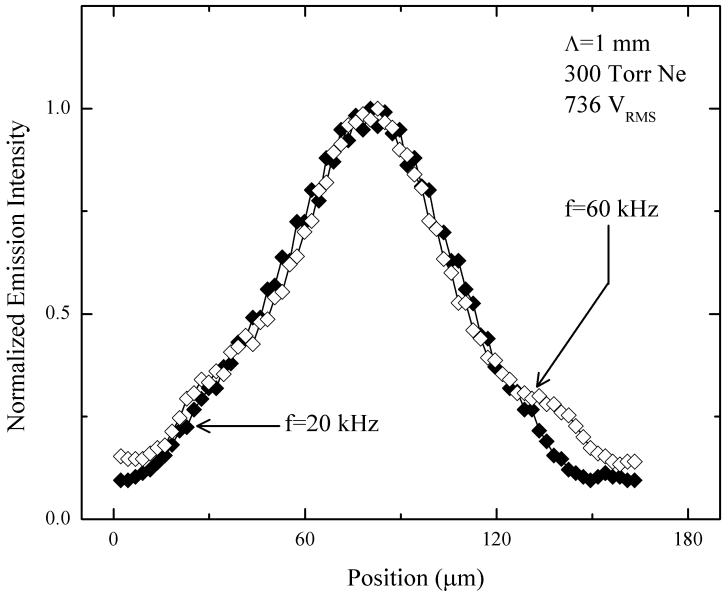

(a)

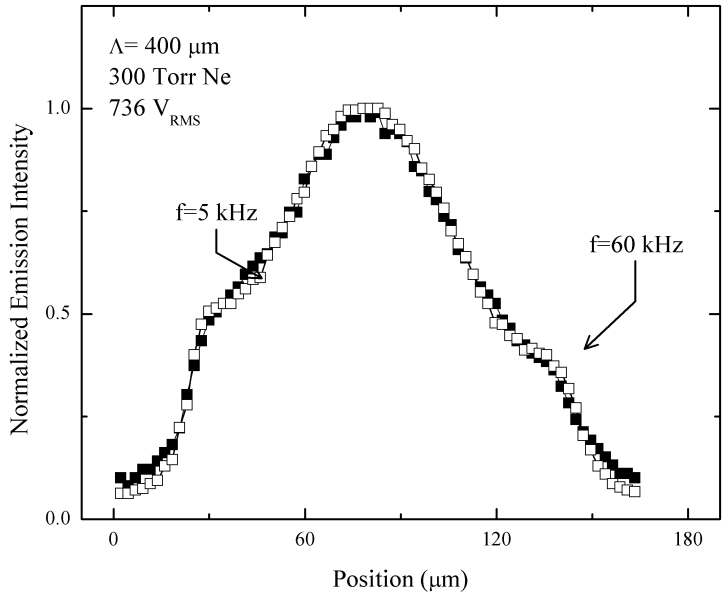

(b)

Figure 4.6: Comparison of the transverse emission intensity profile (lineout) for a single microchannel in an array for different values of pitch: (a) Λ=1 mm, and (b) 400 μm.

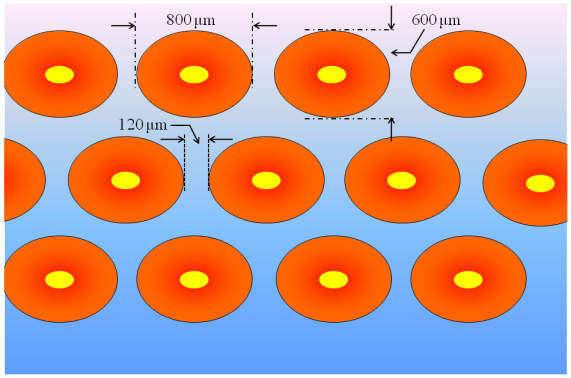

(a)

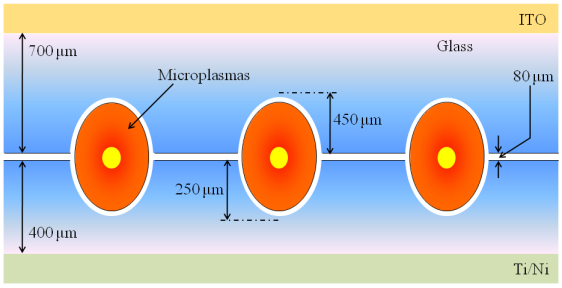

(b)

Figure 4.7: Structure of ellipsoidal microcavity devices with an 80 μm gap: (a) top view of an array of microcavities; and (b) a cross-sectional diagram of the device. The depth of a half-ellipsoidal microcavity on the top glass substrate is 450 μm and the depth of the half-ellipsodial microcavity on the bottom substrate is 250 μm.

for the glass substrate with indium tin oxide (ITO) and the glass substrate with Ti/Ni, respectively. To preserve the micron-scale distance between the bottom of the cavities on a micron scale, the gap distance was set to 80 μm and the distance between the bottom of the cavities including the gap distance was 880 μm in the tested devices.

Voltage-current (V-I) characteristics of this ellipsoidal microcavity plasma device with an 80 μm gap are given in Figure 4.8. The V-I curve is a standard indicator of the electrical properties of plasmas and plasma devices. The positive slope is a well known signature of the abnormal glow discharge and is beneficial for applications because it eliminates the need for resistive ballast. Unexpectedly, three slopes were present in the curves for pressures of 300–700 Torr. For example, Ne at 300 Torr showed different slopes in the

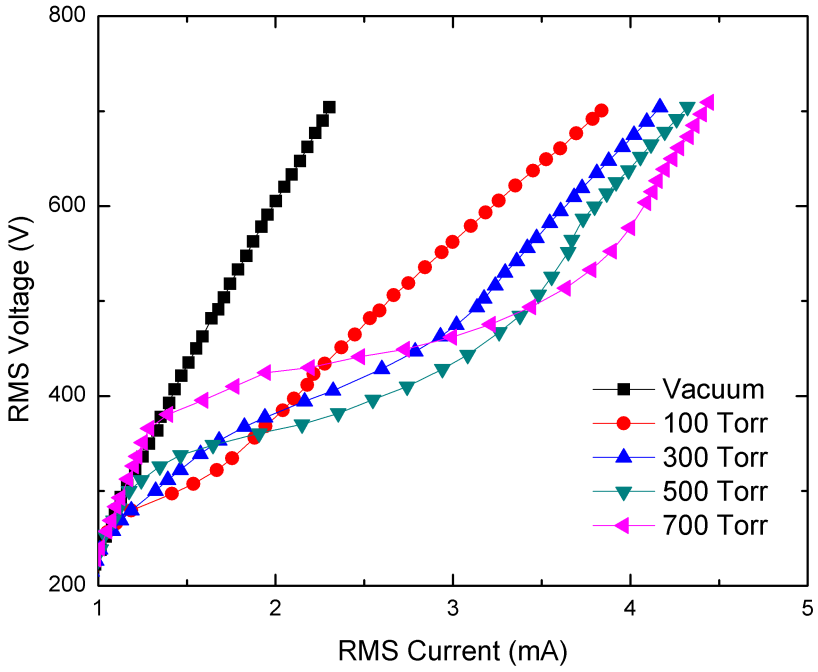

Figure 4.8: V-I characteristics for an arrays of glass microcavity plasma devices with an 80 μm gap. The arrays comprises of 350 devices.

220–300, 300–420 and 420–710 V_{RMS} regions. Spatially-coupled temporal oscillation has unexpectedly been observed in the region of 300–430 V_{RMS}. An electrical model [51] for the device shown in Figure 4.7 was adopted to further investigate this phenomenon.

The electrical model analysis for the devices of Figure 4.7(b) is presented in Figure 4.9. The applied voltage to the top electrode of ITO is represented by $V_{APPLIED}$, C_{SD} is a total capacitance of the glass dielectric layers, I_{TOTAL} is a total current drawn by the array, the Z_{GAS} represents the variable impedance of the plasmas and V_{GAS} is the voltage applied between the top half-ellipsoidal microcavity and its corresponding half-ellipsoidal cavity, including the 80 μm gap . This model is identical to the corresponding model

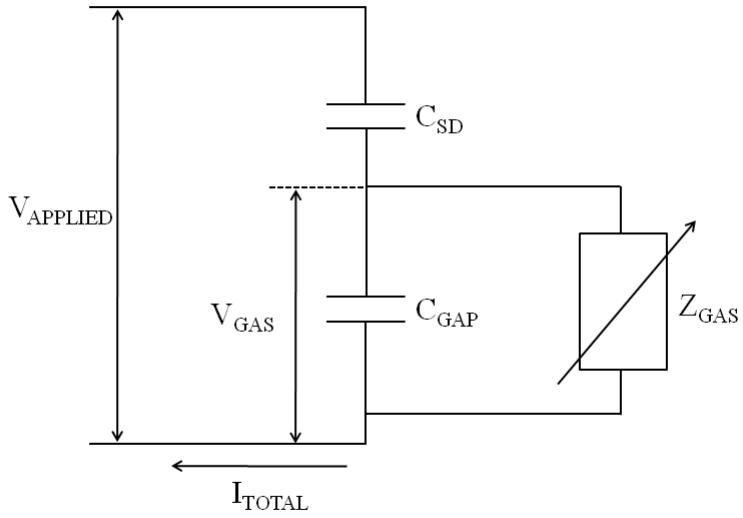

Figure 4.9: An electrically equivalent circuit of glass microcavity plasma devices with a gap.

for conventional dielectric barrier discharge devices [51] with the assumption that the effect of the microcavity on the surface dielectric is negligible. A capacitance measurement of the device showed that this assumption is acceptable. The capacitance C_{SD} is the sum of series capacitances of a top and bottom glass substrate (C_{TOP} and C_{BOTTOM}) with microcavities and is calculated by the expression:

$$C_{SD} = \frac{C_{TOP} \times C_{BOTTOM}}{C_{TOP} + C_{BOTTOM}} = \frac{\epsilon_0 \cdot \epsilon_r \cdot \frac{A}{d_{top}} \times \epsilon_0 \cdot \epsilon_r \cdot \frac{A}{d_{bottom}}}{\epsilon_0 \cdot \epsilon_r \cdot \frac{A}{d_{top}} + \epsilon_0 \cdot \epsilon_r \cdot \frac{A}{d_{bottom}}} \qquad (4.1)$$

where ϵ_0 is the permittivity of free space, ϵ_r is the permittivity of a glass substrate, A is the area of an electrode, d_{top} is the thickness of the top glass substrate and d_{bottom} is the thickness of the bottom substrate.

The capacitance of the gap (C_{GAP}) is also calculated similarly as in Equation 4.1. The equivalent circuit model provides the analytical solution of a gas voltage (V_{GAS}) and is given by

$$V_{GAS} = V_{APPLIED} - \frac{1}{C_{SD}} \cdot \int I_{TOTAL}(\tau) d\tau \ . \tag{4.2}$$

The applied voltage, the gas voltage and discharge current for voltages of 250 and 410 V_{RMS} in 300 Torr of Ne are summarized in Figure 4.10. The 250 V_{RMS} and 410 V_{RMS} curves are representative of the 220–300 V and 420–710 V regions, respectively. These data show clearly the transition from a Townsend-like discharge (Figure 4.10(a)) to an abnormal glow-like discharge (Figure 4.10(b)). The glass microplasmas at 250 V_{RMS} are dimmed glows shown in Figure 4.10(a). Both the discharge current and the gas voltage for 250 V_{RMS} have the similar feature of a sinusoid to the applied voltage. This suggests that the cathode sheath does not exist in the plasmas. In dielectric barrier discharges, the cathode sheath is formed and the gas voltage drops because of charge recombination on the dielectric surface. However, no change was noticed in the gas voltage at 250 V_{RMS}. The depth and shape of the half-ellpsoidal microcavities of the top and bottom substrate also have not been reflected in the maximum of the discharge current when the polarity of the applied voltage changed. This observation leads to a conclusion that the sum of the depth of half-ellipsoidal microcavities determines the maximum discharge current, and this is further evidence that the plasmas are Townsend-like discharges. The maximum current, which was less than 1 mA, of this test is also a well-known aspect of Townsend discharge. These features were dramatically changed when the applied voltage increased to 425 V_{RMS}. The visible emission was distinct from that of 250 V_{RMS}. The abrupt decrease of the gas voltage was clearly observed and this is an indication of the existence of sheath of plasmas. The decrease of the gas voltage also correlates with the FWHM of a discharge current spike of less than 1 μs. The maximum current is 7.9 mA when the bottom electrode is the cathode and the maximum is 7.3 mA when the top is the cathode. The properties of the cathode are different for the different geometry of a microcavity. The

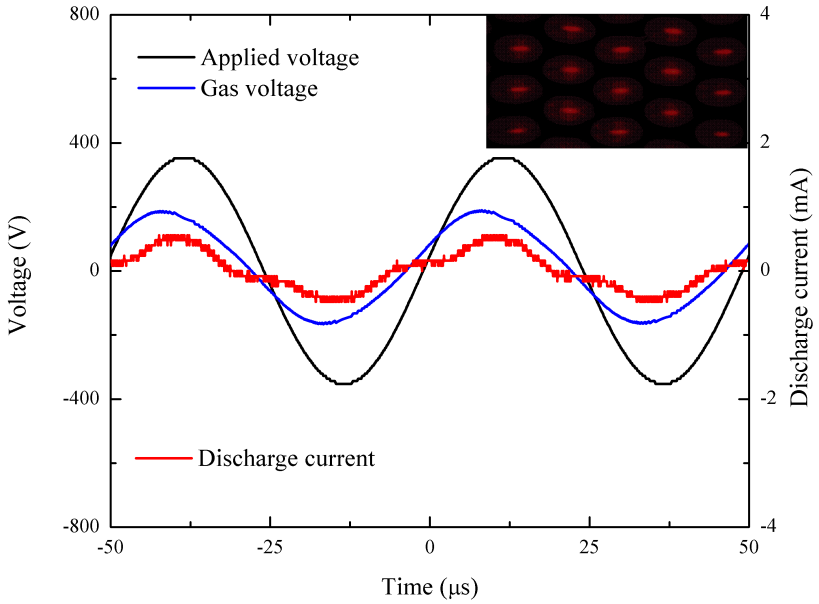

(a)

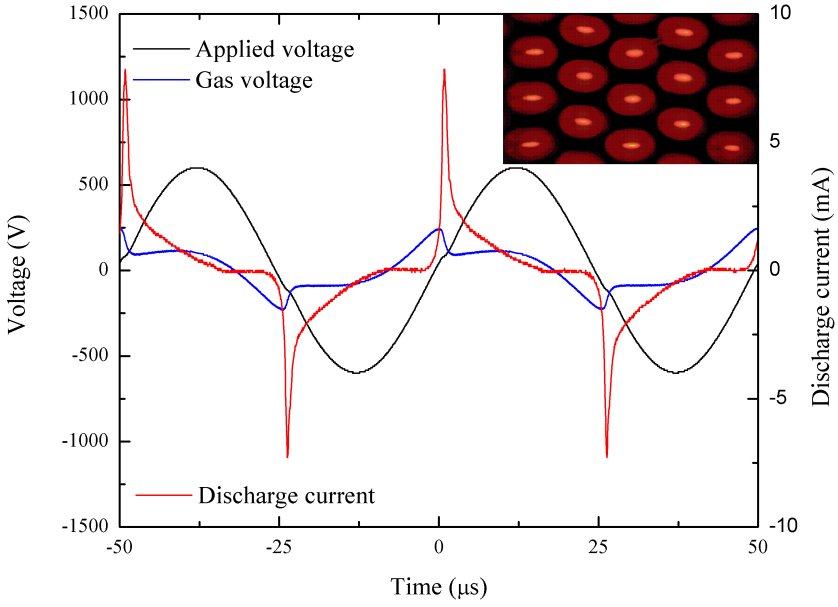

(b)

Figure 4.10: Applied voltage, gas voltage and discharge current for different voltages of: (a) 250 V_{RMS} and (b) 425 V_{RMS}.

maximum current was obtained at the smaller volume of a microcavity as predicted from a numerical simulation [52].

Spatially-coupled temporal oscillations were observed during the transition from the Townsend-like to an abnormal glow discharge. The oscillations, which have two different modes of the visible intensity, were recorded by a CCD in tandem with an objective lens. Figure 4.11 illustrates the bistable modes, which are temporally random, at 310 V_{RMS} in 300 Torr of Ne. Photographs, used for this analysis, were extracted from the recorded video clip. One example is displayed in Figure 4.11(a). The time interval between each frame was ∼80 ms and the exposure time was 50 ms. The microcavities indexed to 1, 2 and 3 are arbitrarily chosen to study the temporal evolution. The horizontal lineouts of the selected microcavities in Figure 4.11(b) show that the visible intensity randomly changes between frames, yet the intensity bifurcates between two differnt modes (High/Low status) of visible emissions from the plasmas. The oscillations in a cell also appear to be closely related to their neighboring microcavities. Figure 4.11(b) illustrates some of the correlation between microcavities. Cell 3 is surrounded by its six neighbors, two of which are cell 1 and 2. It shows that the intensity of at least one of the other neighboring cavities changes to the opposite mode when the center cell of cell 3 changes the mode. The evolution from frame 1 to frame 2 shows that the intensity of cell 3 decreased and the intensity of the neighboring cell 2 increased. One exception is the evolution from frame 5 to 6; however, cell 3 was correlated to other neighboring cavities in this case. Only 11 frames were displayed; however, these oscillations continue under operating conditions of 310 V_{RMS} and 300 Torr of Ne.

The applied voltage, the gas voltage and discharge current were analyzed to further investigate these spatially-coupled temporal oscillations and they are shown in Figure 4.12. The applied voltage was a 20 kHz sinusoid operating at 310 V_{RMS}. Temporal profiles of the estimated gas voltage and measured discharge current appear to be the intermediate stage of the ones of 250 V_{RMS} and 425 V_{RMS}. The gas voltage dropped sharply between 2.4 and 5 μs and continued to drop more slowly afterwards. The first abrupt drop of the gas voltage is similar to that of glow-like discharge and this implies the existence of a sheath in the plasmas. The slow decrease of the gas voltage is similar to that of Townsend-like discharge. The temporal pattern of the discharge current also followed these two steps of the gas voltage. The maximum

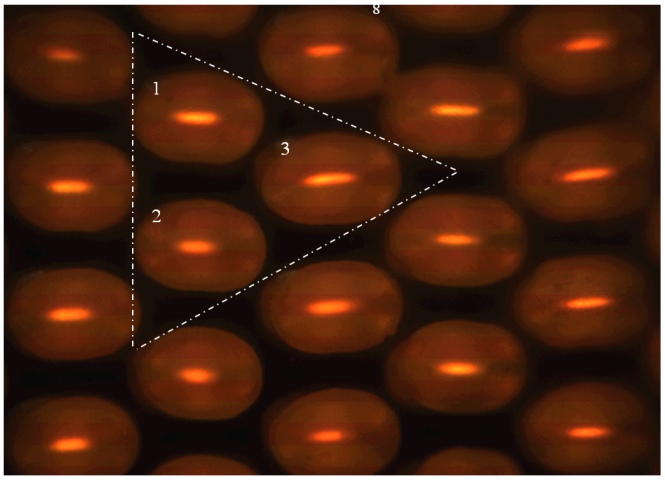

(a)

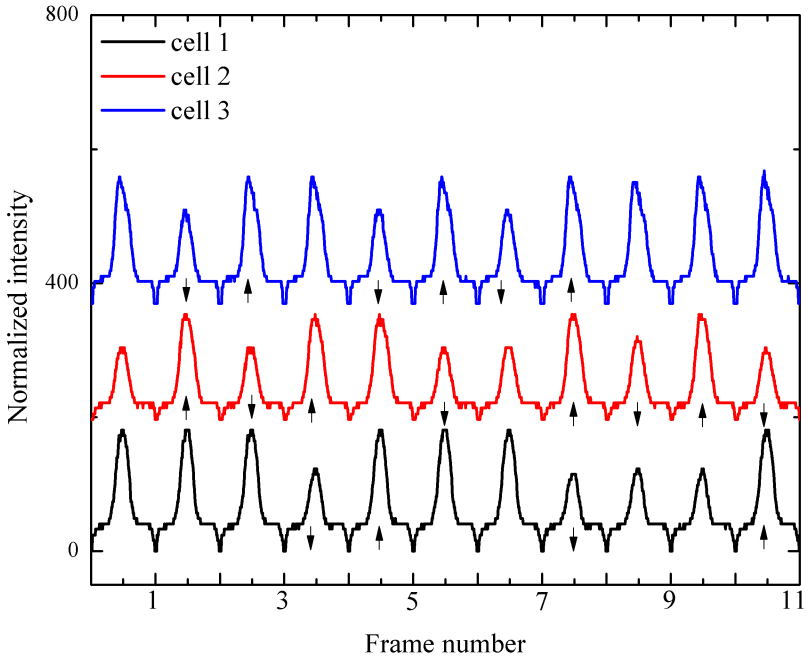

(b)

Figure 4.11: Bistable oscillations at an RMS voltage of 310 V and 300 Torr of Ne: (a) a photograph of the oscillation; and (b) horizontal lineouts of the temporal evolution for the microcavities indexed to 1, 2 and 3. The three microcavities are randomly selected.

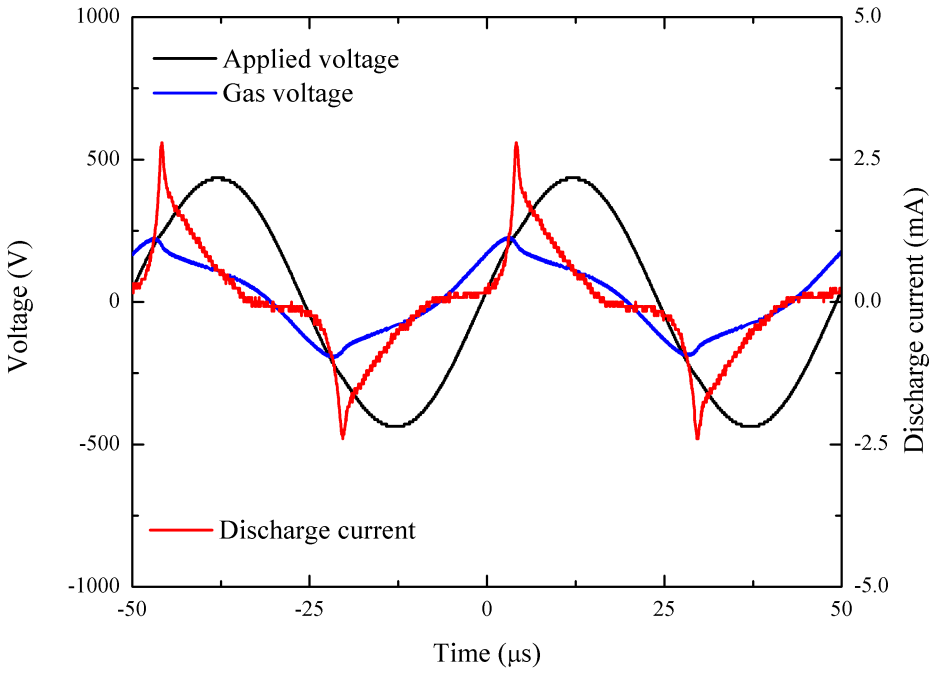

Figure 4.12: Applied voltage, gas voltage and discharge current at the RMS voltage of 310 V and Ne 300 Torr.

current was 2.8 mA and the FWHM of the current was 2.2 μs. The intermediate state indicates the existence of a high impedance for the evolution from a Townsend-like discharge to an abnormal glow-like discharge [53] and this agrees with the positive slope in V-I curves of arrays of microplasmas. The high impedance seems to restrict the maximum of a discharge current and makes recombination processes slower. The negative slope of V-I curves is linked to the spreading of plasmas to the outer cathode surface in a micro-hollow cathode plasma [54]. The cathode of the tested devices was confined in the microcavities, resulting in the positive impedance region between a Townsend-like and an abnormal glow discharge. This high impedance was also associated with the spatio-temporal oscillations in arrays of microplasmas with a micron gap. Each microplasma in the cavities required higher power for the transition from Townsend to glow-like discharge, but the random phenomena such as charge distributions on the dielectric surface with microcavities lead to a local imbalance of a plasma impedance. When one cavity draws more power, its neighboring cavities may lose power. These interactions result in the spatially coupled temporal oscillations in arrays of glass microplasma devices with an 80 μm gap.

4.3 Plasma-Plasma Coupling in Microcavity Plasma Systems

The chaotic behavior [55], self-organization [56] and several patterns such as hexagon [57] or honeycomb [58] of microdischarge in dielectric barrier discharge (DBD) systems have been known and investigated in the last several decades. The plasma systems, however, are limited in that all the microdischarges are randomly generated by the nonuniformity of current distribution on the dielectric layer. The underlying physics of the intriguing phenomena is also not fully understood. To further investigate the phenomena and their fundamental mechanisms in DBDs, the structure shown in Figure 4.13 was investigated. By controlling the depth of two microcavities in the structure, a plasma system comprising of randomly generated microdischarges and spatially-confined microcavity plasmas was implemented and several novel phenomena were observed. The phenomena such as bound microdischarges along the circumference of a circular microcavity, trapped microdischarge be-

tween two microcavities and the interaction of a bound microdischarge with a free microdischarge, are reported here.

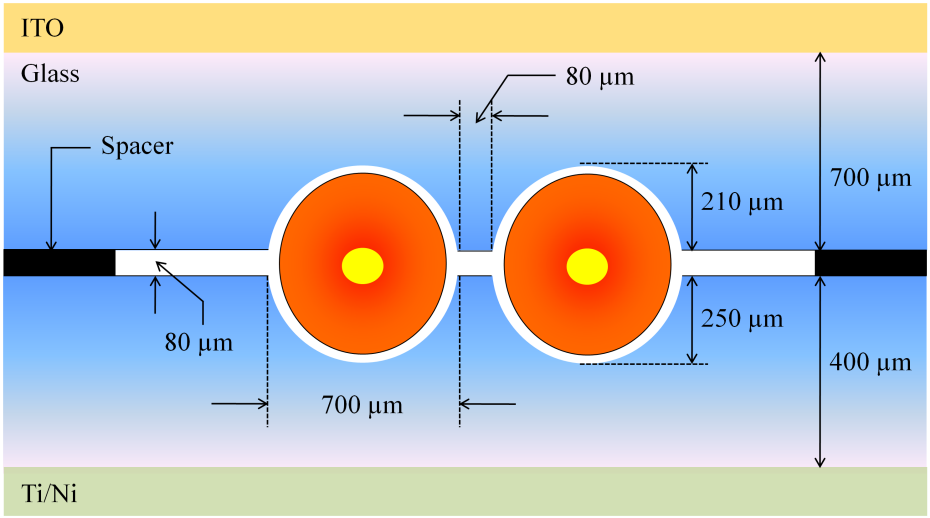

Figure 4.13: Double-cavity microplasma device with an 80 μm gap.

Figure 4.14 illustrates voltage dependent evolution of microplasma generation in the plasma systems having randomly produced microdischarges and spatially-confined microcavity plasma devices. All photographs show microplasmas operating in 760 Torr of Ne. A 20 kHz sinusoid was applied for the operation. Plasmas, as shown in Figure 4.14(a), were ignited and sustained at 467 V_{RMS}. Plasmas were produced in two microcavities and two trapped microdischarges were generated between the two cavities. Dimmed glows were also observed along the circumference of the cavities. Microdischarges in DBDs are produced when a sheath region is fully established near the cathode by sufficient space charge. This condition is made by increasing voltage. Operation at voltages of 496–608 V_{RMS} confirms this mechanism. One microdischarge appeared at 495 V_{RMS} from the dimmed glow along the boundary of the left cavity. Three microdischarges on the perimeter of the left microcavity and two microdischarges on the perimeter of the right microcavity were present at 545 V_{RMS}. At V_{RMS}=608 V, microdischarges

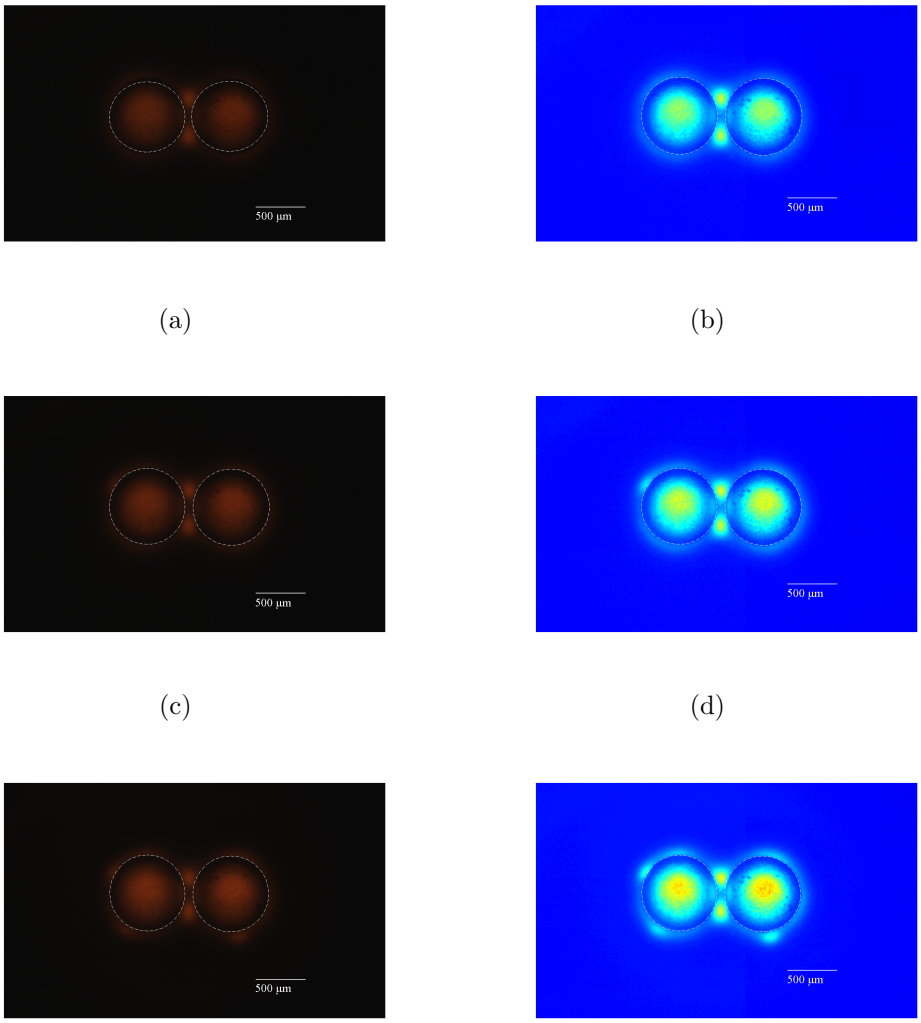

(a) (b)

(c) (d)

(e) (f)

Figure 4.14: Photographs and their corresponding false color images of microplasmas operating in 760 Torr of Ne: (a) and (b): 467 V_{RMS}; (c) and (d): 495 V_{RMS}; (e) and (f): 545 V_{RMS}; (g) and (h): 608 V_{RMS}; (i) and (j): 898 V_{RMS}; (k) and (l): 1061 V_{RMS}; (m) and (n): 1337 V_{RMS}; and (o) and (p): 1768 V_{RMS}.

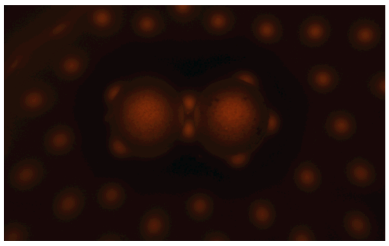

(g)

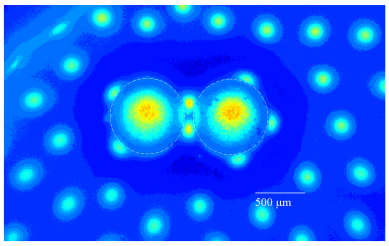

(h)

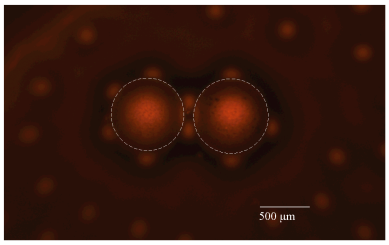

(i)

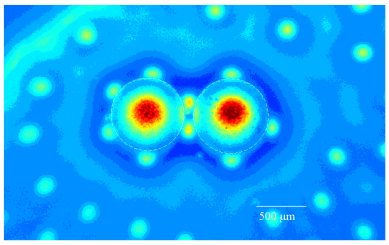

(j)

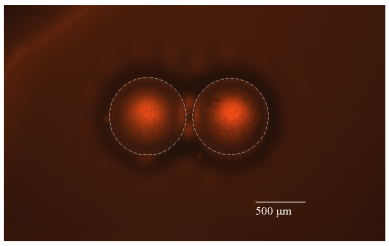

(k)

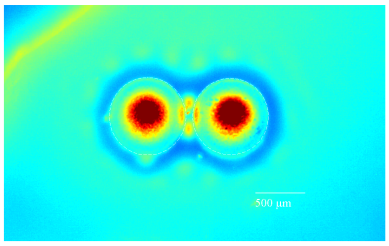

(l)

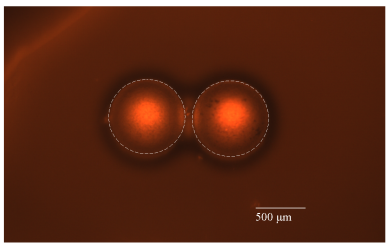

(m)

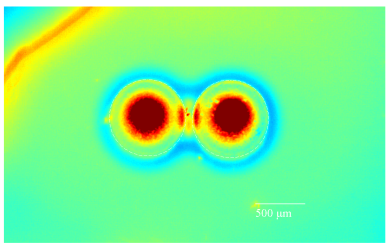

(n)

Figure 4.14: Continued.

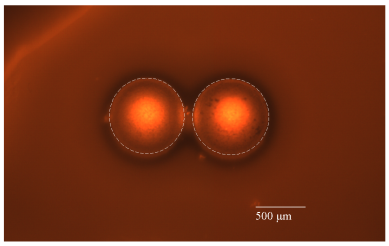

(o)

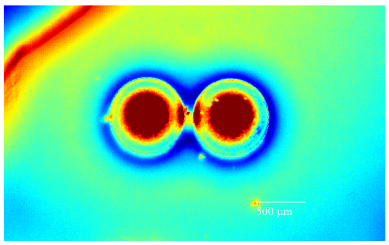

(p)

Figure 4.14: Continued.

were generated over the whole plane and they kept moving to reach a most stable state. These dynamic microdischarges are denoted by "free" microdischarges here. Microdischarges started to change into diffuse glow discharges from 898 V_{RMS} to 1337 V_{RMS}. Eventually, all the microdischarges, other than two trapped microdischarges, altered into diffuse glow discharges. It must be emphasized that the trapped microdischarges between microcavities and the microdischarges along the perimeter of the microcavities has never been observed in other DBD systems.

The behavior between arrays of microdischarges in 760 Torr Ne and 608 V_{RMS} is analyzed by an optical imaging technique. Operation of the tested device in Ne 760 Torr and 608 V_{RMS} was recorded by a CCD. A hundred photographs were again extracted from the video clip and used for this analysis. Statistical data showing the distance between microdischarges and the size of microdischarges are presented in Figure 4.15. The data illustrate that microdischarges having a diameter of 144±11 μm are self-organized with a distance of 485±58 μm. This data also indicate that free microdischarges are balanced even when they keep moving by a possible combination of Coulombic repulsion force, Lorentz attractive force and confinement potential [59] Microdischarges are mainly produced by space charge near the dielectric surface, which results in Coulombic repulsion forces. A localized region of a microdischarge is modeled as a charged region and the Coulombic force between microdischarges is represented by

$$F_{Coulomb} = \frac{1}{4\pi\epsilon_0}\frac{Q^2}{|r_i - r_j|^3}(r_i - r_j) \tag{4.3}$$

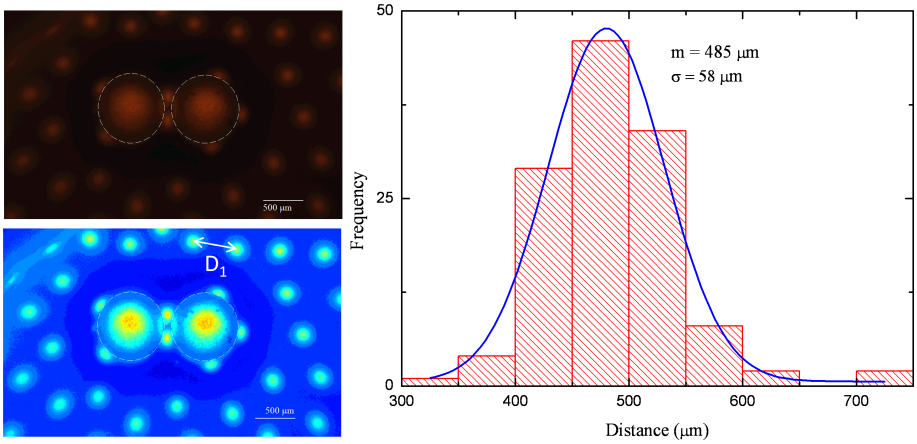

(a)

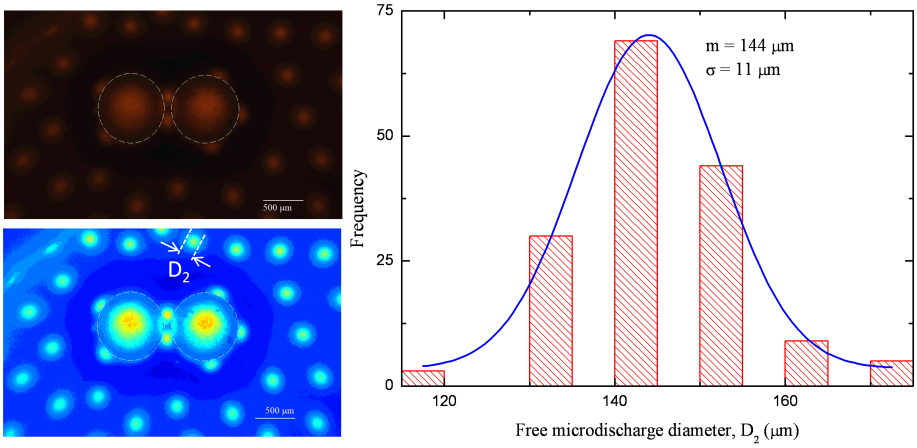

(b)

Figure 4.15: Behavior of microdischarges operating in 760 Torr of Ne and 608 V_{RMS}: (a) distance between microdischarges (b) diameter of microdishcarges.

where r_i and r_j represent the position of microdischarges, Q is the total charge of a microdischarge and ϵ_0 is the permittivity of free space.

There is also Lorentz attractive force between microdischarges which are in phase, given by [59]

$$F_{Lorentz} = -\frac{\mu_0}{2\pi}\frac{I^2}{|r_i - r_j|^2}(r_i - r_j) \tag{4.4}$$

where μ_0 is the permeability of free space.

Previous study [59] has shown a huge discrepancy between the repulsive and attractive forces for microdischarge having the length of several mm. The demonstration of the existence of confinement potential [60] supplemented the balance of forces and the self-organization of microdischarges. The discrepancy between Coulombic and Lorentz force was again confirmed for the characteristic dimension of 80 μm. The statistical data for the distance between microdischarges were used for this calculation. Unfortunately, the current and charge could not be quantitatively measured because of the detection limit. To estimate the repulsive and attractive force, the value of current and charge measured in [59] was scaled according to the dimensions and operating frequency. The predicted value of current and charge was 2.25 μA and 1.12 pC, respectively. These results led to Coulombic force of 48 nN and Lorentz force of 2.1 fN. Thus, in these dimensions, the confinement potential appears to play a critical role in balancing each microdischarge.

One interesting phenomenon is the existence of bound microdischarges which are located on the perimeter of the microcavity. Unlike other microdischarges, which are freely moving to reach a most stable state, the bound microdischarge moves but is bounded to the boundary of the microcavity. This type of microdischarge is probably produced by a geometrical origin of the microcavity, but further study is necessary to elucidate its fundamental mechanisms. This bound microdischarge offers an opportunity to further investigate the interaction between microdischarges because the position is quasi-fixed. Figure 4.16 illustrates the change of the diamter of free microdscharges when they approach bound microdischarges. This clearly shows that the diameter of free microdischarges decreases when the distance between a free and a bound microdischarge is $\lesssim$500 μm. This is caused by the interaction of the free microdischarge with its nearest bound microdischarge. It is probable that space charge, which is responsible for microdischarge gen-

eration, is captivated by a possible comibination of a bound discharge and a microcavity plasma, resulting in the decrease of the diameter of free microdischarges.

The simple plasma system having two microcavities and a microgap showed scientifically interesting phenomena which were not observed in previous plasma systems. It is possible to trap microdischarges between microcavities if the distance is sufficiently close possibly by geometrical origin of the microcavities. Free microdischarges produced in a gap of less than 100 μm have been self-organized. The evidence of the interaction of free microdischarges with bound microdischarges was presented. Continuing research will explain more fundamental aspects of these phenomena, and this plasma system will offer an opportunity to investigate the underlying physics of collective phenomena in a plasma system.

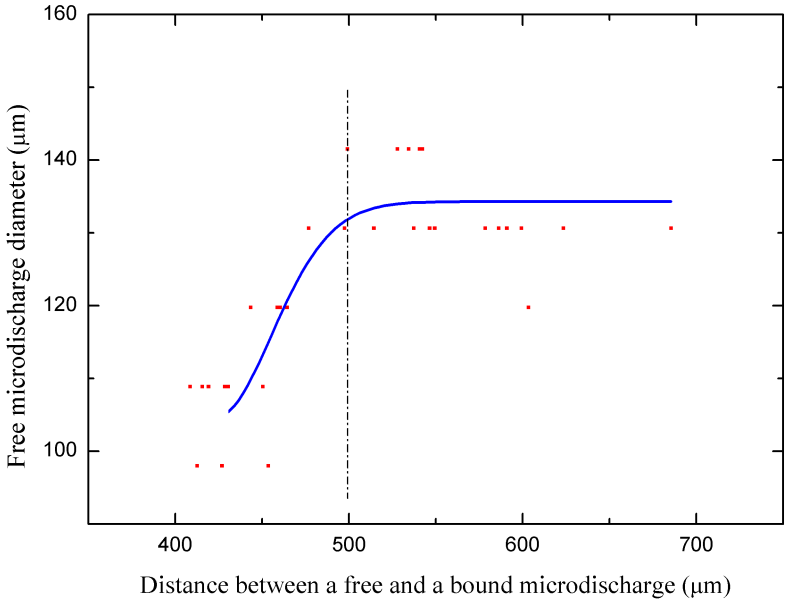

Figure 4.16: Dependence of the diameter of free microdischarges on the distance from a free to a bound microdischarge.

CHAPTER 5

APPLICATION OF MICROCHANNEL PLASMA DEVICES AS ANTENNAS

Plasmas are known to interact with electromagnetic waves of frequencies lower than the plasma frequency. Research has focused on the interaction because of its great potential applications. The reflection of RF signals from the ionosphere has been widely used for long distance RF communication [61] and microwave techniques have been extensively adopted to diagnose plasmas since the 1950s [62]. Research in this area has led to the use of plasmas in electromagnetic devices such as antennas. Plasmas are advantegeous over metal in that plasmas and their arrays can be electrically switched, tuned, and reconfigured in a ≤ 1 μs time interval. Plasma antennas, reflectors, and absorbers have been suggested and demonstrated in the last several decades [63, 64, 65] and theoretical developments have followed [63]. However, the use of plasma devices such as these in military and commercial applications has not yet become feasible for several reasons. Although plasma mirrors have been successfully demonstrated, magnetic fields larger than 100 G were required to sustain them [66]. The mirrors in [64] showed similar reflectance at 10.2 GHz similar to those of conventional metal reflectors. But the band of operating frequencies is still limited by the electron density of the plasma which is on the order of 10^{12} cm^{-3}. Thermal noise and vacuum packaging are also problematic. One possible approach to tackling these issues is to introduce microplasmas instead of macroplasmas for antenna applications. This chapter discusses a proof of concept for microchannel plasma antennas both from experiments and numerical simulations.

5.1 Design and Operation of Arrays of Glass Microchannel Plasmas for Antennas

In glass microchannel plasma antennas, the metal is replaced with arrays of microchannel plasmas. This approach decreases the radar cross section of the antennas. The majority of the plasma antennas is dielectrics made of glass and gas when plasmas are not ignited and they are transparent to radar.

Cross-sectional diagrams of the prototype designs of microplasma antennas are illustrated in Figure 5.1 and Figure 5.2. The configurations have similarities with microstrip patch antennas, where microchannel plasmas correspond to the metal patch of microstrip antennas. The microchannel plasma antennas, unlike conventional plasma columns or slabs in glass tubes [63, 64], incorporate micron-scale plasma columns into glass substrates. The glass micromachining technique [67] developed at the Laboratory for Optical Physics and Engineering Lab (LOPE) made it possible to fabricate arrays of microchannels in glass, and the first planar microplasma antennas have been successfully demonstrated. The device shown in Figure 5.1 was suggested at the early stage of this work. The channel width was set to 200 μm and channel lengths up to 4 cm were tested. The red lines and green lines in this Figure are power feeding lines and ground lines, respectively. Figure 5.1(a) and 5.1(b) show the flexibility in the operating scheme of these devices and stable operations at pressures of 100–500 Torr of noble gases. No visible difference, however, was observed in the plasma operation. Despite the stable operation in this structure, the sputtering of inserted metal wires changed the operating parameters such as the sustain voltage. The design of Figure 5.2 was eventually adopted as a prototype for ongoing research. This prototype is based on the asymmetric half-ellipsoidal microchannel structures introduced in Figure 3.4(c), yet the electrodes were modified to minimize the radar cross section of this antenna, as illustrated in Figure 5.3(g). This prototype has 8 multiple channels having a width and depth of 200 μm. The notation of red and green lines in Figure 5.2 is same as Figure 5.1 and two different operating strategies are described in Figure 5.2(a) and 5.2(b).

The fabrication and packaging procedures of the prototype of Figure 5.2 are described in Figure 5.3. A sodalime glass substrate was cleaned through a standard degreasing process of acetone/isopropyl alcohol, dipped in 49 % hydrofluoric acid (HF) for 2–3 sec, washed in deionized (DI) water for a

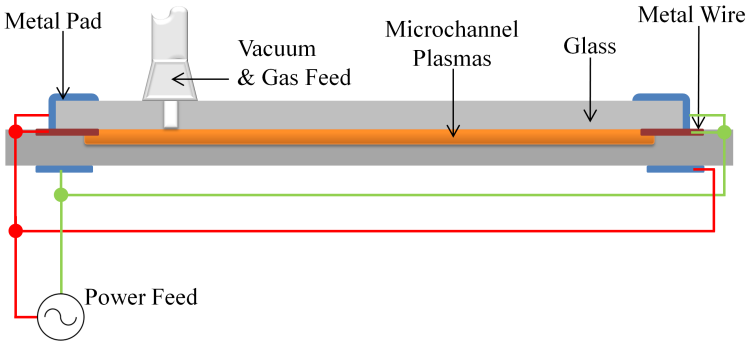

(a)

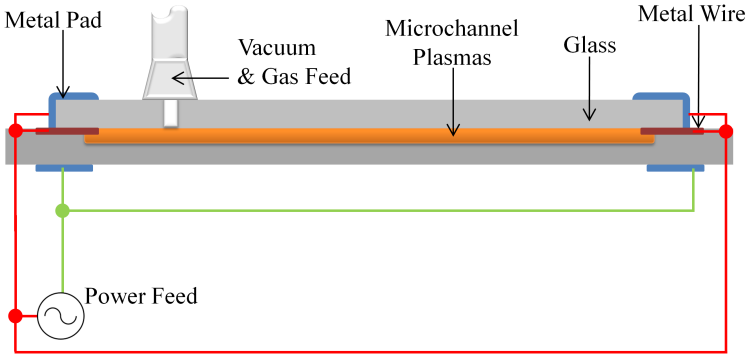

(b)

Figure 5.1: Cross-sectional diagrams of the prototype of microchannel plasma antennas with inserted metal wires: (a) a top metal pad and an inserted wire on the left and a bottom metal pad on the right are powered by a 20 kHz sinusoid. Other wire and metal pads are grounded; and (b) top metal pads and inserted wires at both sides are powered by a 20 kHz sinusoid. The other two metal pads at the bottom of the prototype are grounded.

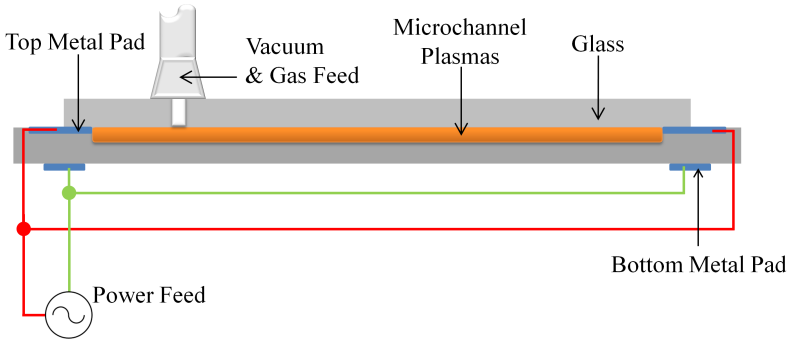

(a)

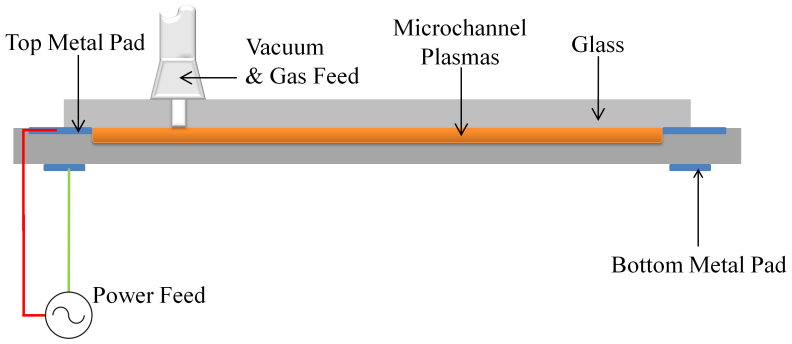

(b)

Figure 5.2: Cross-sectional diagrams of the prototype of microchannel plasma antennas: (a) two top metal pads are powered by a 20 kHz sinusoid and two bottom metal pads are grounded; and (b) a top metal pad on the left is powered by a 20 kHz sinusoid and two bottom metal pads are grounded. Another top metal pad on the right is a floating electrode.

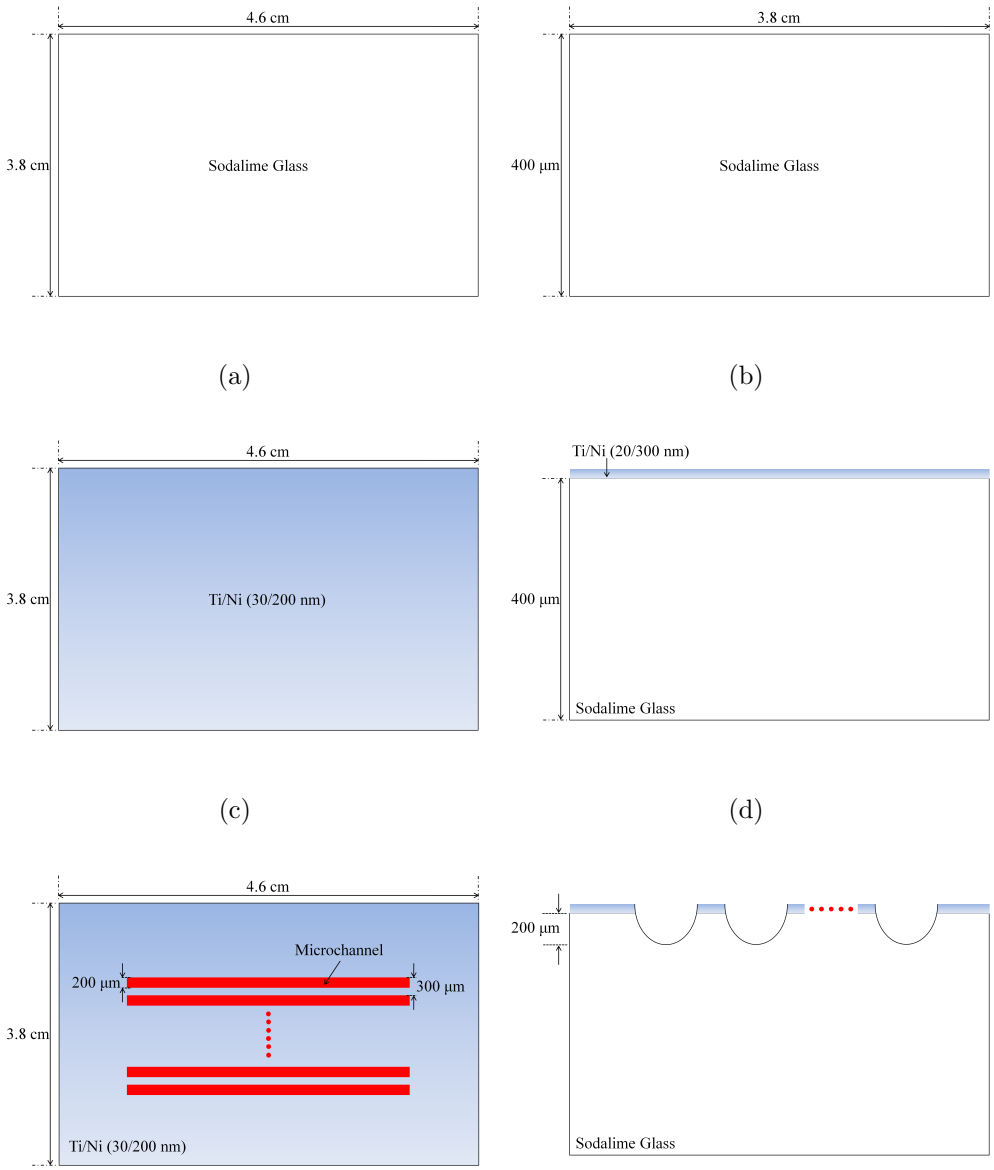

Figure 5.3: (a)-(j): Process sequence for fabricating the prototype of microchannel plasma antennas. The diagrams in the left column are top view and those in the right column are cross-sectional view.

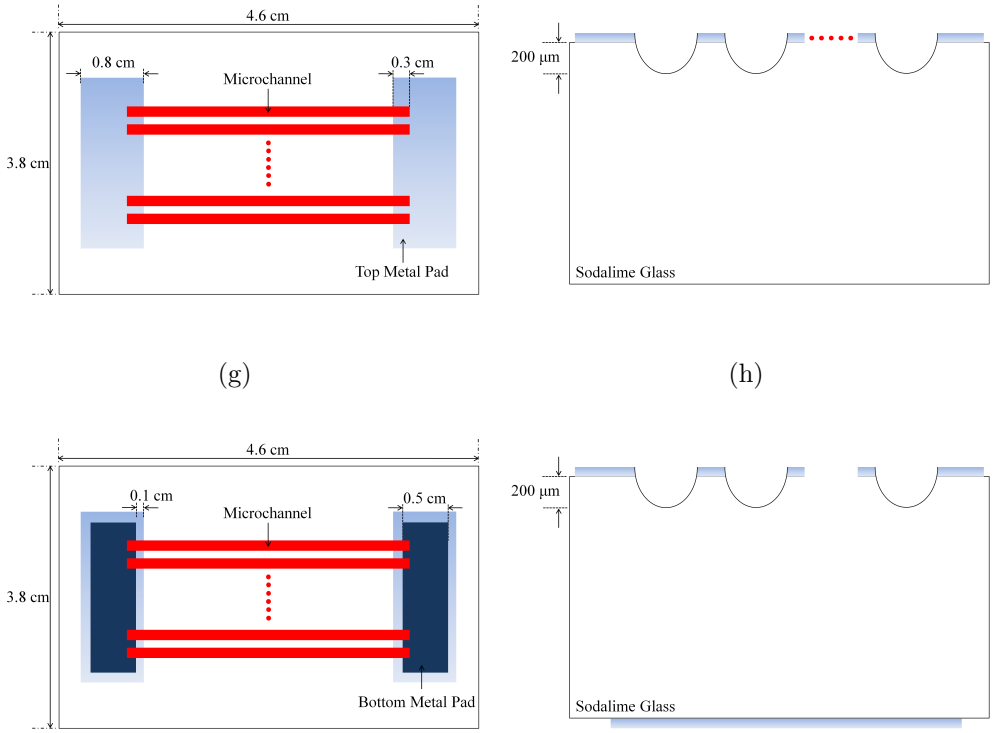

Figure 5.3: Continued.

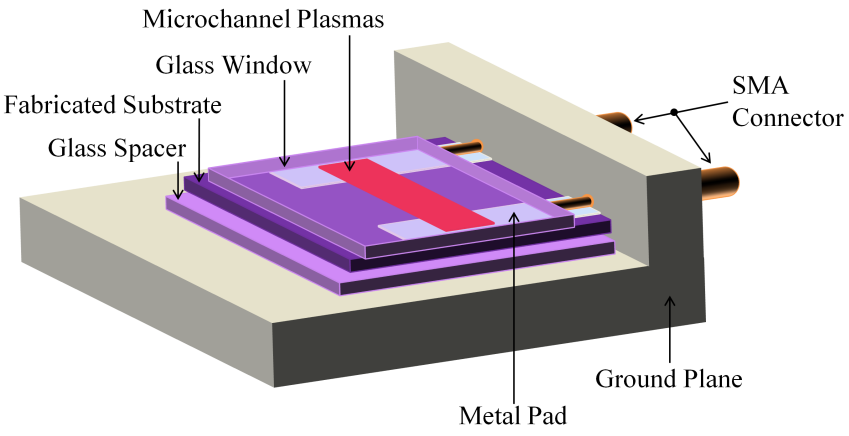

Figure 5.4: A prototype of microchannel plasma antennas integrated onto a ground plane.

minute and dried by N_2 blower. The substrate was baked at 125 °C to elimiate the moisture on the surface. The top electrode of Ti/Ni (30/200 nm) was evaporated onto the glass substrate right after the baking process. Multiple microchannels with a width of 200 μm and pitch of 300 μm are are fabricated by soft-lithography and micropowder blasting described in Chaper 3. The metal pad is patterned by photolithographic processes and only 5–20 % of the channel in length is covered by the electrode. The evaporation of bottom metal pads followed. The metal pads were aligned according to the top metal pads but the bottom ones had a smaller area. The evacuation port was used to remove impurities and introduce gas/gas mixtures into the device. The fabricated glass substrate was hermetically sealed with a 2.3 mm thick glass window and they were fixed onto a 3.4 mm thick glass spacer. The package is integrated with an aluminum ground fixture. The final structure is shown in Figure 5.4.

Two photographs of the operation of the device shown in Figure 5.1 are presented in Figure 5.5. A half-ellipsoidal 200 μm wide channel with a length of 4 cm was fabricated and tested. The applied voltages for the operation in

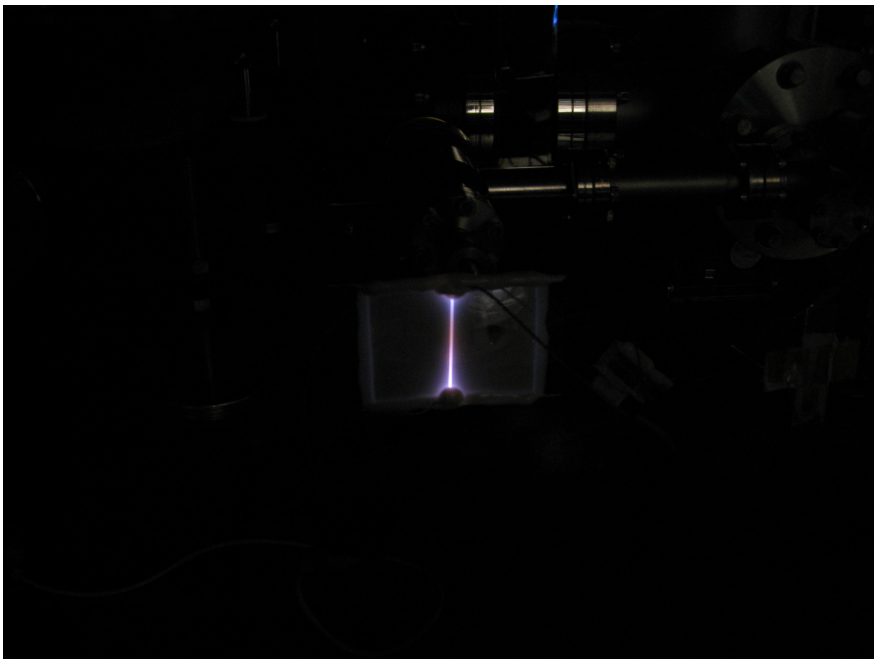

(a)

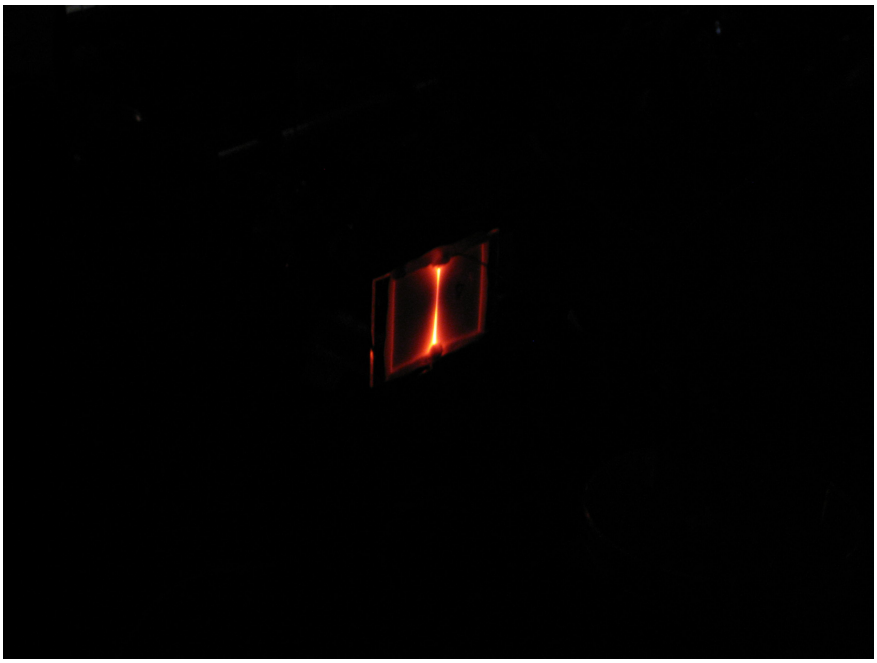

(b)

Figure 5.5: Photographs of the prototype micorchannel plasma antenna shown in Figure 5.1, illustrating the operations in: (a) He 300 Torr; and (b) Ne 500 Torr. A 20 kHz sinusoid was applied to these devices for the operations.

He 300 Torr and Ne 500 Torr were about 1350 and 1600 V_{RMS}, respectively and the operations were stable for both He 300 Torr and Ne 500 Torr: and other noble gases. It is noted that the visible emission was stronger near the electrode than the center of the microchannel and the fluorescence resembles Bow-Tie antennas [68].

5.2 Simulations of Electron Density

The most fundamental question about microchannel plasma antennas is whether metal can be replaced by microchannel plasmas. The question is mainly about the conductivity and plasma frequency of microchannel plasmas with the operating pressure of 100's Torr. The conductivity of plasmas is proportional to an electron density of plasmas and inversely proportional to collisional frequency. The plasma frequency is also proportional to a square root of electron density. Thus, it is of particular importance to predict the electron density of microchannel plasmas at a given pressure and a finite-element simulation was performed using a COMSOL Multiphysics simulator to accomplish this goal.

An asymmetric half-ellipsoidal microchannel of Figure 3.4(c) with a width of 200 μm and depth of 200 μm is adopted for this simulation. A 400 μm thick sodalime glass has been used for this model and its relative dielectric constant is 7.8. Both electrodes on the top and bottom are modeled as a 1 μm thick perfect conductor (PEC). The fluid model is also employed to investigate the microchannel plasmas in this configuration. This model consists of continuity equations for electron, ion and charged particles/excited species, momentum transport equations for electrons and ions and Poisson's equation. The equations are coupled with boundary conditions. The spatial and temporal variations of the density for each species are obtained by following continuity equations:

$$\frac{\partial n_e}{\partial t} + \nabla \cdot \mathbf{\Gamma}_e = S_e \tag{5.1}$$

$$\frac{\partial n_i}{\partial t} + \nabla \cdot \mathbf{\Gamma}_i = S_i \tag{5.2}$$

$$\frac{\partial M}{\partial t} = D_M \nabla^2 M + D_M \tag{5.3}$$

where $\mathbf{\Gamma}$ is particle flux, S is a source term, n represents charged particle density, M stands for excited species density, D is a diffusion coefficient and the subscripts e and i indicate an electron and ion, respectively

The flux is given by momentum transport equations and they are typically approximated by drift-diffusion approximation. The flux of electrons and ions are

$$\mathbf{\Gamma}_e = -n_e \mu_e \mathbf{E} - D_e \nabla n_e \tag{5.4}$$

$$\mathbf{\Gamma}_i = n_i \mu_i \mathbf{E} - D_i \nabla n_i \tag{5.5}$$

where μ is mobility and $\mathbf{E}$ denotes an electric field.

The electric field within each cell, defined by meshing, is self-consistently calculated by Poisson's equation and it is given by

$$\nabla \cdot (\epsilon \mathbf{E}) = q(n_i - n_e) \tag{5.6}$$

where ϵ is permittivity.

In several plasma display panel (PDP) simulations [69, 70], local field approximation (LFA), rates and transport coefficients are a function of a reduced electric field of $\mathbf{E}$/N, where N is a gas density. This approximation can be valid for ions; however, it is a poor assumption for electrons in that LFA cannot describe the energy transfer in electron-neutral collisions and the spatial variation of the field is huge. LFA also does not consider the electron energy redistribution caused by thermal conduction or convection. Thus, in this model, LFA is applied for ions, yet not for electrons. The reaction rates and transport coefficients of electrons are estimated by the following energy balance equation:

$$\frac{\partial n_\epsilon}{\partial t} + \nabla \cdot \mathbf{\Gamma}_\epsilon = S_\epsilon \tag{5.7}$$

where $n_\epsilon (= n_e \bar{\epsilon})$ is electron energy density, $\bar{\epsilon}$ is electron mean energy, $\mathbf{\Gamma}_\epsilon$ represents electron energy flux and S_ϵ is an electron energy source term.

The electron energy flux and electron energy source term are given by

$$\mathbf{\Gamma}_\epsilon = -\frac{5}{3} n_\epsilon \mu \mathbf{E} - \frac{5}{3} D_e \nabla n_\epsilon \tag{5.8}$$

and

$$S_\epsilon = -e \mathbf{\Gamma_e} \cdot \mathbf{E} - n_e \sum_{i=1} \nu_i \epsilon_i \tag{5.9}$$

where ν_i is the frequency of the ith electron impact process and ϵ_i is associated with a loss of electron energy for the process. All of the reactions considered in this plasma simulation are summarized in Appendix B along with their associated rate coefficients.

One notable feature of this simulation is the way to deal with boundary conditions. Detailed analysis of particle flux toward the wall yields the following expressions:

$$\mathbf{\Gamma} \cdot \mathbf{n} = a \cdot sgn(q)\mu \mathbf{E} \cdot \mathbf{n} n + \frac{1}{4} v_{th} n - \frac{1}{2} D \nabla n \cdot \mathbf{n} \tag{5.10}$$

where $\mathbf{n}$ is the normal vector directing toward the wall and v_{th} is a thermal velocity.

In most references [69, 70, 71], it is assumed that $\nabla \cdot \mathbf{n}$ is equal to zero. Hagelaar et al. [72, 73], however, pointed out the importance of the last term of Equation 5.10 and derived an analytical solution. This simulation followed the boundary conditions in [72] and they are summarized in the following equations:

$$\mathbf{\Gamma}_j \cdot \mathbf{n} = \frac{1}{2} v_{th} n \tag{5.11}$$

for the jth neutral species,

$$\mathbf{\Gamma}_i \cdot \mathbf{n} = (2a-1)\mu_i \mathbf{E} \cdot \mathbf{n} n_i + \frac{1}{2} v_{th} n_i \tag{5.12}$$

for ions, and

$$\mathbf{\Gamma}_e \cdot \mathbf{n} = -(2a-1)\mu_e \mathbf{E} \cdot \mathbf{n} n_e + \frac{1}{2} v_{th}(n_e - n_{e,\gamma}) - 2(1-a)\sum_p \gamma_p \mathbf{\Gamma}_p \cdot \mathbf{n} \tag{5.13}$$

for the electrons, where a=1 if the drift velocity is directed toward the wall and is zero otherwise, and $n_{e,\gamma}$ is approximated as

$$n_{e,\gamma} = (1-a)\frac{\sum_p \gamma_p \bar{\epsilon}_p \mathbf{\Gamma}_p \cdot \mathbf{n}}{\frac{5}{3}\mu_e \mathbf{E} \cdot \mathbf{n}} \tag{5.14}$$

where $\bar{\epsilon_p}$ is a mean initial energy of electrons emitted by collision of species p.

All these equations and boundary conditions were coupled into the given physical geometry. They were eventually integrated into COMSOL Multi-

physics and they were solved for a two-dimensional Cartesian geometry. This finite-element simulation was also performed with a mesh resolution of 3 μm.

Figure 5.6 illustrates the driving voltage waveform and the temporal response of electron desity. In the figure, n_e represents electron density. Instead of a 20 kHz sinusoid which had been used for experiments, a 60 kHz sinusoid having 4 kV_{p-p} was applied for this numerical simulation. The discharge dynamics between those two frequencies are not expected to be different, and a 60 kHz sinusoidal voltage decreases the time cost of this simulation by a factor of 3. The frequency of 60 kHz corresponds to a period of $\sim$16.67 ms. The simulated structure has a thick glass dielectric of $\geq$200 μm. The accumulation of wall charge on the dielectric layer plays a critical role in the first several periods, and after an operation of six periods the physical parameters such as wall charge and electron density reached steady state. All the data discussed in this section are after the steady state. The breakdown voltage of this structure was 1.5–2 kV_{p-p} at a 20 kHz operation, yet the double of that voltage was applied to investigate the discharge dynamics in this configuration. Note that 20 kHz sinusoids with 4–6 kV_{p-p} had been used for the operation of the prototype of plasma antennas.

Neon gas was used to research the temporal response of electron density. Ne gas has been well studied because of its structural simplicity. It is also a convenient gas for image analysis of plasmas in experiments because of its strong visible emissions. Most importantly, compared with other noble gases or gas mixtures, neon has a low collisional frequency per unit pressure of $\sim 10^9$ /sec-Torr. This results in higher plasma conductivity. Estimated plasma parameters of several gases are provided in Table 5.1 [15]. The temporal evolution of an electron density of microchannel plasmas operating in 200 Torr of neon is shown in Figure 5.6 along with a 60 kHz driving voltage. The peak electron density is $\sim 1.5\times 10^{16}$ cm^{-3} and it corresponds to a conductivity of 2180 S/m and plasma frequency of 1.1 THz. The estimated plasma frequency of 1.1 THz indicates that this microchannel plasma antenna can operate up to the THz regime. The peak electron density is encouraging, but the full width at half max (FWHM) of the density is less than 1 μs. Collisional losses at pressures of 100s of Torr cause the electron density to decay to 1.3×10^{12} cm^{-3} in $\sim$10 μs and the minimum density occurs at t=7 and 24 μs. The minimum density gives a conductivity of 0.2 S/m and a plasma frequency of 10 GHz. The estimated minimum conductivity corresponds to

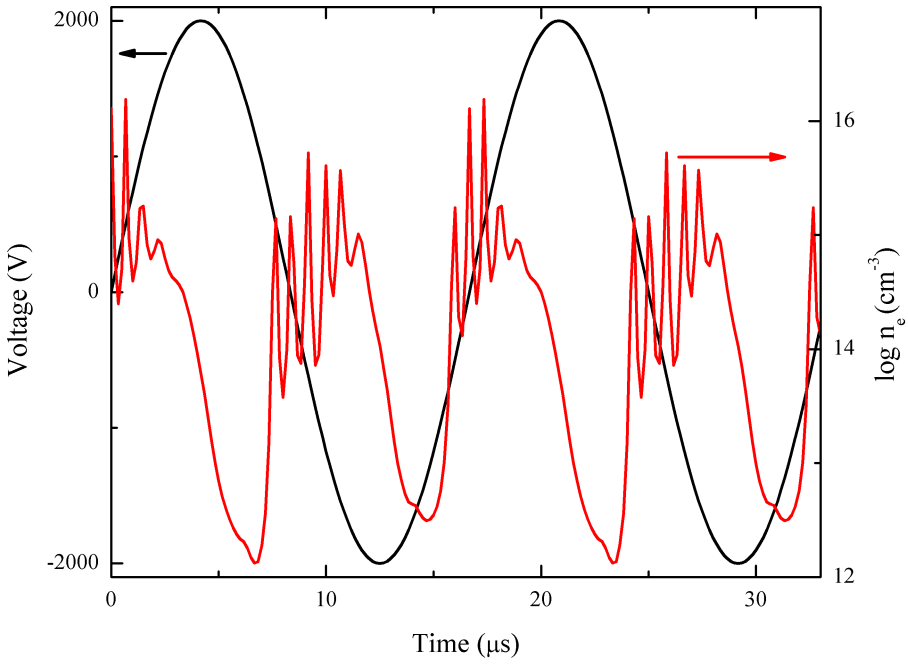

Figure 5.6: Temporal evolution of electron density in 200 Torr of Ne, excited by a 60 kHz sinusoidal voltage of 4000 V$p-p$. n_e is electron density and the unit is cm^{-3}.

Table 5.1: Estimated Parameters of Plasmas for Different Gases

Gas	ν_c/p 10^9 cm–Torr	$\mu_e \cdot p$ 10^6 cm^2–Torr/V–sec	$\frac{\sigma \cdot p}{n_e}$ 10^{-13} Torr–cm^2/ohm
Air	4	0.45	0.7
N_2	4	0.4	0.7
Ar	5	0.3	0.5
Ne	1	1.5	2.4
He	2	0.9	1.4

1/20 of the conductivity of sea water and this is the inherent hault in operation of the plasma antenna. The threshold electron density in the operating pressure of 100's of Torr is on the order of 10^{14} cm^{-3} and the inherent pause of the operation is approximately 40% at the driving frequency of 60 kHz.

One possible approach to tackling this challenge is to apply a sinusoid which has a higher frequency to arrays of microchannel plasma devices. The fundamental idea of this proposal is to excite microchannel plasmas before the electron density of microchannel plasmas decays down to 10^{14} cm^{-3} and this idea is demonstrated in Fig. 5.7. The self-oscillation of electron density is still present, but the minimum electron density at 1 MHz operation is $\sim 5.14 \times 10^{14}$ cm^{-3}. This minimum leads to a conductivity of 72.5 S/m and plasma frequency of 204 GHz. These results suggest that microchannel plasma antennas are in a continuous mode at 1 MHz operation and the operating frequency can be as high as 200 GHz.

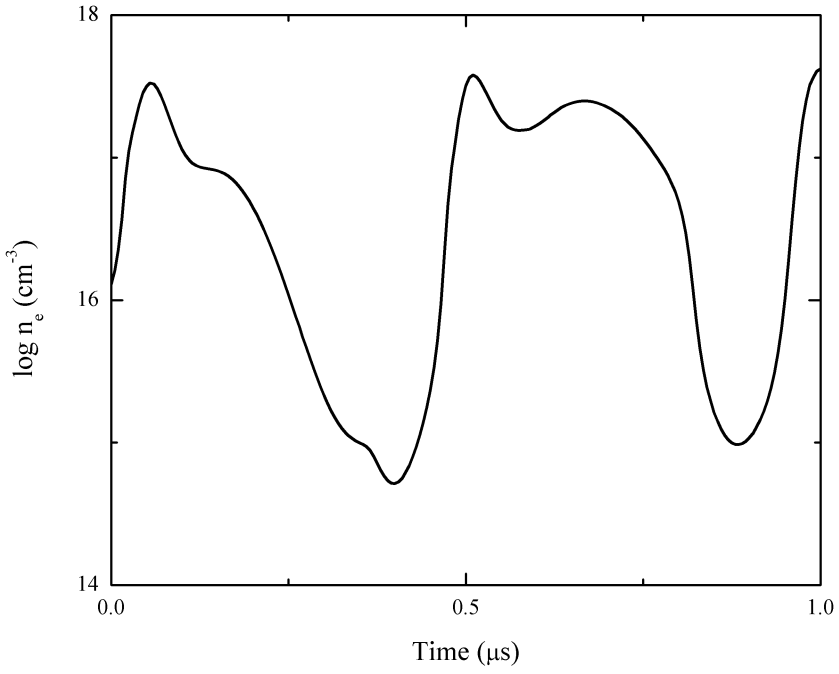

Figure 5.7: Temporal evolution of electron density in 200 Torr of Ne, excited by a 1 MHz sinusoidal voltage of 4000 V_{p-p}. n_e is electron density and the unit is cm^{-3}.

5.3 RF Transmission Measurement

Tests of RF transmission through micochannel plasmas were conducted in order to understand how well the microchannel plasmas mimic metal in traditional antennas and to infer an electrical conductivity of plasmas. These experiments were also used to validated simulations. To operate microchannel plasmas at several MHz, the configuration of the prototype needed to be redesigned. Instead, in this section, a measurement scheme was devised to measure the transient transmission of RF signal and is illustrated in Figure 5.8. The key change from conventional RF transmission measurements

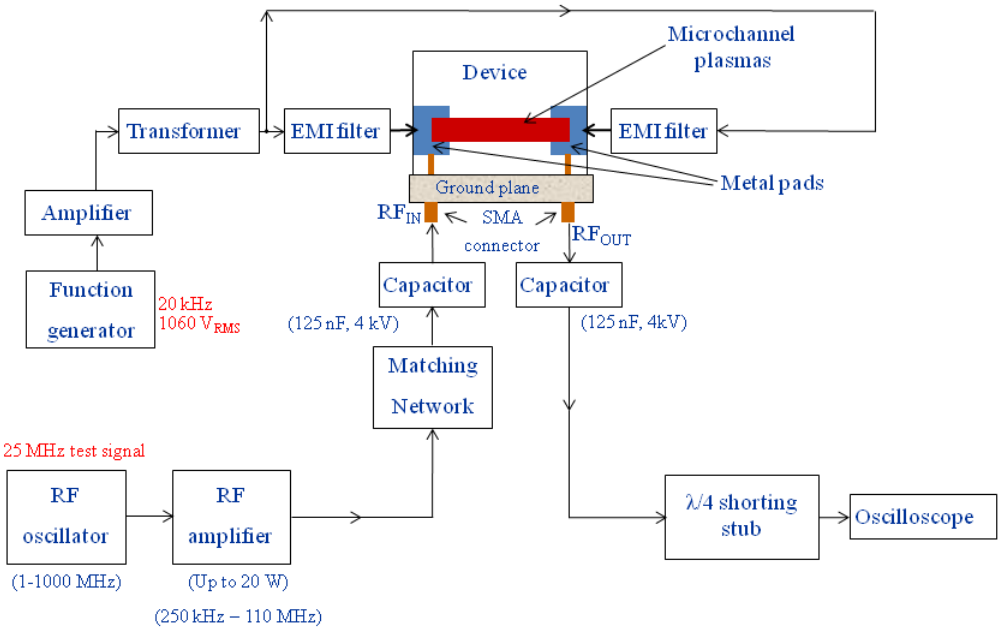

Figure 5.8: Experimental setup for RF transmission measurements through microchannel plasmas.

was the introduction of an oscilloscope (Tektronix, TDS5104B) with a sampling rate of 5 GS/s. A network analyzer provides time-averaged data, but this averaging process decreases the transmitted signal and the signal may lie below the noise floor. Note that the measured duty cycle of the discharge current is only ~0.034 % at the operation of 20 kHz. Microchannel plasmas

were operated at 20 kHz frequency and 1060 V_{RMS}, and an RF signal was fed through the left SMA connector. The transmitted signal was observed through the right SMA connector. Capacitors were included in this measurement scheme to block the driving signal with a high voltage of 1060 V_{RMS} and a frequency of 20 kHz. One quarter-wave ($\lambda/4$) shorting stub decreased the RF signal of 25 MHz by 20 dB. These two components were used to protect the oscilloscope. EMI filters were introduced to block RF tranmission through the wires needed to drive the plasmas.

In this mesurement, the frequency of an RF test signal was chosen to be 25 MHz because of the limit in the matching network between the microchannel device and the RF amplifier, and the frequency characteristics of the EMI filter. In addition to taking the measurement of an RF transmission when the plasma was on, measurements of RF transmission when plasma was off and plasma noise were also performed to eliminate artifacts such as RF coupling between the left and right metal pad. Figure 5.9 presents representative output signals in the time domain, and RF transmission loss is obtained by

$$
\begin{aligned}
&Transmission\ \text{Loss}|^{25MHz} \\
=&20 \times log_{10}(\text{FFT Magnitude of RF Transmission} \\
&- \text{FFT Magnitude of Plasma Noise - FFT Magnitude of RF Coupling}) \\
&- 20 \times log_{10}(\text{FFT Magnitude of Reference})
\end{aligned}
\tag{5.15}
$$

In this calculation, a fast Fourier transform (FFT) was carried out over a time window of 0.996 μs and yielded transmission losses in the range of 56 to 63 dB. The FWHM of the discharge current was only 8.5 ns during the time interval of 0.996 μs and the predicted transmission loss would be 15–25 dB under 100% duty cycle of discharge current. This transmission loss can be converted to the conductivity of the microchannel plasmas from the basic theory of microstrip antennas. The conductor loss, in general, is much more significant than dielectric loss. The dielectric loss is ignored in the following calculation and the plasma conductivity is given by

$$
\sigma_{plasmas} = \left[\frac{8.686}{\alpha_C \cdot W \cdot Z_0} \times \sqrt{\frac{2}{\omega \cdot \mu_0}} \right]^2 \tag{5.16}
$$

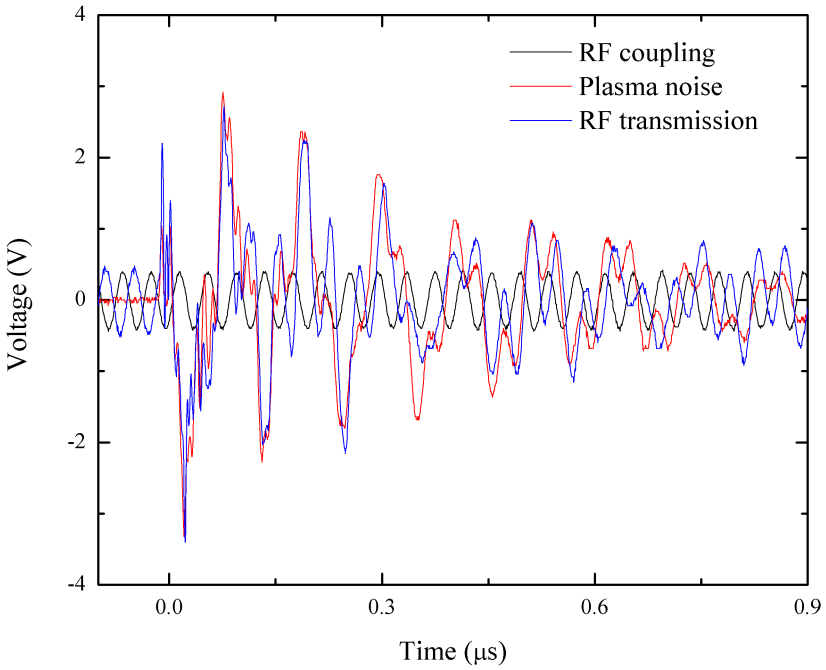

Figure 5.9: RF coupling, plasma noise and transmitted RF signal in the time domain.

where α_C is conductor loss of a microstrip line, Z_0 is the characteristic impedance of a microstrip line and μ_0 is the permeability of free space.

The time-averaged conductivity of 35–60 S/m is obtained, and this leads to the time-averaged electron density on the order of 10^{14} cm^{-3}. The assessed conductivity from transmission measurements supports the simulation results. Both simulations and experiments suggest that these microchannel plasma devices have great potential as antennas.

5.4 Plasma Noise Measurements

For the application of plasmas as antennas, it is important to understand their noise characteristics. It is encouraging that recent research on plasma antennas showed that the noise level of surface wave driven plasma antennas was only 4 dB higher than a receiver sensitivity of −116 dBm [74]. The noise characteristics of microchannel plasmas are studied with the experimental setup given in Figure 5.10. It is noted that arrays of microchannel plasmas are operated by applying a 20 kHz sinusoid having 1150 V_{RMS} to the metal pad on the left in the figure. Two capacitors were introduced to block the driving voltage from the metal pad on the left of the microchannel plasma device. Then, the noise signals were measured at both SMA connectors of RF_{OUT1} and RF_{OUT2} in the Figure 5.10. It is assumed that all the noise from microchannel plasmas is coupled into the connector and it is measured at the oscilloscope (Tektronix, TDS 5104B).

Figure 5.11 displays the magnitude of the FFT of the measured signal at RF_{OUT1}. The signal strength at 20 kHz is almost 110 dB in the magnitude of the FFT and this is from the driving voltage. It is observed that much of the noise lies at the freqeuncy region of less than 1 MHz and it is up to 25 dB in the magnitude of FFT from the noise floor. It seems that the measured signal at the node of RF_{OUT2} describes the noise of microchannel plasmas better. The node of RF_{OUT1} is more exposed to the noise from plasma-driving parts such as the function generator and the power amplifier. For example, the noise from the power amplifier is known to be acoustic noise and its frequency range includes the frequency components of the measured noise of RF_{OUT1}. The power spectrum of RF_{OUT2} is shown in Figure 5.12. Interestingly, this spectrum shows radio frequencies for local public services and businesses

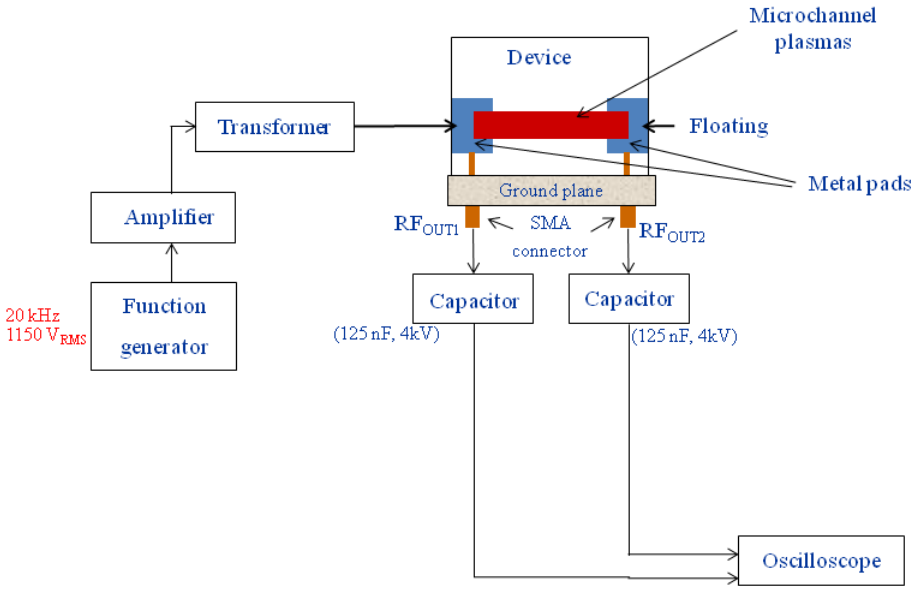

Figure 5.10: Experimental setup to characterize the noise of microchannel plasmas.

in Urbana and Champaign. This is primarily because these measurements were not performed in a shielded environment. This does, however, provide evidence that this prototype of microplasma antennas functions as a receiving antenna because the local FM bands show up only when the plasmas are on. The highest signal strength is from WPGU and the signal is almost 40 dB higher than the noise floor. WPGU is the student-run radio station at the University of Illinois at Urbana-Champaign and its frequency is 107.1 MHz. WPGU is just 1.4 miles from the testing area. The noise from microchannel plasmas is also encouraging because the highest frequency of 20 MHz from the noise observed at RF_{OUT2} is still better than that observed for plasma columns [63]. All these results lead to the conclusion that microchannel plasma devices have great potential as invisible antennas.

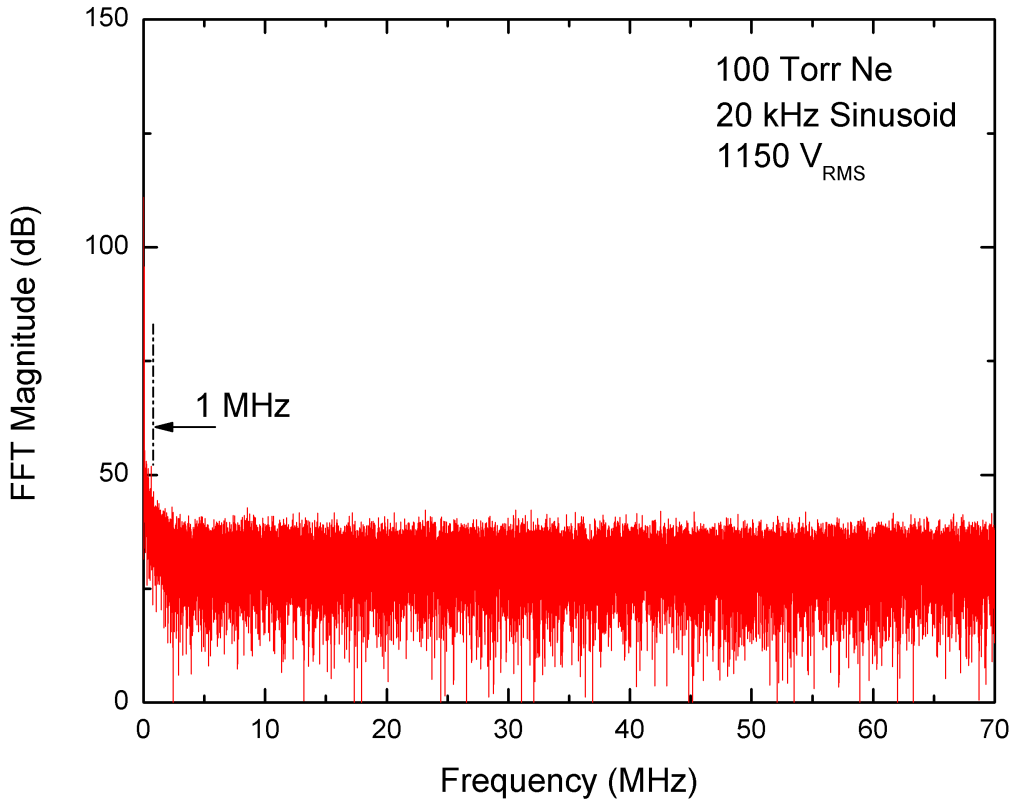

Figure 5.11: Magnitude of the FFT of the measured signal at RF_{OUT1}.

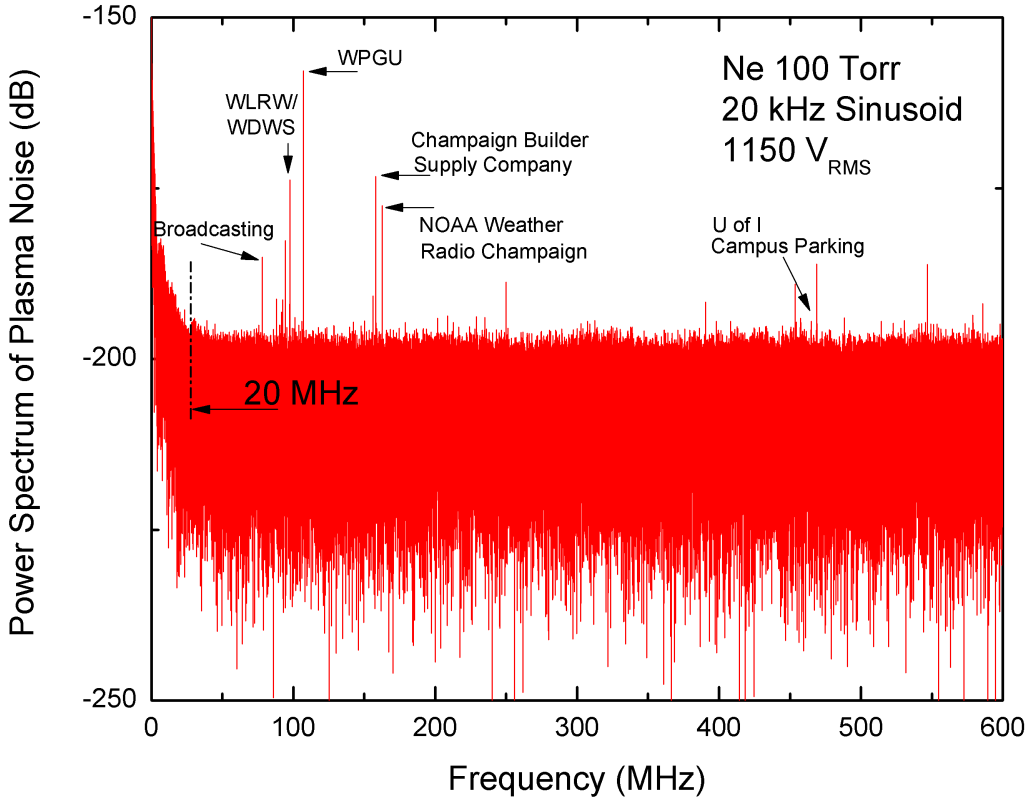

Figure 5.12: Magnitude of the FFT of the measured signal at RF_{OUT2}.

CHAPTER 6

CONCLUSIONS

This dissertation has explored the underlying physics in arrays of glass microplasmas, produced in cavities having the characteristic dimensions of 25–800 μm, that is responsible for coupling a microplasma with its neighbors. This work also demonstrated a proof of concept to use arrays of microchannel plasmas as invisible antennas. There are several significant contributions of this work to both plasma science and engineering. First of all, this work demonstrated a novel glass micromaching using replica molding and micropowder blasting. By applying replica molding and micro-imprinting into a mask fabrication, high-resolution of 25 μm, scalability up to several 10's of cm^2 and low cost have been achieved. This new class of glass fabrication techniques laid a foundation to extensively research and characterize glass microcavity or microchannel plasmas having the characteristic dimensions of 25 μm–800 μm.

Arrays of microcavity and microchannel plasma devices with different geometries and electrode configurations are tested in this work. All the microplasmas confined in the spatial scale of 25–800 μm showed stable and uniform operation for different gas mixtures and pressures. Intriguing phenomena of optical and electrical coupling in arrays of microcavity and microchannel plasma devices have been observed and investigated. Each element of the plasma arrays is physically separated, yet is optically and/or electrically coupled to its neighbors. The spatial broadening and intensification of the visible emission from linear plasma channels operating in Ne were investigated. By varying the pitch for the array and operating frequency, it was demonstrated that optogalvanic effects play a critical role for the optical coupling.

An electrical modeling of arrays of micrcavity plasma devices with an 80 μm gap showed the transition from a Townsend-like to an abnormal glow discharge. This investigation elucidated the underlying mechanism of the

positive slope in V-I curves for arrays of microcavity plasma devices. Temporal bistable oscillations of visible emissions were also observed during the transition. It appears that each microcavity plasma is spatially coupled to its neighbors during the oscillations, possibly by the time-varying distribution of charge deposited on the dielectric layer. Interestingly, the coupling of bounded and free microdischarge was also reported. Space charge near a dielectric layer and geometrical effects of microcavities seem to be responsible for the interactions. Ongoing study is necessary to elucidate the underlying mechanisms of the interesting phenomena of the plasma-plasma interaction.

Another objective of this dissertation was to explore the possibility of using microchannel plasma devices as antennas. Both the simulation of electrical conductivity and the experiments on RF transmissions through the plasma channels suggest that microchannel plasmas can be substitutes for metal patches of microstrip antennas. This work was limited in that the operating frequency was 20 kHz and the duty cycle of the plasmas was less than 0.05 %. The setup designated for measuring the transient signal from the plasma, however, successfully presented the performance of microchannel plasma devices as receiving antennas. It is also proposed that research on microplasma antennas focus on RF-driven microplasma devices for quasi-continuous operation. This work is preliminary but significant in that it shows the great potential of microplasma devices as invisible antennas.

In sum, microplasmas are scientifically intriguing subjects with enormous potential for applications. The theoretical and experimental investigation must be given to this emerging field to explain and utilize novel phenomena which were not observed in macroplasmas. Of particular interest is to develop invisible antennas using arrays of microplasmas. Future research will focus on the development of microchannel plasma structures operating in the MHz frequency domain. Several dimensions including the width of microchannels and the pitch of arrays may be further optimized, and multi-layer structures will be considered for novel applications.

APPENDIX A

DERIVATION OF ABSORPTION COEFFICIENT IN HOMOGENEOUS PLASMAS

The absorption coefficient is derived from the wavevector and the complex permittivity of plasmas, with the assumption that plasmas are homogeneous. Homogeneous plasmas are assumed in order to reduce mathematical complexity in this derivation. The complex permittivity of plasmas is given by

$$\epsilon_p = \left(1 - \frac{f_p^2}{f_0^2 + \nu_m^2}\right) - j \cdot \left(\frac{\nu_m}{f_0} \cdot \frac{f_p^2}{f_0^2 + \nu_m^2}\right) \tag{A.1}$$

where ϵ_p is the relative dielectric constant of plasmas, f_p is the plasma frequency, f_0 is the frequency of an oscillating electric field and ν_m is the collision frequency for momentum transfer. The plasma frequency is a function of the electron density and is given by

$$\omega_p = 2\pi f_p = \sqrt{\frac{n_0 e^2}{m_e \epsilon_0}} \approx 9000\sqrt{n_e} \tag{A.2}$$

where m_e is the mass of an electron, ϵ_0 is the permittivity of free space, n_0 is the average density of electrons, e is charge on an electron and f_p is expressed in Hz.

The wavevector can be obtained from the complex permittivity by the following expression:

$$k = \omega_0\sqrt{\epsilon_0\mu_0}\sqrt{\epsilon_p} = k_0\sqrt{\epsilon_p} = k_r - j \cdot k_i \tag{A.3}$$

where k_0 is the wavevector of free space, ϵ_0 is the permittivity of free space and ν_0 is the permeability of free space. k_r and k_i are the real part of k_p and the negative of the imaginary part of k_p, respectively.

Note that k_i must be positive to be physically acceptable because a positive value for k_i predicts the absorption of electromagnetic waves by plasmas rather than gain.

Let the ϵ_p be $r^{1/2}e^{j\phi}$. Then, the ratios of k_r/k_0 and k_i/k_0 are given by

$$k_r/k_0 = r^{1/4}cos(\phi/2) \tag{A.4}$$

$$k_i/k_0 = -r^{1/4}sin(\phi/2) \tag{A.5}$$

Integrating Equation A.4–A.5 with Equation A.1, the ϕ and r are given by

$$\phi/2 = -tan^{-1}\left[\frac{\nu_m \cdot f_p^2}{f_0 \cdot \left(f_0^2 + \nu_m^2 - f_p^2\right)}\right], \quad Re(\epsilon_p) > 0 \tag{A.6}$$

$$r = \frac{\nu_m^2 \cdot f_0^4}{f_0^2\left(\nu_m^2 + f_0^2\right)^2} + \left(1 - \frac{f_p^2}{\nu_c^2 + f_0^2}\right)^2 = \frac{\nu_m^2 \cdot f_0^2 + \left(f_0^2 - f_p^2\right)^2}{f_0^2\left(\nu_m^2 + f_0^2\right)} \tag{A.7}$$

Therefore, the absorption coeffcient is given by

$$\begin{aligned} k_i &= k_0 \cdot \left(\frac{\nu_m^2 \cdot f_0^2 + \left(f_0^2 - f_p^2\right)^2}{f_0^2(\nu_m^2 + f_0^2)}\right)^{1/4} \times \\ &\quad sin\left(tan^{-1}\left[\frac{\nu_m \cdot f_p^2}{f_0 \cdot \left(f_0^2 + \nu_m^2 - f_p^2\right)}\right]\right), \quad Re(\epsilon_p) > 0\ . \end{aligned} \tag{A.8}$$

APPENDIX B

REACTION MECHANISMS IN NEON

Electrical conductivity of microchannel plasmas has been predicted by finite-element simulations in Chapter 4. The detailed physics was also described. The reaction mechanisms included in the simulation are summarized in Table B.1.

Table B.1: Reaction Mechanism in Neon

Reaction mechanism Reaction	Rate coefficient, cm^3–s^{-1}	Reference
Electron impact processes		
$e + Ne \rightarrow e + Ne^m$	1	[75]
$e + Ne \rightarrow e + Ne^*$	1	[75]
$e + Ne \rightarrow e + Ne^{**}$	1	[75]
$e + Ne^m \rightarrow e + e + Ne^+$	1	[52]
$e + Ne^* \rightarrow e + e + Ne^+$	1	[76]
$e + Ne^* \rightarrow e + Ne^{**}$	1	[77]
$e + Ne^m \rightarrow e + Ne^{**}$	1	[77]
$e + Ne^+ \rightarrow Ne^{**}$	$4.0\times10^{-13}\mathrm{T}_e^{-0.5}$	[5]
$e + Ne^+ + M \rightarrow Ne^{**} + M$	1.0×10^{-38}	[5]
$e + Ne_2^+ \rightarrow Ne^m + Ne$	$2.7\times10^{-14}\mathrm{T}_e^{-0.5}$	[5]
$e + Ne_2^+ \rightarrow Ne^* + Ne$	$1.0\times10^{-14}\mathrm{T}_e^{-0.5}$	[5]
$e + Ne_2^+ \rightarrow Ne^{**} + Ne$	$3.7\times10^{-14}\mathrm{T}_e^{-0.5}$	[5]
Heavy particle collision		
$Ne^m + Ne \rightarrow Ne^* + Ne$	4.2×10^{-14}	[5]
$Ne^* + Ne \rightarrow Ne^m + Ne$	3.4×10^{-14}	[5]
$Ne^m + Ne^m \rightarrow e + Ne^+ + Ne$	3.2×10^{-10}	[5]
$Ne^m + Ne^* \rightarrow e + Ne^+ + Ne$	3.2×10^{-10}	[5]
$Ne^m + Ne^{**} \rightarrow e + Ne^+ + Ne$	3.2×10^{-10}	[5]

Continued on next page

Table B.1 – Continued

Reaction mechanism	Rate coefficient, cm^3–s^{-1}	References
Heavy particle collision		
$Ne^* + Ne^* \rightarrow e + Ne^+ + Ne$	3.2×10^{-10}	[5]
$Ne^* + Ne^{**} \rightarrow e + Ne^+ + Ne$	3.2×10^{-10}	[5]
$Ne^{**} + Ne^{**} \rightarrow e + Ne^+ + Ne$	3.2×10^{-10}	[5]
$Ne^m + Ne + Ne \rightarrow Ne_2^* + Ne$	4.1×10^{-34}	[5]
$Ne^* + Ne + Ne \rightarrow Ne_2^* + Ne$	4.1×10^{-34}	[5]
$Ne^{**} + Ne + Ne \rightarrow Ne_2^* + Ne$	4.1×10^{-34}	[5]
$Ne^+ + Ne + Ne \rightarrow Ne_2^+ + Ne$	4.4×10^{-32}	[5]
Radiative transitions		
$Ne^{**} \rightarrow Ne^m + h\nu$	1.84×10^7	[5]
$Ne^{**} \rightarrow Ne^* + h\nu$	1.25×10^7	[5]
$Ne^* \rightarrow Ne + h\nu$	6×10^6	[5]
$Ne_2^* \rightarrow Ne + h\nu$	3.6×10^8	[5]

[a]Rate coefficients were determined by the cross section in the reference and the electron mean energy etimated from the energy balance equation.

REFERENCES

[1] R. P. Feynman, "There's plenty of room at the bottom," talk presented at annual meeting of the American Physical Society, Pasadena, CA, 1959. [Online]. Available: http://www.zyvex.com/nanotech/feynman.html.

[2] K. S. Novoselov, A. K. Geim, S. V. Morozov, D. Jiang, Y. Zhang, S. V. Dubonos, I. V. Grigorieva, and A. A. Firsov, "Electric field effect in atomically thin carbon films," *Science*, vol. 306, pp. 666–669, 2004.

[3] T. Ha, T. Enderle, P. R. Selvin, D. S. Chemla, and S. Weiss, "Quantum jumps of single molecules at room temperature," *Chem. Phys. Lett.*, vol. 271, pp. 1–5, 1997.

[4] S.-J. Park and J. G. Eden, "13-30 micron diameter microdischarge devices: Atomic ion and molecular emission at above atmospheric pressures," *Appl. Phys. Lett.*, vol. 81, pp. 4127–4129, 2002.

[5] M. J. Kushner, "Modeling of microdischrge devies: Pyramidal structures," *J. Appl. Phys.*, vol. 95, pp. 846–859, 2004.

[6] N. Ostrom and J. Eden, "Microcavity plasma photodetectors: photosensitivity, dynamic range, and the plasma-semiconductor interface," *Appl. Phys. Lett.*, vol. 87, pp. 14 110 101–14 110 103, 2005.

[7] C. J. Wagner, P. A. Tchertchian, and J. G. Eden, "Coupling electron-hole and electron-ion plasmas: Realization of an npn plasma bipolar junction phototransistor," *Appl. Phys. Lett.*, vol. 97, pp. 13 410 201–13 410 203, 2010.

[8] A. Paul, R. A. Bartels, R. Tobey, H. Green, S. Weiman, I. P. Christov, M. M. Murnane, H. C. Kapteyn, and S. Backus, "Quasi-phase-matched generation of coherent extreme-ultraviolet light," *Nature*, vol. 421, pp. 51–54, 2003.

[9] A. Braun, G. Korn, X. Liu, D. Du, J. Squier, and G. Mourou, "Self-channeling of high-peak-power femtosecond laser pulses in air," *Opt. Express*, vol. 20, pp. 73–75, 1995.

[10] C. P. Hauri, W. Kornelis, F. W. Helbing, A. Heinrich, A. Couairon, A. Mysyrowicz, J. Biegert, and U. Keller, "Generation of intense, carrier-envelope phase-locked few-cycle laser pulses through filamentation," *Appl. Phys. B*, vol. 79, pp. 673–677, 2004.

[11] T. S. Anderson, J. H. Ma, S.-J. Park, and J. G. Eden, "Multichannel microchemical reactor comprising replica-molded microplasma devices: chemiluminescence and sulfur deposition in Ar/Cs_2 flows," *IEEE Trans. Plasma Sci.*, vol. 36, pp. 1250–1251, 2008.

[12] S. H. Sung, T. M. Spinka, Y. M. Kang, A. G. Berger, S.-J. Park, and J. G. Eden, "Evidence for nearest neighbor coupling in arrays of ellipsoidal microcavity plasmas," *IEEE Trans. Plasma Sci.*, vol. 36, pp. 1246–1247, 2008.

[13] J. A. Bittencourt, *Fundamentals of Plasma Physics*. New York, NY: Springer, 2004.

[14] B. E. Cherrington, *Gaseous Electronics and Gas Lasers*. New York, NY: Pergamon Press, 1979.

[15] A. Fridman and L. A. Kennedy, *Plasma Physics and Engineering*. New York, NY: CRC Press, 2004.

[16] M. A. Lieberman and A. J. Lichtenberg, *Principle of Plasma Discharges and Material Processing*. New York, NY: Wiley-Interscience, 2005.

[17] Y. P. Raizer, *Gas Discharge Physics*. New York, NY: Springer-Verlag, 1987.

[18] D. K. Doughty and J. E. Lawler, "Model of optogalvanic effects in the neon positive column," *Phy. Rev. A*, vol. 28, pp. 773–780, 1983.

[19] J. R. Nestor, "Optogalvanic spectra of neon and argon in glow discharge lamps," *Appl. Opt.*, vol. 21, pp. 4154–4157, 1982.

[20] J. W. Frame, D. J. Wheeler, T. A. DeTemple, and J. G. Eden, "Microdischarge devices fabricated in silicon," *Appl. Phys. Lett*, vol. 71, pp. 1165–1167, 1997.

[21] S. J. Park and J. G. Eden, "13–30 micron diameter microdischarge devices: Atomic ion and molecular emission at above atmospheric pressures," *Appl. Phys. Lett.*, vol. 81, pp. 1165–1167, 2002.

[22] S.-J. Park, K.-S. Kim, and J. G. Eden, "Ultraviolet emission intensity, visible luminance, and electrical characteristics of small arrays of Al/Al_2O_3 microcavity plasma devices operating in Ar/N_2 or Ne at high–power loadings," *J. Appl. Phys.*, vol. 99, pp. 02 610 701–02 610 703, 2006.

[23] S. J. Park, J. G. Eden, K. Jain, and M. A. Klosner, "Flexible arrays of Ni/polyimide/Cu microplasma devices with a dielectric barrier and excimer laser ablated microcavities," *J. J. Appl. Phys.*, vol. 45, pp. 8221–8224, 2006.

[24] K. Kolari, "Deep plasma etching of glass with a silicon shadow mask," *Sensors Actuat. A-Phys.*, vol. 141, pp. 677–684, 2008.

[25] X. Li, T. Abe, Y. Liu, and M. Esashi, "Fabrication of high–density electrical feed-throughs by deep–reactive–ion etching of pyrex glass," *J. MEMS*, vol. 11, pp. 677–684, 2008.

[26] X. Li, T. Abe, Y. Liu, and M. Esashi, "Smooth surface glass etching by deep reactive ion etching with SF_6 and Xe gases," *J. Vac. Sci. Technol. B*, vol. 216, pp. 2545–2549, 2003.

[27] P. E. Dyer, S. M. Maswadi, C. D. Walton, M. Ersoz, P. D. I. Fletcher, and V. N. Paunov, "157 nm laser micromachining of n–bk7 glass and replication for microcontact printing," *Appl. Phys. A*, vol. 77, pp. 391–394, 2003.

[28] A.-G. Pawlowski, A. Sayah, and M. A. M. Gijs, "Precision Poly–(Dimethyl Siloxane) masking technology for high–resolution powder blasting," *J. MEMS*, vol. 14, pp. 619–624, 2003.

[29] A. Sayah, P. A. Thivolle, V. K. Parashar, and M. A. M. Gijs, "Fabrication of microfluidic mixers with varying topography in glass using the powder–blasting process," *J. Micromech. Microeng.*, vol. 19, pp. 085 024–085 031, 2009.

[30] H. Wensink and M. C. Elwenspoek, "A closer look at the ductile and brittle transition in solid particle erosion," *Wear*, vol. 253, pp. 1035–1043, 2002.

[31] C. Penache, A. Braeuning-Demian, L. Spielberger, and H. Schmidt-Boecking, "On the influence of core laminations upon power transformer noise," in *Proc. Int. Symp. on High Pressure Low Temperature Plasma Chemistry*, Greifswald, Germany, Sep. 2000, pp. 501–503.

[32] Y.-B. Guo and F. C.-N. Hong, "Radio–frequency microdischarge arrays for large–area cold atmospheric plasma generation," *Appl. Phys. Lett.*, vol. 82, pp. 337–339, 2003.

[33] K. S. Kim, T. L. Kim, J. K. Yoon, S. J. Park, and J. G. Eden, "Control of cavity cross section in microplasma devices: Luminance and temporal response of 200×100 and 320×160 arrays with parabolic Al_2O_3 microcavities," *Appl. Phys. Lett.*, vol. 94, pp. 01 150 301–01 150 303, 2009.

[34] J. Chen, S. J. Park, Z. Fan, C. Liu, and J. G. Eden, "Development and characterization of micromachined hollow cathode plasma display devices," *J. MEMS*, vol. 11, no. 5, pp. 01 150 301–01 150 303, 2002.

[35] R. Ganter, T. Callegari, L. Pitchford, and J. P. Boeuf, "Efficiency of ac plasma display panels from diagnostics and models," *Appl. Surface Sci.*, vol. 192, pp. 299–308, 2002.

[36] W. Wiete and N.-K. Ludmila, "Treatment of vitiligo with UV–B radiation vs topical psoralen plus UV–A," *Arch. Dermatol.*, vol. 133, pp. 1525–1528., 1997.

[37] A. B. Shekhter, V. A. Serezhenkov, T. G. Rudenko, A. V. Pekshev, and A. F. Vanin, "Beneficial effect of gaseous nitric oxide on the healing of skin wounds," *Nitric Oxide*, vol. 12, pp. 210–219, 2005.

[38] J. Drimal and J. Janca, "Biological purification of water by an ozoniser with a discharge tube electrode," *J. Phys. D:Appl. Phys.*, vol. 23, pp. 7–11, 1990.

[39] H. W. Herrmann, I. Henins, J. Park, and G. S. Selwyn, "Decontamination of chemical and biological warfare (CBW) agents using atmospheric pressure plasma jet (APPJ)," *Phys. of Plasmas*, vol. 6, pp. 2284–2289, 1999.

[40] A. N. Goyette, W. B. Jameson, L. W. Anderson, and J. E. Lawler, "An experimental comparison of rotational temperature and gas kinetic temperature in a h_2 discharge," *J. Phys. D:Appl. Phys.*, vol. 29, pp. 1197–1201, 1996.

[41] B. J. Ricconi, "Microcavity plasmas in rare gas/water vapor mixtures: ultraviolet emission from the hydroxyl radical," M.S. thesis, University of Illinois at Urbana–Champaign, Urbana, 2006.

[42] G. H. Dieke and H. M. Crosswhite, "The ultraviolet bands of OH fundamental data," *J. Quant. Spec. Radiat. Transfer*, vol. 29, pp. 1197–1201, 1996.

[43] O. Sakai, T. Sakaguchi, and K. Tachibana, "Photonic bands in two-dimensional microplasma arrays i. theoretical derivation of band structures of electromagnetic waves," *J. Appl. Phys.*, vol. 101, pp. 07 330 401–07 330 409, 2007.

[44] R. M. Sankaran, D. Holunga, R. C. Flagan, and K. P. Giapis, "Synthesis of blue luminescent Si nanoparticles using atmospheric pressure microdischarges," *Nano Lett.*, vol. 5, p. 537541, 2005.

[45] H. J. Lee, C. H. Shon, Y. S. Kim, S. Kim, G. C. Kim, and M. G. Kong, "Degradation of adhesion molecules of g361 melanoma cells by a non-thermal atmospheric pressure microplasma," *New J. Phys.*, vol. 11, pp. 11 502 601–11 502 613, 2009.

[46] K. H. Becker, K. H. Schoenbach, and J. G. Eden, "Microplasmas and applications," *J. Phys. D:Appl. Phys.*, vol. 39, no. 3, pp. R55–R70, 2006.

[47] N. P. Ostrom and J. G. Eden, "Visible emission contours for neon plasmas in silicon microcavity discharge devices: pressure dependence of spatially resolved fluorescence above the anode plane," *IEEE Trans. Plasma Sci.*, vol. 33, pp. 576–577, 2005.

[48] J. R. Nestor, "Optogalvanic spectra of neon and argon in glow discharge lamps," *Appl. Opt.*, vol. 21, pp. 4154–4156, 1982.

[49] J. R. Dixon and F. A. Grant, "Decay of the triplet p levels of neon," *Phys. Rev.*, vol. 107, pp. 118–124, 1957.

[50] V. N. Ochkin, N. G. Preobrazhensky, and N. Y. Shaparev, *Optogalvanic Effect in Ionized Gas.* London, United Kingdom: CRC Press, 1999.

[51] F. Massines, N. Gherardi, N. Naude, and P. Segur, "Glow and Townsend dielectric barrier discharge in various atmosphere," *Plasma Phys. Control. Fusion*, vol. 47, pp. B577–B588, 2005.

[52] H.-J. Lee and J. G. Eden, "Simulation study on the discharge characteristics of the double parabolic Al_2O_3 microcavity device," to be published.

[53] I. Enachea, N. Naude, J. P. Cambronne, N. Gherardib, and F. Massines, "Electrical model of the atmospheric pressure glow discharge (APGD) in helium," *Eur. Phys. J. Appl. Phys.*, vol. 33, pp. 15–21, 2006.

[54] J. P. Boeuf, L. C. Pitchford, and K. H. Schoenbach, "Predicted properties of microhollow cathode discharges in xenon," *Appl. Phys. Lett.*, vol. 86, pp. 07 150 101–07 150 103, 2005.

[55] M. Klein, N. Miller, and M. Walhout, "Time-resolved imaging of spatiotemporal patterns in a one-dimensional dielectric-barrier discharge system," *Phys. Rev. E*, vol. 64, pp. 02 640 201–02 640 205, 2001.

[56] Q.-Y. Nie, C.-S. Ren, D.-Z. Wang, S.-Z. Li, J.-L. Zhang, and M. G. Kong, "Self-organized pattern formation of an atmospheric pressure plasma jet in a dielectric barrier discharge configuration," *Appl. Phys. Lett.*, vol. 90, pp. 22 150 401–22 150 403, 2007.

[57] L. Dong, Y. He, W. Liu, R. Gao, H. Wang, and H. Zhao, "Hexagon and square patterned air discharges," *Appl. Phys. Lett.*, vol. 90, pp. 03 150 401–03 150 403, 2007.

[58] L. Dong, W. Liu, H. Wang, Y. He, W. Fan, and R. Gao, "Honeycomb hexagon pattern in dielectric barrier discharge," *Phy. Rev. E*, vol. 76, pp. 04 621 001–04 621 004, 2007.

[59] T. Shirafujia, T. Kitagawa, T. Wakai, and K. Tachibana, "Observation of self-organized filaments in a dielectric barrier discharge of Ar gas," *Appl. Phys. Lett.*, vol. 83, pp. 2309–2311, 2003.

[60] M. Kong, B. Partoens, and F. M. Peeters, "Transition between ground state and metastable states in classical two-dimensional atoms," *Phys. Rev. E*, vol. 65, pp. 04 660 201–04 660 213, 2002.

[61] N. Blaunstein and C. Christodoulou, *Radio Propagation and Adaptive Antennas for Wireless Communication Links*. New York, NY: Wiley-Interscience, 2007.

[62] C. B. Wharton and D. M. Slager, "Microwave determination of plasma density profiles," *J. Appl. Phys.*, vol. 31, pp. 428–430, 1960.

[63] J. P. Rayner and A. P. Whichello, "Physical characteristics of plasma antennas," *IEEE Trans. Plasma Sci.*, vol. 32, no. 1, pp. 269–281, 2004.

[64] J. Mathew, R. F. Fernsler, R. A. Meger, J. A. Gregor, D. P. Murphy, R. E. Pechacek, and W. M. Manheimer, "Generation of large area, sheet plasma mirrors for redirecting high frequency microwave beams," *Phy. Rev. Lett.*, vol. 77, no. 10, pp. 1982–1985, 1996.

[65] R. J. Vidmar, "On the use of atmospheric pressure plasmas as electromagnetic reflectors and absorbers," *IEEE Trans. Plasma Sci.*, vol. 18, no. 4, pp. 733–741, 1990.

[66] A. E. Robson, R. L. Morgan, and R. A. Merger, "Demonstration of a plasma mirror for microwaves," *IEEE Trans. Plasma Sci.*, vol. 20, no. 6, pp. 1036–1040, 1992.

[67] S. H. Sung, I. C. Hwang, S. J. Park, and J. G. Eden, "Inter-channel optical coupling within linear arrays of microplasma generated in 25-200 μm wide glass channels," *Appl. Phys. Lett.*, vol. 20, no. 6, pp. 1036–1040, 2010.

[68] R. Compton, Z. Popovic, G. Rebeiz, P. Tong, and D. Rutledge, "Bow-tie antennas on a dielectric half-space: theory and experiment," *IEEE Trans. Antennas and Propagation*, vol. 35, pp. 622–631, 1987.

[69] C. Punset, J.-P. Boeuf, and L. C. Pitchford, "Two-dimensional simulation of an alternating current matrix plasma display cell: Cross-talk and other geometric effects," *J. Appl. Phys.*, vol. 83, pp. 1884–1897, 1998.

[70] P. J. Drallos, V. P. Nagorny, and W. Williamson, "A kinetic study of the local field approximation in simulations of ac plasma display panels," *Plasma Sources Sci. Tech.*, vol. 4, no. 4, pp. 576–590, 1995.

[71] J. H. Seo and J. G. Eden, "Two-dimensional simulation of ac–driven microplasmas confined 100–300 μm diameter cylindrical microcavities in dielectric barrier discharges," *J. Appl. Phys.*, vol. 100, pp. 123 302 – 123 302–8, 2006.

[72] G. J. M. Hagelaar, F. J. de Hoog, and G. M. W. Kroesen, "Boundary conditions in fluid models of gas discharges," *Phy. Rev. E*, vol. 62, no. 1, pp. 1452–1454, 2000.

[73] G. J. M. Hagelaar, G. M. W. Kroesen, U. Slooten, and H. Schreuders, "Modeling of the microdischarges in plasma addressed liquid crystal displays," *J. Appl. Phys.*, vol. 88, no. 5, pp. 2252–2262, 2000.

[74] G. G. Borg, J. H. Harris, N. M. Martin, D. Thorncraft, R. Milliken, D. G. Miljak, B. Kwan, T. Ng, and J. Kircher, "Plasma as antennas: theory, experiment, and application," *Phys. Plasmas*, vol. 7, no. 5, pp. 2198–2202, 2000.

[75] M. H. Phillips, L. W. Anderson, and C. C. Lin, "Electron excitation cross sections for the metastable and resonant levels of Ne ($2p^5 3s$)," *Phy. Rev. A*, vol. 32, pp. 2117–2127, 1985.

[76] M. Johnston, K. Fujii, J. Nickel, and S. Trajmar, "Ionization of metastable neon by electron impact," *J. Phys. B*, vol. 29, pp. 531–543, 2009.

[77] J. B. Boffrard, M. L. Keeler, G. A. Peiech, L. W. Anderson, and C. C. Lin, "Measurement of electron-impact excitation cross sections out of the neon $^3p_2$ metastable level," *Phy. Rev. A*, vol. 64, pp. 03 270 801–03 270 810, 2001.